DEBONDING OF FRP FROM CONCRETE IN STRENGTHENING APPLICATIONS: EXPERIMENTAL INVESTIGATION AND THEORETICAL VALIDATION

by

MOHAMAD ALI-AHMAD

A dissertation submitted to the Graduate Faculty in Engineering in partial fulfillment of the requirements for the degree of Doctor of Philosophy, The City University of New York

2005

UMI Number: 3187469

ProQuest Information and Learning Company
300 North Zeeb Road
P.O. Box 1346
Ann Arbor, MI 48106-1346

This manuscript has been read and accepted for the
Graduate Faculty in Engineering in satisfaction of the
dissertation requirement for the degree of Doctor of Philosophy.

Prof. Kolluru Subramaniam

Date

Chair of Examining Committee

Dean Mumtaz Kassir

Date

Executive Officer

Prof. Michel Ghosn

Prof. Anil Agrawal

Prof. FengBao Lin

Prof. Thomas Price

Dr. Christian Carloni

Supervision Committee

THE CITY UNIVERSITY OF NEW YORK

Abstract

DEBONDING OF FRP FROM CONCRETE IN STRENGTHENING APPLICATIONS: EXPERIMENTAL INVESTIGATION AND THEORETICAL VALIDATION

by

MOHAMAD ALI-AHMAD

Adviser: Professor Kolluru Subramaniam

The last few years have witnessed a wider use of fiber reinforced polymer (FRP) sheets for strengthening existing reinforced and prestressed concrete structures. The success of this strengthening method relies on the effectiveness of the stress-transfer between the concrete and the FRP. Although previous studies have demonstrated the merits of using FRP composites, a number of issues are hampering the widespread implementation of this new technology. These issues are related to the shear debonding failure in the FRP-concrete interface. This study consists of the experimental investigation of the interfacial bond behavior between concrete and FRP. A material law for the FRP-concrete interface is established. The instability at failure of the FRP-concrete bond is found to be the result of snapback. The load response of the interfacial bond is shown to change from softening to snap-back upon increasing the bonded length of the FRP composite. The effect of harsh environmental conditions especially freeze-thaw cycles on the interfacial bond is also investigated. The results of the statistical analysis indicate that there is a significant drop in the interfacial fracture energy with freeze-thaw cycling. The results also suggest a progressive decrease in the fracture parameters with freeze-thaw cycling

indicating continuous accrual of freeze-thaw damage in the interface. The nonlinear material law of the FRP-concrete interface, which considers the shear-debonding mode of failure, is incorporated into a numerical model for predicting the load-deflection response of FRP-strengthened beams. The load response obtained numerically is compared with existing experimental results. It is shown that the high stress concentration in the FRP-concrete interface close to a flexural crack is responsible for the initiation of debonding. A failure criterion based on a critical value of strain gradient, which can be obtained from a direct shear test, is proposed.

This thesis is in memory of my sister, Sawsan.
Her smile is always in my mind. I will never forget her.

Acknowledgment

I would like to express my gratitude to my advisor, Professor Kolluru Subramaniam, for his support and encouragement throughout my doctoral study. This thesis would have been impossible to be completed without his editorial and academic advice. I would also like to thank him for editing of my publications and spending the time teaching me using the equipments in the laboratory.

I would also like to thank my co-advisor, Professor Michel Ghosn, for his guidance, support and expertise in editing my thesis. His encouragement and useful discussions were very helpful over the last five years. I also would like to thank Professor Anil Agrawal, Dr. Christian Carloni, Professor FengBao Lin, and Professor Thomas Price for their remarkable advices and for serving in my PhD committee.

I wish to express my thanks to my friends and colleagues at City College of New York for all the discussions, cooperation and for the wonderful time we have shared. I also would like to thank Yevgeniy Leykin and Jifang Zhu for their help in the laboratory.

I wish to thank my engineering team at Goldstein Associates for their support during the last period of my study.

I am very grateful for the continuous help and encouragement of my parents and my brothers.

Especially, I would like to express my loving gratitude to my wife, Nina, for her patience, understanding and support throughout this work, and to my son, Ramy, who is a never-ending source of love, pride and inspiration to me.

Table of Contents

List of Tables

List of Figures

CHAPTER 1

INTRODUCTION

1.1 Background

In a recent study sponsored by the National Academy of Sciences, the value of concrete-based structures in the United States was estimated to be six trillion dollars. Yet, many of these concrete structures, especially highway bridges that were built more than four decades ago, are classified as structurally deficient and in need of rehabilitation (Report to Congress, *1999 Status of the Nation's Highway Bridges and Transit: Conditions and Performance*). The urgent need to rehabilitate these structures is forcing the engineering community to develop repair strategies that are both reliable and economical. Because of their superior structural properties, the use of Carbon Fiber Reinforced Polymer (CFRP) composites has generated considerable interest for retrofitting these existing structures especially bridges. The benefits of using FRP composites for strengthening bridge members are: (a) reduced cost for rehabilitation of deteriorated members; (b) lightweight and flexibility that makes them transportable and

adaptable for use in different configurations and in difficult to reach places; (c) high tensile strength and excellent corrosion resistance; and (d) repairs can be made while the bridge is still in service avoiding traffic disruptions and associated economic and environmental impacts.

FRP sheets applied to existing bridge girders are used to improve their flexural and shear performances. In typical flexural and shear strengthening applications, test results (Ritchie et al. 1991, Buyukozturk & Hearing 1998, Lopez et al. 2000) have shown that besides the usual failure modes observed in reinforced concrete beams, premature debonding of the FRP from the concrete substrate is an important factor that controls the efficacy of the repair. Despite the observation made by previous studies that FRP debonding is one of the most critical failure mechanisms, no previous studies have yet succeeded in developing a rational and consistent mechanistic model that accounts for the factors that control debonding or to understand the behavior of the structure during the debonding process. The lack of such a model has hampered the wide scale implementation of FRP repair methods in rehabilitating existing deteriorated concrete structures despite the fact that in-situ testing has been on going for over two decades. To help overcome this problem, this study conducts an experimental investigation of the debonding failure at the interface between the concrete and the FRP. The effect of environmental impacts, such as freeze-thaw exposure, on the bond behavior is also studied. The experimental investigation leads to the development of a mechanistic model to predict the debonding of FRP from the concrete substrate of reinforced concrete beams. The debonding failure mode is then incorporated into an analytical model for predicting the load-deflection response of FRP strengthened concrete beams.

1.2 Research Objectives and Scope

The main objective of this study is to develop a fundamental understanding of the interfacial debonding observed in concrete beams externally strengthened with CFRP composite sheets. To account for the debonding failure mode and incorporate it into an analytical model for predicting the load-deflection response of strengthened beams, it is necessary to investigate the interfacial bond behavior between the concrete and the FRP. Therefore, establishing the material law for the bond and investigating the effect of environmental conditions on this law are the essential issues addressed in this study. The material law obtained experimentally is used in numerical simulations to explain the scaling in the direct shear response of FRP sheets bonded to concrete. Finally, this study includes numerical simulations to investigate the failure criterion for FRP-concrete interfacial debonding close to flexural cracks in concrete beams.

1.3 Outline of the Dissertation

This dissertation presents a comprehensive study of the debonding phenomenon which leads to achieve the above-stated research objectives. This study involves: (a) a review of the literature on the application of FRP for strengthening concrete members; (b) an experimental investigation of the bond between the FRP and concrete; (c) an experimental investigation of environmental effects particularly freeze-thaw cycles on the FRP-concrete interfacial bond; (d) a numerical analysis of instability in FRP-concrete shear debonding; and (e) failure analysis of FRP-strengthened concrete beams. The general description of the dissertation is summarized in the following chapters:

Chapter 2: *Literature review*. This chapter reviews the-state-of-the-art of FRP applications in strengthening concrete structures. The literature review is

divided into three main sections: (a) The structural properties of the components used in externally strengthening reinforced concrete beams with CFRP are described in the first section; (b) The second section reviews experimental, analytical and numerical investigations of FRP strengthened beams; and (c) The third section reviews experimental and analytical investigations that study the bond behavior and the load transfer between the FRP sheets and concrete.

Chapter 3: *Experimental investigation and fracture analysis of debonding between concrete and FRP*. Direct shear tests are performed to study the progressive debonding between the concrete and the FRP. The strains in the FRP and concrete surfaces are determined using an optical technique known as digital image correlation (DIC). The nonlinear cohesive material law for shear fracture is determined from the strain analysis. The fracture energy for the interface is obtained from the material law. The load-slip response of the bond between the concrete and FRP is interpreted in terms of the crack propagation. Instability in the load response of the interfacial bond at ultimate failure is shown to be the result of snapback.

Chapter 4: *Freeze-thaw degradation of FRP-concrete interface: impact on the fracture parameters*. An experimental program for subjecting specimens to freeze-thaw cycles, which realistically simulates the actual in-field conditions, is developed in this chapter. The experimental test results and the effect of freeze-thaw damage on the interfacial material law are presented and compared with the material law obtained from tests performed on dry

specimens. The results show that freeze-thaw cycling produces a statistically significant decrease in the ultimate load transferring capacity, interfacial fracture energy and the parameters of the interface material law.

Chapter 5: *Analysis of instability in FRP-concrete shear debonding for beam strengthening applications*. This chapter presents a numerical analysis of the FRP-concrete shear debonding mechanism using the nonlinear material model for the interface previously established in Chapter 3. The analysis is carried out using the finite element method. An insight into the unstable failure witnessed in shear debonding in beams is obtained from the numerical analysis of the direct shear test geometry. The equilibrium path of the load response after the point of instability in the debonding response of FRP is traced using the arc-length method and the reason for the instability is shown to be the snap-back mechanism. The fracture parameters of the material law are treated as random variables. A Monte Carlo simulation is performed taking into consideration the correlation between the fracture parameters to study the effect of randomness of these parameters on the direct shear load response of FRP sheets bonded to concrete. This chapter also presents a parametric study to investigate the influence of the geometric variables such as the number of FRP plies and the variation in the fracture parameters on the debonding mechanism and the load response of the FRP bonded to concrete.

Chapter 6: *Failure analysis of FRP-strengthened concrete beams*. In this chapter, analyses of the behavior of plain concrete beams strengthened using externally attached FRP composite sheets are presented. Firstly, a

preliminary analysis based on concept of linear elastic fracture mechanics is performed to study the debonding mechanism at the FRP-concrete interface. In the second part of this chapter, a three dimensional finite element analysis considering the nonlinear FRP-concrete material law and smeared cracking for concrete in tension is presented. The initiation of debonding, the progressive debonding and the ultimate failure of FRP-strengthened concrete beam are investigated. A comparison between the conventional strain-based sectional analysis and the nonlinear finite element analysis is also performed in this chapter. It is shown that the strain-based failure criterion (recommended by ACI 440) is not conservative for predicting the debonding mode of failure. Finally, a debonding failure criterion for shear and flexural strengthening applications is proposed based on the strain and the strain gradient along the FRP composite.

Chapter 7: *Conclusions and recommendations*. In this chapter, a summary of the results included in the dissertation and recommendations for the implementation of FRP repair strategies are presented. Future research interest is also presented at the end of this chapter.

CHAPTER 2

LITERATURE REVIEW

2.1 Introduction

Carbon Fiber Reinforced Polymer (CFRP) sheets have been used successfully for strengthening existing reinforced and prestressed concrete bridge structures. The benefits of using CFRP composites for strengthening bridge members are: (a) reduced cost for rehabilitation of deteriorated members; (b) lightweight and flexibility that makes them transportable and adaptable for use in different configurations and in difficult to reach places; (c) high tensile strength and excellent corrosion resistance; and (d) repairs can be made while the bridge is still in service avoiding traffic disruptions and associated economic and environmental impacts.

Typical applications of FRP strips in strengthening of bridge members include: (a) applying transverse strips to improve the shear capacity of concrete members; (b) attaching longitudinal strips to the tension face of girders to improve flexural capacity; and (c) wrapping of concrete columns with Fiber/Epoxy jackets for seismic retrofit to

increase column ductility and concrete strength by confinement. In typical flexural and shear strengthening applications, the stresses are transferred to the FRP through the bond between the two materials. Thus, the bond becomes an important factor that controls the level of strengthening achieved. In applications involving wrapping of columns, tensile stresses are produced in the FRP by concrete bearing pressure against the FRP where the bond has relatively little importance. The FRP provides confinement to the concrete, which increases the load carrying capacity and the ductility. For use of FRP in bond sensitive applications such as in flexural or shear strengthening of beams, the behavior of the bond between FRP and concrete must be well understood. This chapter presents a review of the-state-of-the-art of FRP applications in strengthening concrete structures. The chapter is divided into three parts: (a) strengthening components of FRP composites; (b) flexural behavior of strengthened concrete girders; and finally (c) behavior of the bond between concrete and FRP laminates.

2.2 Strengthening Components

Fiber reinforced polymer strengthening systems are commercially available as plates or sheets. FRP plates are fabricated to fit the shape of the beam or column and are attached to the structural members using epoxy. Sheets on the other hand are composed of fibers reinforced with an epoxy matrix and because of their flexibility can be adapted to fit any structural components and shape.

Unidirectional FRP composite sheets are increasingly used for strengthening deteriorated bridge girders. Fiber sheets are typically made of Carbon or Glass fibers. Carbon fibers are most popular because of their high strength, stiffness, and durability. In a typical strengthening application, FRP composite sheets are attached to the concrete

structural members using an epoxy-based adhesive. During application, the epoxy impregnates the fiber sheets. Upon setting, the epoxy forms a composite with the fibers and also provides a bond with the substrate. Most commercially available epoxies provide sufficient bond strength with concrete and often failure is observed in a thin layer of concrete underneath the epoxy layer (Swamy et al. 1986, Chajes et al. 1996, and Yoshizawa et al. 1996, Ali-Ahmad et al. 2005).

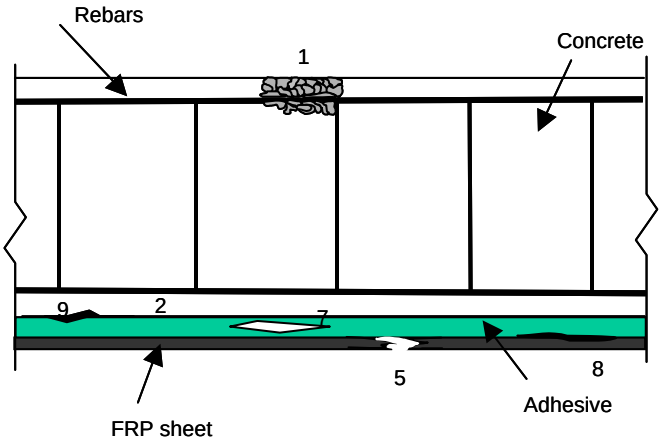

Figure 2.1: Possible failure modes in RC beam externally strengthened with FRP

2.3 Flexural Strengthening of Concrete Beams

In a typical flexural beam strengthening application, FRP composite strips are bonded to the tension side of the beam to act as supplementary reinforcement and contribute to the overall strength and stiffness of the beam. The load capacity of the strengthened beam depends upon several parameters summarized by Reddy et al. (1996) as follows: (a) the geometry of the beam and FRP laminate; (b) the bond at the interface between concrete and FRP composite; (c) the mechanical properties of concrete and FRP laminate; (d) the type of epoxy and primer used; (e) surface preparation procedures;

(f) type of steel reinforcement (under or over reinforcement, prestressed); (g) extent of beam cracking; (h) loading condition; and (i) environmental exposure.

Composite action between the concrete and the FRP is ensured by the interfacial bond strength between the two adherents. However, it is often difficult to develop the total composite strength capacity because of premature failure of the interface due to debonding, delamination and/or peeling-off of the laminate. Considering the different factors listed in the previous paragraph, the failure modes exhibited by beams strengthened with externally bonded FRP are (Meier et al. 1992):

1. Concrete compressive failure: Crushing of the concrete in compression before yielding of the reinforcing steel.
2. Failure of the concrete layer between the steel reinforcement and the composite plate. This failure mode is unique to plated beams and is caused by stress concentration at the end of the plate.
3. Diagonal tension failure resulting from vertical shear in the section.
4. Tension failure of reinforcing steel (like fatigue failure).
5. Tension failure (rupture) of the FRP sheet. The sheets fail suddenly with an explosive snap.
6. Inter laminar shear failure in FRP sheet (secondary failure).
7. Cohesive failure within the adhesive.
8. Adhesive failure at the FRP composite sheet/adhesive interface primarily observed when beams are subjected to freeze-thaw cycles.
9. Adhesive failure at the concrete/adhesive interface resulting in debonding of the FRP laminate, which is also called interfacial bond failure.

Broadly, these failures can be classified into three types: (a) failure in the beam, (1 2, 3, 4); (b) failure in the FRP composite, (5, 6); and (c) failure at the interfaces, (7, 8, 9). Detailed investigations of these failure modes were presented by Quantrill et al. (1996) and Saadatmanesh and Malek (1998) and are schematically shown in Figure 2.1.

2.3.1 Experimental Investigation of Strengthened Beams

The earliest known work on the application of FRP was carried out by Meier et al. (1987) who tested concrete beams with CFRP composite sheets externally bonded to the tension side of the beams. While a 100 % increase in the ultimate load carrying capacity was observed, there was a significant reduction in the ductility of the beam. The final deflection at failure was observed to be 50% lower than that of the unstrengthened beam. The loss of ductility in beams strengthened with externally bonded FRP has been identified as a significant factor to be considered in design by several researchers (Triantafillou and Pelvris 1991, Ritchie et al. 1991, Chajes et al. 1994).

From the experimental investigation of large reinforced concrete beams with varying steel reinforcement ratios and shear reinforcement, Saadatmanesh and Ehsani (1991) concluded that gluing GFRP plates increases the strength and stiffness of the beams. The GFRP plates carried a portion of the tensile force, which decreased the stress in the steel reinforcement. In addition, it was found that the extent of cracking and the ductility of the beams were reduced at all load levels.

Ritchie et al. (1991) investigated the influence of the type of FRP plate, plate dimensions and end-anchoring schemes on the mode of failure and the increase in strength and stiffness of concrete beams. To prevent plate end peeling, several end-anchoring schemes were used (as shown in Figure 2.2). These consisted of: (a) wrapping

the plate end with bonded angles to the top of the beam; and (b) extending the plate up to the support. Both methods were successful in increasing the load capacity. From their experimental study, the authors did not recommend any specific end-anchoring scheme for field applications nor did they provide enough information to clarify the mechanisms of each failure mode. The only recommendation they made was to extend the plate all the way up to the support in long span beams with smaller ratio of shear to moment.

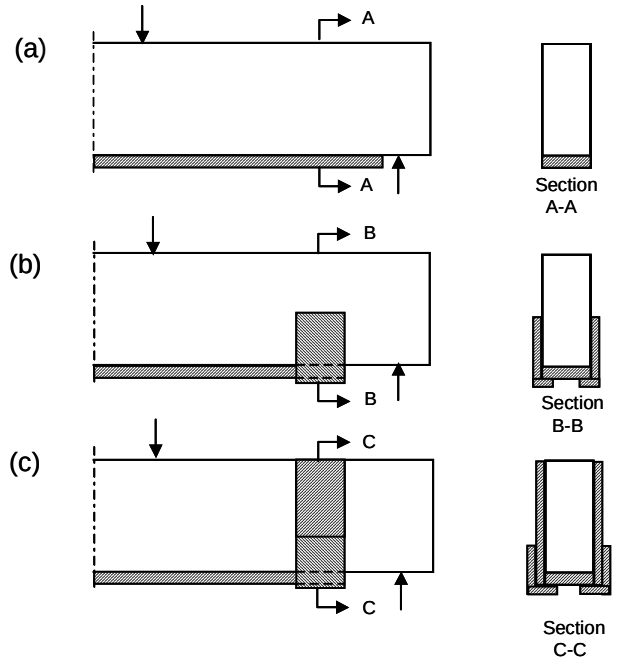

Figure 2.2: FRP end-anchorage schemes: (a) plate extended up to the support; (b) partial-height bonded angles; and (c) full-height bonded plates connected by bonded angles (Ritchie et al. 1991)

From the experimental investigation of initially loaded RC beams externally strengthened with FRP plates, Sharif et al. (1994) concluded that the repaired beams developed their ultimate flexural capacity if premature failures were prevented. Peeling of the plates from the ends, FRP plate rupture and diagonal tension crack failure were identified as primary modes of premature failure (as shown in Figure 2.3). It was shown that the failure mechanism depends on the plate thickness. As the plate thickness

increases, the failure changes from FRP plate rupture to plate end peeling. Use of anchor bolts at the ends of the plates and FRP jackets were found to prevent premature failure due to end peeling of the FRP plate.

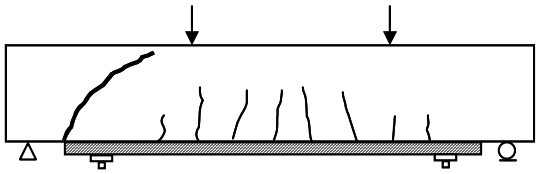

Figure 2.3: Diagonal tension-crack failure in FRP strengthened beams (Sharif et al. 1994)

Yoshizawa et al. (1996) studied the relationship between concrete surface preparation and the flexural strength of beams externally strengthened with CFRP sheets. A better bond between concrete and FRP was observed in the beams treated with water jet when compared with those obtained by sanding the concrete surface. No noticeable influence on the ultimate load capacity was observed by using different water jet pressures or by using different primers. It was observed that as the surface preparation changed from sanding to water jet treatment, the ultimate load capacity increased by up to 40% and the failure mode changed from interfacial bond failure (concrete/adhesive interfacial failure) to concrete cover failure (failure of concrete cover between steel reinforcement and FRP sheets). Unfortunately, the latter result has not been widely confirmed and there was no acceptance for the use of water jet surface treatment as a solution for preventing the debonding mode of failure.

Norris et al. (1997) presented the results of an experimental study of the behavior of damaged concrete beams retrofitted with thin CFRP sheets. The effect of CFRP sheets on strength and stiffness of the beams was investigated for various orientations of the fibers with respect to the axis of the beam. The strengthening consisted of U-shaped

sheets wrapped around the beam section (as shown in Figure 2.4). It was concluded that the direction of reinforcing fibers significantly influences the increase in strength and stiffness and the mode of failure. The largest increases in stiffness and strength were obtained when the CFRP fibers were placed perpendicular to the cracks in the beam.

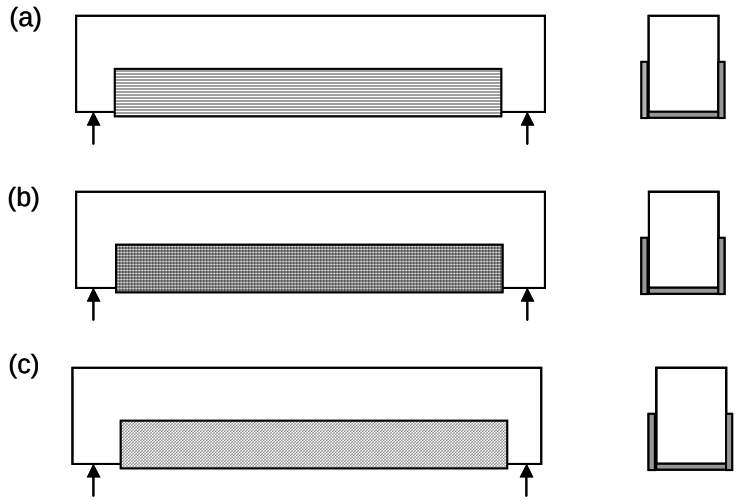

Figure 2.4: FRP fiber orientations: (a) longitudinal fibers; (b) fibers parallel and perpendicular to beam axis; and (c) fibers applied at 45^{o} angle (Norris et al. 1997)

The available information on the flexural behavior of reinforced concrete beams strengthened with CFRP plates and sheets can be summarized: (a) there is a reduction in ductility of the beam; (b) external strengthening contributes to decreasing the beam flexural and shear crack sizes and increasing its yield and ultimate load carrying capacity; (c) beam strengthened using FRP plates exhibit a peeling mode of failure where the FRP plates peel from the ends; (d) using end anchorage devices can prevent plate end peeling; and (e) end peeling failure mode is not common in sheets.

2.3.2 Analytical Models for Strengthened Beams

Sectional Analysis Procedures

Several analytical models have been proposed to investigate the load response of RC beams externally strengthened with FRP. Early models were based on simplified assumptions, such as those used in the design of reinforced concrete beam sections. Most early models were primarily based on sectional analysis, which assumes the following: (a) linear strain distribution throughout the depth of the beam; (b) small deformations; (c) tensile strength of concrete is negligible; (d) shear deformation is negligible; and (e) perfect bond between the concrete and FRP (i.e. no relative slip between the FRP and concrete). In such an analysis, it is implicitly assumed that the ultimate failure of the FRP can be achieved before the failure of the bond between the concrete and FRP. Using these simplified assumptions, El-Milhimy and Tedesco (2000) developed moment capacity design curves as a function of several geometric variables. Sectional analysis based procedure, which do not consider the debonding mode of failure, overestimate the moment capacity in beams, which fail by debonding.

Triantafillou and Pelvris (1991) developed a procedure for estimating the ultimate moment capacity of FRP-strengthened beam sections, which considers debonding. The ultimate load carried by the beam before debonding failure is produced by interfacial crack propagation was predicted. Using the established principles of Linear Elastic Fracture Mechanics (LEFM), the critical load for crack propagation along the interface was obtained as a function of G_{IIc} (the critical mode II energy release rate). While this model provides an insight into the failure at one section and estimates the

reduction in moment capacity due to debonding, it does not properly model the full response of strengthened beams since a beam is assumed to fail when one section fails.

Sectional analysis procedures have also been used to predict the load-deflection response of strengthened beams. In the sectional analysis, the moment-curvature response of one section is determined and then the load-deflection response of the beam is obtained by integrating the response of all the sections along the length of the beam. Arduini et al. (1997) developed an analysis procedure for the load-deflection response of RC beams strengthened with FRP plates during progressive peeling of the FRP plate from its ends. Using a sectional analysis, the stresses in concrete, steel and FRP were evaluated at different sections along the length of the beam. The stresses in the FRP were used to evaluate the stresses at the concrete-FRP interface. By using the strain as the criterion for the separation of the FRP plate from concrete, the load-deflection response of the beam was obtained for progressively large peeled lengths of the FRP plate. From the analysis, Arduini et al. (1997) established that the failure of the beam does not coincide with the failure of the section where peeling is initiated. This analysis is only valid for beams strengthened with FRP plates where interfacial crack forms and propagates in the concrete/adhesive interface from the end of the FRP plate towards the center of the beam. However, this method is not valid in the case of FRP sheets because the interfacial crack (in the concrete/adhesive interface) propagates from the center of the beam towards the supports. In this case, the fully debonded portion of FRP sheet remains connected at both ends and its contribution cannot be disregarded. More sophisticated analyses to predict such mode of failure have yet to be developed.

While the sectional analysis predicts the ultimate capacity of a section in situations where no debonding occurs before failure, models based on sectional analysis often are unreliable in predicting the ultimate load and the load-deflection response of the beam when debonding occurs. For instance, sectional models underpredict the ultimate deflection at failure. This discrepancy can be explained considering the assumptions made during sectional analysis.

Linear Elastic and Nonlinear Procedures

Linear elastic analyses were used by several researchers to gain an understanding of the stress distribution at the interface between FRP and concrete. Taljsten (1997) presented an analytical model to solve for the stresses acting at the edge of a plate externally bonded to a reinforced concrete beam in an attempt to explain the peeling of FRP plates from the end. This problem was modeled as a beam on elastic foundation to predict the shear and normal stresses in the adhesive layer connecting the concrete and plate. The adhesive was modeled as springs connecting the plate and the concrete. As a conclusion, the critical stress levels that initiate end plate peeling were obtained at the end of FRP plate externally bonded to a beam with an arbitrary cross section loaded with a point load.

To account for the stress concentration and the stresses in the adhesive layer, Malek et al. (1998) investigated an analytical method to calculate shear and normal stress concentrations at the end of FRP plate externally attached to a reinforced concrete beam. The effect of large flexural cracks along the beam has also been investigated. Good comparison between the interfacial shear stresses between FRP plates and epoxy predicted by the model and a finite element analysis were obtained.

Wu and Niu (2000) investigated the effects of flexural cracks in concrete on the interfacial shear stress in FRP-strengthened reinforced concrete beams for several load cases based on linear elastic beam theories. Closed form solutions for shear stress distribution along the FRP-concrete interface due to flexural cracks were derived for several load cases: (a) three-point bending; (b) four-point bending; and (c) uniformly distributed loading. The shear stress distribution obtained based on linear elastic beam theory was verified by comparisons with FEM analyses. Finally, the authors proposed a methodology for predicting the initiation of debonding in reinforced concrete beams and compared the debonding load with that obtained from existing experimental data.

Based on a Closed-Form High-Order approach (CFHO), Rabinovich and Frostig (2001) presented a non-linear analysis of the behavior of cracked reinforced concrete beams retrofitted with externally bonded fiber-reinforced plastic strips. The model considered the nonlinear constitutive relations of the various materials. The complete nonlinear response of the beam, including stresses and deformations, was calculated at every load level. Three types of retrofitted RC beams were analyzed: Rectangular RC beams strengthened with externally bonded glass-FRP strips; and two T-section beams retrofitted with CFRP strips. Verification of the CFHO nonlinear model was presented through comparison with experimental results. Some discrepancies blamed on the imperfect bonding of the FRP strip and local delaminations. Although the CFHO model provided a reasonable degree of accuracy in the case of perfect bond between the adherents, which is not unlikely in most strengthened beams, the complicated mathematical derivations involved makes it difficult to incorporate into routine design procedures.

Lopez et al. (2000) proposed a design procedure for structural elements externally reinforced with FRP laminates. The nonlinear stress-strain relations for steel and concrete and the linear elastic behavior of FRP laminates were utilized. The interfacial shear stresses were calculated based on the assumption that the FRP laminates and the adhesive layer (epoxy) are thin; therefore the stresses due to the bending moment acting on them can be disregarded. By defining the shear span as the inclined linear part of the bending moment diagram under four-point loading, an expression for the average uniform shear flow was derived from the equilibrium equation of the FRP plate. In the constant bending moment zone of the four-point loading a peeling failure model was derived. This model was based on the behavior of the individual concrete tooth formed between two adjacent flexural cracks deforming like a cantilever under the action of the shear stress between the plate and the extreme tension fiber of the concrete. The basic assumption was that failure occurs prior to debonding at the epoxy concrete interface. The minimum value of the shear stress that leads to this type of failure was developed as a function of: (a) the net depth of the concrete cover; (b) the width of the externally bonded FRP plate; (c) the width of the beam; (d) the tensile splitting strength of concrete; and (f) the average stabilized flexural crack spacing.

As a summary of this section, sectional analysis was used to predict the load-deflection response of FRP strengthened beams. However, this method is not valid in the presence of flexural cracks, which cause the initiation of interfacial cracks in the concrete/adhesive interface that propagate from the middle of the beam towards the supports. In this case, the unbonded portion of the FRP sheet remains connected at both ends and its contribution cannot be disregarded. Linear elastic theories were also applied

to predict the stress distribution along the interface between concrete and FRP. However, there are no known models for the analysis of RC beams accounting for the unbonded FRP under flexural crack.

2.3.3 Numerical Methods

Many researchers presented numerical models based on the finite element analysis for predicting the load response and studying the stress redistribution along the FRP sheets/plates. Malek et al. (1998) studied the interfacial shear stress between FRP and concrete and the normal stresses as well as the longitudinal stresses of FRP plates bonded to reinforced concrete beams using a finite element model. It was assumed that: (a) the FRP, concrete, steel, and epoxy are isotropic and linear elastic; and (b) there is full composite action between FRP and concrete. High shearing stresses in the interface were predicted by the numerical analysis at the cutoff point of the FRP plate. The high shear stress at the cutoff point provided a means for explaining the failure of bonded FRP sheets at the cutoff point.

Numerical simulation of a cracked RC beam considering a smeared crack approach to model the behavior of concrete in tension was used by Arduini et al. (1997) to study the load-deflection response of strengthened beams. Good correlation with experimental results was observed for the load-deflection response of the beam. However, the numerical model fell short in the identification of the maximum load carrying capacity of the beam. This could be attributed to the simplified assumption of perfect bond between FRP and concrete.

2.4 Interfacial Bond

The interfacial bond, which joins the concrete and FRP, is responsible for transferring the stresses from the concrete substrate to the FRP. Several researchers have conducted experimental and analytical investigations to study the bond behavior, load transfer between the FRP and concrete, and the debonding of the FRP from the concrete substrate.

2.4.1 Experimental Investigations of the Interfacial Bond

Several different test configurations have been proposed in the literature to study the interfacial bond behavior between FRP and concrete under shearing stresses. Most of the test setups can be classified as pull-push or pull-pull depending on the relative direction of the forces applied on the FRP and concrete as shown in Figure 2.5.

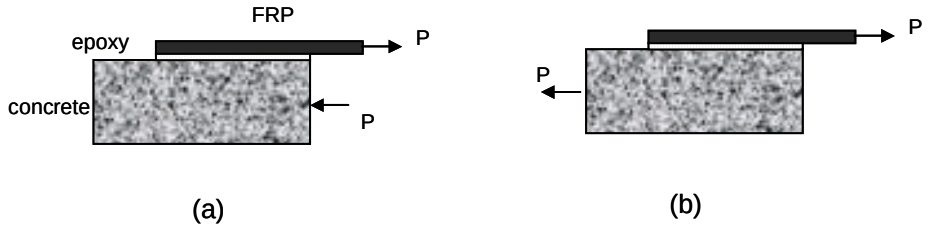

Figure 2.5: Test configuration of the interfacial bond between concrete and FRP: (a) pull-push joint; and (b) pull-pull joint

Following such investigations, Karbhari et al. (1997) determined the failure modes of FRP plates bonded to concrete depending on the layer where interfacial failure occurs. The authors classified these failure modes as follows: (a) interfacial failure between concrete and adhesive; (b) cohesive failure in the adhesive; (c) interfacial failure between the adhesive and the composite; (d) alternating crack path between the

two interfaces; and (e) peel failure into concrete. These failure modes are schematically shown in Figure 2.6.

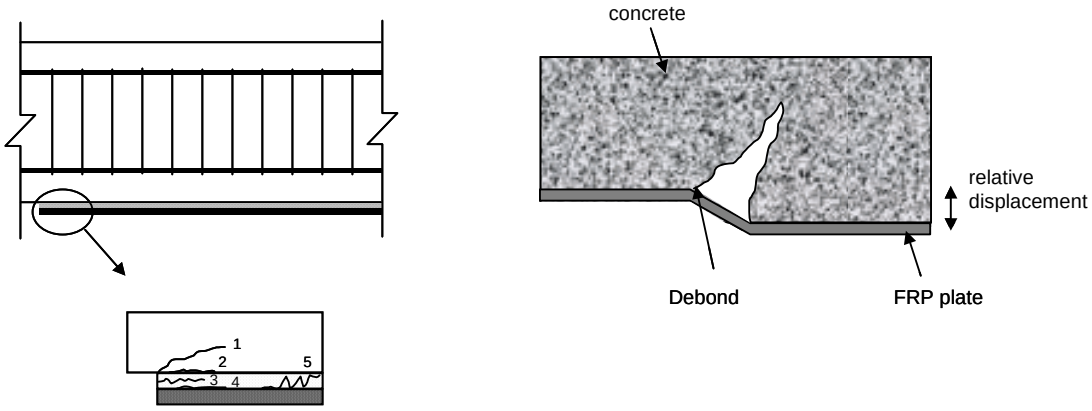

1: Peel failure into concrete
2: Interfacial failure between concrete and adhesive
3: Cohesive failure in the adhesive
4: Interfacial crack between the adhesive and the composite
5: Alternating crack path between the two interfaces

Figure 2.6: Schematic representation of interfacial failure modes (Karbhari et al. 1997)

Chajes et al. (1996) investigated the effect of surface preparation on the shear bond strength of FRP plates. Three different procedures were used: (a) no surface preparation; (b) grinding with a stone wheel to give a smooth finish; and (c) mechanically abrading with a wire wheel. In their tests, bond strength was defined as the ultimate load that the bond can sustain divided by the bonded area. The results of the surface preparation tests showed that the failure was initiated due to the shearing of the concrete directly beneath the adhesive layer. Based on these test results, mechanical abrasion of the concrete surface was found to produce the highest bond strength. In the case of the concrete failure directly beneath the adhesive layer, the researchers concluded that the ultimate bond strength is proportional to the square root of the compressive strength of concrete.

Swamy et al. (1986) investigated the influence of the thickness of epoxy on bond strength and found no variation in the strength of the bond between the adherents due to the adhesive layer thickness. Finally it was observed that there is a bond development length for a joint beyond which no further increase in capacity can be achieved.

Yoshizawa et al. (1996) studied the influence of concrete surface treatment, the rigidity of carbon fiber sheets (CFS), the number of CFS lamination layers and the localized debond (separation) of CFS on the overall bond strength. Bond strength was defined as the ultimate load divided by the total bonded area. It was observed that the failure occurred near the interface of concrete and CFS and when the bonding length was increased, the maximum tensile strength of the bond hardly changed from that of a 4 inch-bonding length. Surface treatment by water jet was found to be the most effective procedure for increasing the bond strength. Also, it was concluded that the bond strength increases as the number of CFS lamination layers increases. This is probably due to the reduction in the stress concentration near the edge.

Taljsten (1997) presented the result of pull out tests performed on concrete prisms onto which steel or CFRP plates have been bonded. The anchor length was defined as the minimum length of FRP/steel plate that contributes to the ultimate load capacity such that a longer bond would not add to the capacity. The criteria for the necessary anchor lengths for steel and FRP plates were presented as well as the critical strain level in the concrete at failure. The results showed that there is a specific anchor length for each material used. It was shown that the strain in the concrete was the governing factor in determining the interfacial bond failure. The observed failure occurs

directly in the thin concrete layer under the adhesive. The load response of the bond was determined and the debonding process was related to the strain distribution in the FRP.

Bizindavyi and Neale (1999) investigated the shear conditions between FRP sheets and concrete. Strain gauges were used to determine the strain distribution in the FRP at different load levels. From the strain data, the shear stress distribution along the bonded joint between concrete and FRP was determined. A uniform shear stress distribution along the bonded joint was assumed to determine the bond strength, which is the ultimate load divided by the bonded area. The values of the initial transfer lengths for GFRP/concrete and CFRP/concrete joints were estimated by defining the transfer length as the distance from the loaded end to the point on the joint where strain reaches zero.

Ueda et al. (1999) presented an experimental study on bond strength of Continuous Fiber Sheet (CFS). Several series of simple pull out test were conducted. Strain at CFS level was measured at many locations to observe bond strain distribution. Based on the experimental results, factors for determining the bond strength of CFS were presented. The effects of bond length, width of CFS, Stiffness of CFS (number of plies), loading condition and method of anchorage were studied. It was concluded that: (a) there is no increase in bond strength for bonds longer than 4 inches; (b) greater Stiffness of CFS provides greater bond strength and less strain gradient in CFS; (c) CFS with narrower widths have greater bond strengths than these with wider widths; (d) based on the observed local bond stress in CFS, an equation to predict the maximum bond stress was proposed.

Lorenzis et al. (2001) performed tests to identify the factors expected to affect the bond between FRP laminates and concrete. The test setup consisted of a plain concrete having inverted T-shape cross section. The beam was simply supported and externally reinforced with FRP sheets. In order to investigate the bond strength, a steel hinge was inserted at the top of the tested beam and a saw cut at the bottom. The load was applied at the hinge located at mid span. During loading, the saw cut caused a horizontal crack to propagate between the FRP sheets and concrete. From the test results, the strain distribution at the FRP level before the formation of the cracks was generated and the constitutive relationship of the bond was determined. It was concluded that the width of FRP sheets did not affect the bond strength, which contradicts the results of Ueda et al. 1999, and the bonded length did not affect the ultimate load, thus confirming the existence of an effective length beyond which no stress is transferred.

As a summary of this section, most investigations of the behavior of the interfacial bond between concrete and FRP plates or sheets focused on determining the type of failure and the ultimate load carrying capacity of the bond include shearing stresses, peeling stresses or combinations of the two types. The test results showed that peeling occurred in plates and is seldom observed in FRP sheets that primarily debond due to shearing stresses.

2.4.2 Analytical Models for the Interfacial Bond

The theoretical formulation of the shear response and the bond behavior between the FRP laminates and concrete has been the subject of intense research for the last decade. Existing formulations are based on either the theory of elasticity or fracture mechanics.

Elasticity Based Approach

The theory of elasticity may be used to derive the elastic shear and peeling stresses at the interface between concrete and FRP laminates. The following assumptions are typically made in a linear elastic analysis: (a) the materials are homogenous, isotropic and linear elastic; (b) the adhesive is only subjected to shear forces; (c) the thickness of the adherents and the adhesive are constant throughout the bond line; and (e) the width of the FRP plate/sheet is constant throughout the bond line.

Taljsten (1997), Bizindavyi and Neale (1999) derived expressions for the elastic shear along the bond at the FRP plate/concrete interface. The comparison showed that the analytically derived elastic shear stress accurately predicted the shear stress at early stages of loading and started to deviate at higher load levels.

Lorenzis et al. (2001) used a different geometry to illustrate the linear behavior of the joint between an FRP sheet and concrete. A linear bond stress-slip relationship, along with a simple shear model for the evaluation of the slip modulus, which is the shear stress divided by the relative slip, was used to model the strain distribution. A reasonable agreement with experimental results was achieved for low load levels.

Fracture Mechanics Based Approach

The FRP sheets have been observed to delaminate from the concrete substrate when a crack forms and propagates along the interface between the two materials. To explain the propagation of the crack, many researchers have used fracture mechanics to develop material models that can be used to predict the load response and failure of the bond. Usually, strengthening is performed on cracked reinforced concrete beams. In a cracked beam the stresses are transferred to the FRP in the portion of the concrete

between the cracks. In the case where the FRP is attached in the region where there are flexural cracks i.e. close to the maximum bending moment, a mode II mechanism (pure shear mode as described in Figure 2.7) is most probable to occur and the problem of debonding can be analyzed as the propagation of an interfacial crack. In this case, the shear stress is the dominant factor and peeling stresses are not significant. In the presence of a shearing crack, a crack that forms close to the support, the failure mechanism will be due to mixed modes I-II (mixed shear and opening mode), and the combination of interfacial and peeling stresses will drive the failure mechanism.

Taljsten (1996) developed an analytical expression for predicting the ultimate load of a joint between FRP plates and concrete using an energy-based criterion obtained from Linear Elastic Fracture Mechanics (LEFM). In his model the load at failure P_{max} is calculated as:

$$P_{\max} = \sqrt{\frac{2bG_f}{\frac{\partial C}{\partial a}}} \tag{2.1}$$

where G_f is the energy release rate; C is the compliance of the structure, which is the inverse of the stiffness; b is the width of the plate; a is the interfacial crack length; and P is the load applied to the joint between the two adherents. Expressions were derived for predicting the ultimate load in the two different test configurations (depicted in Figure 2.8): (a) symmetric; and (b) anti-symmetric load cases as a function of the plate width, elastic modulus of the adherents, thickness of the plate, and fracture energy (G_f).

For a symmetric joint, the load at failure is found to be:

$$P_{\max} = 2b\sqrt{EtG_f} \tag{2.2}$$

For an anti-symmetric joint:

$$P_{\max} = b\sqrt{\frac{2E_1 t_1 G_f}{1+\alpha}} \tag{2.3}$$

where $\alpha = \frac{E_1 t_1}{E_2 t_2}$, and E_i and t_i are the elastic modulus and thicknesses of the concrete and FRP with i=1 corresponding to the concrete and i=2 corresponding to the FRP.

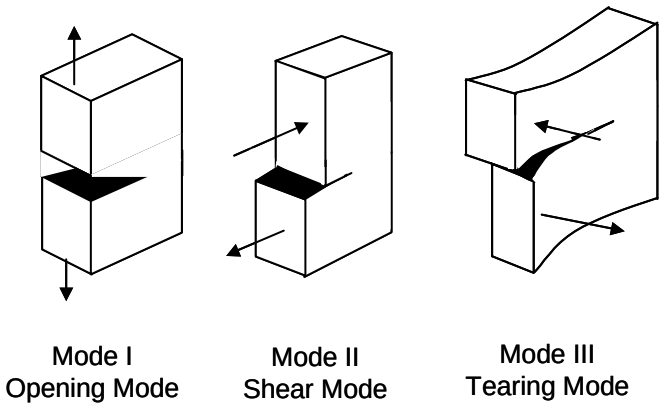

Figure 2.7: Schematic drawing of the three mode of failure.

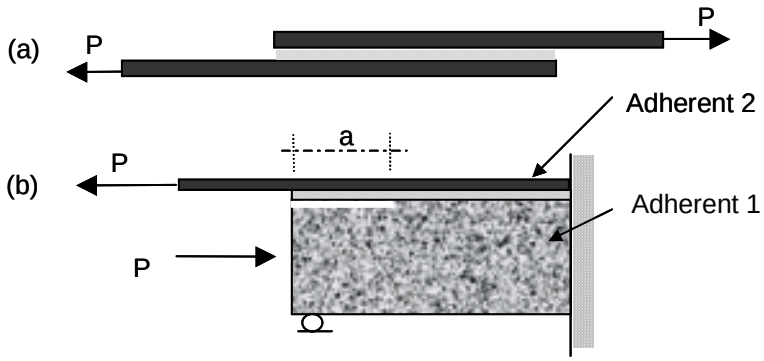

Figure 2.8: Schematic sketch of test setups: (a) symmetric; and (b) anti-symmetric joint (Taljsten 1996)

The derived LEFM equations gave a rough estimate of the maximum tensile load at failure. Also, one-dimensional nonlinear fracture mechanics approach based on assumed shear-slip curves was studied**.** The complicated mathematical derivations

involved in the nonlinear approach makes it difficult to find simple formulations for the load at failure.

Using the shear-slip curve obtained from experimental studies, Lorenzis et al. (2001) presented expressions for the critical load and the effective bond length based on LEFM model. A design equation was proposed to calculate the effective maximum FRP strain to be used in design to account for bond failure.

Yuan et al. (2001) assumed a variety of nonlinear constitutive laws describing the pre- and post-cracking behavior of FRP-concrete interface to solve the nonlinear interfacial stress transfer problem. Expressions for the bond strengths and the interfacial shear stress distributions along laminate-concrete interfaces were derived. The following conclusions were made: (a) for different stress-slip models, the load-carrying capacity was only dependent on the interfacial fracture energy, thickness of the FRP plate and young's modulus of the laminates; (b) the load carrying capacity and the effective bond length increased with the increase of interfacial fracture energy, thickness and young's modulus of the laminates; (c) shear stress-slip curves significantly affect the debonding propagation, shear stress distribution along the interface, and elastic-softening-debonding region and effective bond length.

2.4.3 Material Models for FRP- Concrete Interface

In the studies mentioned earlier (Taljsten 1997, Lorenzis et al. 2001), the constitutive law, the relationship between the shear stress and relative slip or τ-s curve, of the bond was assumed to be bilinear and the fracture energy (G_f) was considered to be the only parameter that controls debonding. Leung and Tung (2001) presented a three-parameter debonding model based on experimental and numerical investigations. The

authors proposed an interfacial cohesive material law that exhibits a sharp drop in interfacial shear resistance where the interfacial slip reaches a critical value followed by a more gradual decrease with further sliding. In this model, the sharp drop represents bond failure in the material, while the gradual decrease is due to a reduction of particle interlocking as sliding occurred. The debonding failure which is governed by the following three parameters (Figure 2.9): (a) the maximum shear stress that initiates debonding (τ_{max}); (b) the maximum residual stress right after debonding initiates (τ_0); and (c) a parameter governing the linear reduction of shear stress with sliding (k). Based on this new model, the expression of the tensile stress along FRP laminates was derived. It was found that the model was able to predict the trend of strain variations obtained in laboratory tests. By using this model a simulation was carried out which concluded that: (a) the post-peak residual shear stress at the interface could strongly affect the debonding behavior and cannot be neglected; and (b) the debonding behavior is not only affected by the fracture energy (G_f) but also depends on the shear stress versus sliding relationship.

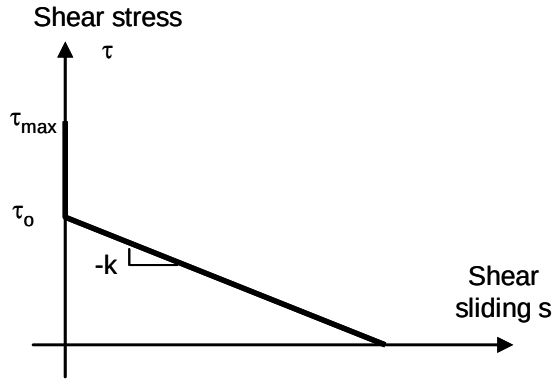

Figure 2.9: Shear stress versus slip for the debonding model (Leung and Tung 2001)

Lorenzis et al. (2001) established a material law from an experimental study. They observed that the shear versus relative slip curve does not include a softening part, which means that the shear resistance of the bond is not affected by an increase in slip. This result contradicted the observations of Leung and Tung (2001), which lead to a much higher value of the fracture energy release rate.

2.4.4 Impact of Environmental Factors on the Bond

The application of FRP sheets for strengthening reinforced concrete beams constantly exposes them to adverse environmental conditions. For example, the FRP sheets and epoxy adhesive are exposed to temperature variations, freezing and thawing cycles, wetting and drying cycles, salt runoff from deicing salt, UV radiation from the sun, and acid rain. The environmental factors progressively degrade the FRP sheets and the epoxy bond between the concrete and FRP. This results in a steady decrease in the load carrying capacity and the service performance of the strengthened/retrofitted structural element. It is believed that freeze-thaw cycles are among the most harmful environmental factors that reduce the integrity of the interfaces of the bonded joints.

Mukhopadhyaya et al. (1998) presented the results of a study on the influence of aggressive exposure conditions on the behavior of epoxy bonded concrete-glass fiber reinforced polymer plates. The accelerated tests consisted of exposing the specimens to freeze-thaw cycles in air with a temperature range of 20^{o}C and -17^{o}C, and a combination of chloride immersion and freeze-thaw cycles. It was concluded that the exposure regimes increased the bond transfer length, the magnitude of the shear stress distribution and the plate slip, and the combined chloride immersion/freeze-thaw cycles produced the largest differential movements between the plate and concrete substrate.

Green et al. (2000) presented experimental studies to examine the effects of freeze-thaw cycling on the bond between FRP and concrete. The specimens were exposed to up to 300 freeze-thaw cycles consisting of 16 hours of freezing and 8 hours of thawing in a water bath. It was observed that freeze-thaw cycling did not reduce the load carrying capacity of the joint between concrete and CFRP plates when the joints were loaded either in pure shear or in a combination of shear and flexure. On the other hand, as the number of freeze-thaw cycles was increased failure appeared to move into the epoxy-binding agent, such that failure generally occurred at the FRP-epoxy interface. Bisby and Green (2002) investigated the effect of freeze-thaw cycles on the bond between concrete and FRP of RC beams. It was observed that little, if any, damage to the FRP-concrete bond resulted from freeze-thaw cycles. At the University of Michigan, Lopez et al. (2000) studied the effect of freeze-thaw cycles on the overall beam behavior and bond strength. They concluded that a significant decrease in moment capacity occurs with an increase in the number of the freeze-thaw cycles contradicting the observation of Green et al. (2000).

Grace and Sing (2005) exposed RC beams strengthened using FRP to one freeze-thaw cycle every 4 hours. The temperature was varied between -17.8^{o}C and 0^{o}C. The authors observed that freeze-thaw cycling decreases the load-carrying capacity of reinforced concrete beams strengthened using CFRP plates and fabrics by up to 13%.

In summary, the literature review reveals that the impact of freeze-thaw on the bond between FRP and concrete is not completely understood and the results in the literature are often contradictory. The only significant result pertains to an observed change in the modes of failure and an increase in the relative slip between concrete and

the FRP at failure after a number of freeze-thaw cycles. The failure in RC beams, externally strengthened with FRP and exposed to freeze-thaw cycles, was found to consistently occur at the FRP/epoxy interface where the failure of regular beams occurs in the concrete/epoxy interface.

2.5 Summary

The review of the literature on previous research on RC beams externally strengthened with FRP has revealed the following:

1) The debonding mode of failure is the most critical of the possible failure mechanisms of externally reinforced RC beams.

2) The properties of each of the adherents is well understood individually can be well modeled.

3) The behavior of RC beams externally strengthened with FRP can be reasonably well modeled when perfect bonding of the adherents is in effect.

4) Most experimental studies of externally RC beams were performed on FRP plates which exhibit different debonding mechanisms than FRP sheets due to differences in the stress distribution near the edges of such materials.

5) Experimental investigations of the behavior of the bond at the interface of the different materials show varying results on the effect of different geometric properties such as thickness, and width of the FRP.

6) When using FRP sheets (rather than plates), experimental investigations show a sharp increase in the stress distribution near the edge of the sheet. The stresses rapidly decrease over a distance of about 4 inches.

7) The above observation, along with interfacial shear tests, indicates that the debonding can best be modeled using the theory of fracture mechanics.

8) Very few experimental investigations succeeded in obtaining realistic models of the material law for the FRP-concrete bond.

9) Due to the inconsistency and the dearth of available data, previous research has mostly used linear elastic models to describe the fracture of the FRP/concrete bond.

10) Hypothetical assumptions on different cohesive laws for the fracture of the FRP-concrete bond demonstrated the importance of using an accurate cohesive law accounting for the softening of the shear stress versus relative slip of the bond.

11) Experimental investigations of the impact of environmental loading such as freeze-thaw cycles produced conflicting results on their effect on the integrity of the FRP/concrete bond although a clear shift in the layer where debonding occurred was observed from the concrete side of the interface to the FRP side.

CHAPTER 3

EXPERIMENTAL INVESTIGATION AND FRACTURE ANALYSIS OF DEBONDING BETWEEN CONCRETE AND FRP

3.1 Overview

The last few years have witnessed a wide use of externally bonded carbon fiber reinforced polymer (CFRP) sheets for strengthening existing reinforced and prestressed concrete structures. The success of this strengthening method relies on the effectiveness of the load-transfer between the concrete and the FRP. Understanding the stress transfer and the failure of the concrete-FRP interface is essential for assessing the structural performance of strengthened beams and for evaluating the strength gain. This chapter describes an experimental investigation of the interfacial bond behavior between concrete and FRP. The strain distributions in concrete and FRP are determined using an optical technique known as digital image correlation (DIC). The results confirm that the debonding process can be described in terms of crack propagation through the interface between concrete and FRP. The data obtained from the analysis of digital images was used to determine the interfacial material behavior for the concrete-FRP interface (stress

versus relative displacement response) and the fracture energy (G_F). The instability in the test response at failure is shown to be the result of snapback, which corresponds with the elastic unloading of the FRP as the load carrying ability of the interface decreases with increasing slip.

3.2 Introduction

In typical flexural strengthening applications, FRP composite sheets are bonded to the tension side of the beam to act as external reinforcement. The FRP composite sheets contribute tensile forces to the internal moment resistance, which results in an increased load carrying capacity of the beam. The stress transfer from concrete to the FRP composite through the bond generates tensile stresses in the FRP. Thus, the bond between the concrete and the FRP composite becomes an important factor that controls the efficacy of the repair. In design applications, the load carrying capacity of a strengthened beam is evaluated considering the rupture mode of failure for the FRP composite, in addition to the usual modes of failure observed in a typical reinforced concrete beam (Meier et al. 1991, Quantrill et al. 1996, Saadatmanesh and Malek 1998, El-Mihilmy and Tedesco 2000). However, it has been shown that the total strength capacity of the beam is often not attained due to premature debonding of the FRP from the concrete substrate (Triantafillou and Pelvris 1992, Lopez et al. 2000). To develop rational models for predicting the load response of strengthened beams, the debonding behavior of the FRP composite from concrete must be understood. Material models, which consider the debonding mode of failure, can then be developed and incorporated into the analytical/numerical analyses for predicting the load-deflection response of strengthened beams.

Many researchers have developed fracture mechanics-based models to predict the theoretical load response for debonding failure mode of the FRP attached to concrete (Taljsten 1996, Yuan et al. 2001, Wu and Niu 2000). Due to lack of data, these models are based on an assumed constitutive law for the interface. The interfacial constitutive response is the relationship between the interfacial shear stress and the relative motion (slip) between the concrete and the FRP. Taljsten (1996) developed an approach for predicting the maximum force that the composite layers can resist before debonding by considering energy balance obtained from fracture mechanics. Yuan et al. (2001) studied the influence of the shape of the interfacial constitutive relationships on the load capacity of FRP bonded to concrete. Wu and Niu (2000) proposed a methodology for predicting the initiation of debonding in reinforced concrete beams using an assumed material model and compared the predicted debonding load with that obtained from existing experimental data.

A few detailed experimental investigations aimed at determining the strains in the FRP and the concrete during debonding have been conducted (Taljsten 1997, De Lorenzis et al. 2001, Ueda et al. 1999, Bizindavyi and Neale 1999). In these investigations, strains were measured using surface mounted strain gauges. Some researchers have attempted to establish the interfacial constitutive law using these data (De Lorenzis et al. 2001, Savoia et al. 2003). The strain obtained from strain gauges, however, does not provide sufficient spatial resolution to allow for an accurate determination of the interfacial stresses. A method for estimating the interfacial material law based on numerical inversion of experimental data was developed by Leung and Tung (2001). Direct experimental determination of the interfacial material behavior that

is derived from a spatially continuous measurement of strain has, however not been reported. A full understanding of the stress transfer between FRP and concrete during interfacial debonding and of the observed instability at failure in a direct shear response are also not available.

In this chapter, the progressive debonding between concrete and FRP is studied using an optical technique known as digital image correlation (DIC). DIC provides spatially continuous displacement fields during debonding. DIC has previously been used successfully to investigate the fracture mechanisms in concrete and composites (Choi and Shah 1997, Lawler et al. 1999, Sutton et al. 1993). From the information provided by DIC, the stress transfer during debonding along the FRP-concrete interface is studied. The nonlinear interfacial material behavior for fracture along the FRP-concrete interface is also determined. The instability in the test response at failure is shown to be the result of snapback.

3.3 Objectives

The objectives of this chapter are: (a) to study the progressive debonding process at the interface between the concrete and the FRP; (b) to determine the stress transfer between the adherents at different stages of debonding; (c) to develop a fundamental understanding of the load-slip response of the FRP in terms of the crack growth which produces debonding; (d) to establish the material law for the interfacial bond between the concrete and the FRP; and (e) to understand the nature of instability in the load response at failure.

3.4 Materials and test methods

3.4.1 Specimen details and material characteristics

Twenty five concrete blocks of nominal dimensions, length (330 mm), width (125 mm), and height (125 mm) were used in the experimental program. The concrete mix proportion by weight were: 2(coarse aggregates): 2(fine aggregates): 1(cement): 0.45(water). The coarse aggregates consisted of gravel with a maximum size equal to 10 mm. River sand was used as fine aggregate. The concrete specimens were deP{oLP .omolded 24 hours after casting and subjected to curing at 99% RH for 28 days. The 28-day compressive strength of concrete, determined as per ASTM-C39 (2000), was 38 MPa. The specimens were then placed in the laboratory environment (ambient temperature equal to 22^{o}C and RH equal to 50%) until tested.

Table 3.1: Properties of primer, resin and carbon fiber sheet

Products		Primer	Resin	Carbon Fiber Sheet
Product Number		PS301	L700W	REPLARK^{TM} 30
Good for		Cool season	Cool season	--
Usable Temperature (^{o}F) (Recommended)		41-77 ^{o}F (5-25 ^{o}C)	41-59 ^{o}F (5-15 ^{o}C)	--
Base Resin		Epoxy Based		--
Specific Gravity 77 ^{o}F	Main Agent	1.11	1.13	--
	Hardener	1.02	1.05	--
Tensile Strength (73 ^{o}F)		N.A	over 29 MPa	--
Flexural Strength (73 ^{o}F)		N.A	over 38 MPa	--
Tensile Shear Strength (73 ^{o}F)		N.A	over 9.7 MPa	
Thickness, t(mm)		--	--	0.167
Tensile Modulus, E(GPa)		--	--	230
Ultimate Tensile Strength, f_{fu}(MPa)		--	--	3820
Viscosity, mPa.S (73 ^{o}F)		500	3500	--
Pot Life, minutes (73 ^{o}F)		40	20	--
Curing Time, days (73 ^{o}F)		N.A	7	--

The FRP composite was applied to the surface of the concrete specimens using the wet-lay-up procedure recommended by the manufacturer (Technical Manual 2000). The FRP composites were fabricated in the laboratory and consisted of continuous unidirectional high-strength carbon fiber sheets (REPLARK^{TM} 30) with thickness equal to 0.167 mm in an epoxy-based resin (L700S^{TM}) supplied by Mitsubishi Chemical Corporation. The nominal material properties of the carbon fiber sheets, the primer and the resin, provided by the manufacturer, are shown in Table 3.1. During the application, the resin impregnates into the carbon fibers and also functions as the adhesive to bond the carbon fiber sheet to the concrete surface. Upon curing, the resulting composite strengthens the concrete surface. The application of the FRP composite to the concrete surface consisted of the following steps: (a) grinding the concrete surface using a disk grinder to remove any stain and grit; (b) removing the dust from the surface using pressurized air; (c) applying the primer followed by the resin undercoat; and (d) installing the carbon fiber sheet followed by a resin overcoat.

The FRP composite was attached in the center on one side of the concrete specimen when the concrete specimens were 90 days of age. A notch was introduced along the interface between the FRP composite and the concrete by leaving a portion of the FRP composite close to the edge of the concrete block unbonded (Figure 3.1a). The notch extended for a length approximately equal to 35 mm from the edge of the concrete block along the full width of the FRP composite. The width and the bonded length of the FRP composite attached to concrete were equal to 46 mm and 150 mm, respectively. After installing the FRP composite, the strengthened concrete block was allowed to cure for seven days in the laboratory environment before testing. Details of the specimen

geometry are shown in Figure 3.1a. In addition, FRP composite laminates of nominal dimensions, width (46mm), and length (300mm) were also fabricated for obtaining the material properties of the composite.

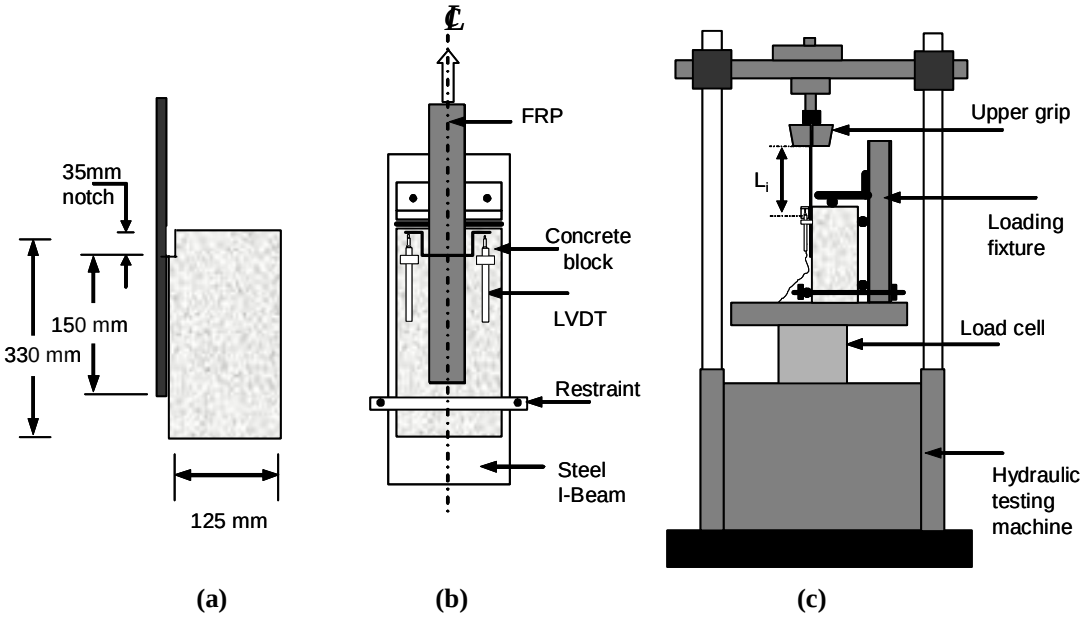

Figure 3.1: Specimen geometry and loading arrangement: (a) Specimen dimensions; (b) Loading fixture; (c) Test setup

3.4.2 Testing procedures and measurements

Uniaxial material properties of the FRP composite laminate were determined using a direct tension test. The uniaxial test of the FRP composite laminate was performed in displacement control up to failure. The strain in the FRP composite laminate was determined during the loading procedure using an LVDT gauge attached to the surface over a gauge length equal to 25 mm.

The debonding between the FRP composite and the concrete substrate was studied using a direct shear test. A loading fixture was designed for this purpose and consisted of a rigid steel I-beam which was anchored to the test machine (Figure 3.1c).

The concrete block was placed in the fixture and load was applied to the FRP composite while the reaction provided by the steel I-beam restrained the concrete block from movement (Figure 3.1b). Two linear variable displacement transformer (LVDT) gauges, which had a range equal to $\pm 2.5\text{mm}$, were attached to the concrete block on both sides of the FRP composite at the tip of the notch (Figure 3.1b). The LVDTs were reacted off of a thin plate, which was attached to the FRP composite also located at the tip of the notch. The displacement measured by the two LVDTs was averaged and is referred to as global slip (d) throughout this chapter. The tests were performed using a 223-KN capacity servo-hydraulic testing machine (Figure 3.1c).

Two types of direct shear tests were performed on strengthened concrete blocks: (a) quasi-static monotonic; and (b) quasi-static cyclic. In the quasi-static monotonic tests, the global slip was monotonically increased up to failure. In the quasi-static cyclic tests, the load was cycled from and to the load envelope at quasi-static rates of loading up to failure. All quasi-static monotonic and cyclic tests were performed in global slip control, at a constant rate equal to 0.00065 mm/sec.

For each test, the surface strains in the FRP composite and the concrete were obtained using the digital image correlation (DIC) technique. DIC is a data analysis procedure that uses the mathematical correlation method to analyze digital images of a specimen undergoing deformation. This technique offers the advantage of obtaining spatially continuous measurements of displacements. The surface preparation for the specimen consisted of creating a random, sprayed-on speckle pattern, obtained by spraying the FRP and the concrete surfaces with white paint followed by a black mist of paint. The test setup for DIC measurements comprised a high-resolution digital camera

(1280×1024 pixels), which was interfaced with a computer (Figure 3.2) using an image acquisition board. The specimen was illuminated using normal white light to provide uniform light intensity across the surface. The camera was placed perpendicular to the specimen surface at a distance equal to 1.5 meters. A reference image was recorded prior to the start of the loading procedure. The field of view captured in the digital image was 250mm×200mm. Digital images were recorded, at regular intervals during each test and stored in the computer for later analysis.

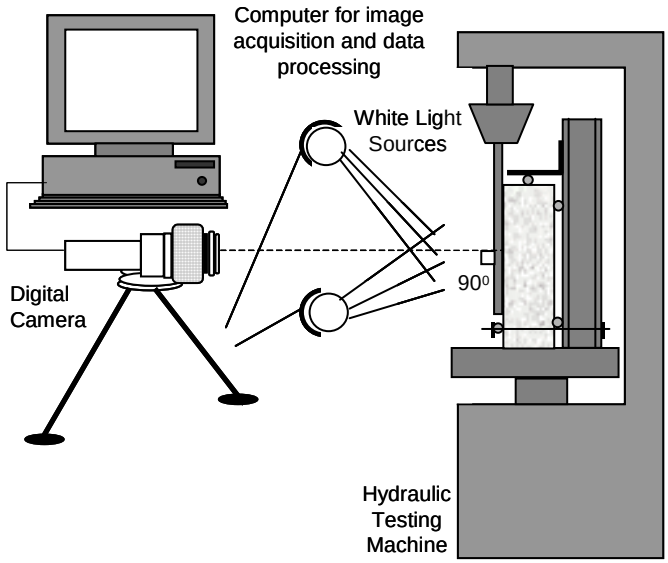

Figure 3.2: Digital Image Correlation test setup

The correlation between the deformed images and the undeformed reference image was used to obtain a two-dimensional displacement field for all points on the specimen surface. The displacement fields were computed through a correlation of gray levels between the reference image and the images of the specimen undergoing deformation using a commercially available software, Vic 2D. The image displacement accuracy was determined to be equal to 0.005 pixels and the accuracy in the measured

displacement field was equal to 1×10^{-6}m (Sutton et al. 1983, 1988, 1989). The strain fields were calculated from the gradients of a set of displacements. The accuracy of the measured strain was determined to be 50με (Sutton et al. 1983, 1988, 1989).

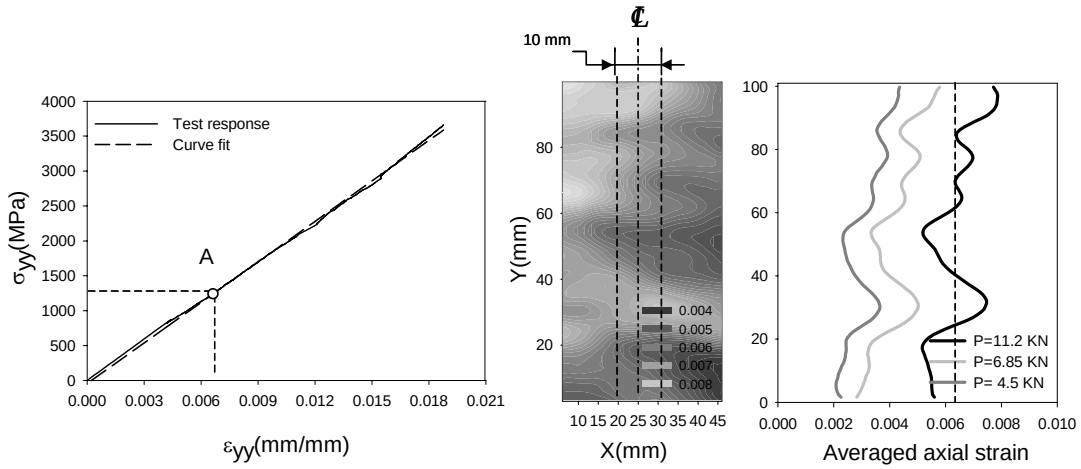

(a) **(b)** **(c)**

Figure 3.3: Uniaxial tensile tests of FRP composite strips; (a) Typical stress-strain relationship for FRP composite laminate; (b) Strain contours corresponding to point A of the load response; (c) Averaged strain distribution from 10mm wide strip versus location along the length of the FRP composite

3.5 Experimental results

3.5.1 Tensile tests of FRP composite strips

Four uniaxial tension tests were performed to obtain the material properties of the FRP composite laminate. A typical stress-strain response of the composite laminate is shown in Figure 3.3a. The engineering properties of the composite are based on the thickness of the fibers contained in the composite sheet and not the gross composite area, consistent with typical practice (Technical Manual 2000). The cross-sectional area of the composite laminate was determined based on the width and the thickness of the carbon fiber sheet in the laminate. The tests confirmed that the FRP composite exhibits linear elastic behavior up to failure. The nominal values of the Young's modulus and the

ultimate strain at failure were calculated as the average obtained from four specimens and are equal to 200 GPa and 1.8%, respectively.

Digital images of the FRP composite laminate were recorded at load intervals equal to 1KN during the uniaxial test. The images were captured for the portion of the FRP laminate sufficiently removed from the grips to avoid the local stress concentration in this region. The displacement fields obtained from the recorded digital images were used to generate the displacement contours and subsequently for determining the strain fields on the surface of the FRP composite laminate. The axial strain distribution (strain in the load direction) in the FRP composite at a load corresponding to 11.2 KN is shown in Figure 3.3b. The strain contours have varying gray scale intensities; darker contours indicate higher strains. It can be seen that there is a significant spatial variation in the axial strain recorded in the FRP composite, where it is expected to be constant. The fluctuations in the measured surface strain were found to be due to local material variations in the FRP laminate. Optical measurements performed using a 50X hand held microscope revealed that the observed variations correlated well with locations of material inhomogeneities found in the FRP composite laminate. A local low in the strain distribution was observed at points where fibers in the FRP composite laminate were bundled together. Also, variations in the thickness of the FRP composite laminate were found to contribute to local variations in the measured strain.

Since the axial response of the FRP composite and its variation in the axial direction are of interest in this study, it was decided to use an averaging procedure in the transverse (width) direction. The axial strain distribution along the length of the FRP composite laminate was obtained by averaging the strain across the width of a strip in

the center of the laminate as shown by the dashed vertical lines in Figure 3.3b. Averaging the axial strain across different strip widths (1, 2, 10 and 25 mm) revealed insignificant difference in the axial strain distribution along the length of the FRP composite. The axial strain along the length of the FRP composite for different load levels obtained using the averaging procedure across a 10mm wide strip is shown in Figure 3.3c. It can be seen that while there is a significant variation in the measured strain in the axial direction, the relative pattern of the strain distribution produced by the local material variations however does not change with loading (Figure 3.3c). The value of the mean axial strain at any given load obtained from the strain distributions shown in Figure 3.3c was found to compare very well with the strain at the corresponding load level measured using the LVDT (Figure 3.3a).

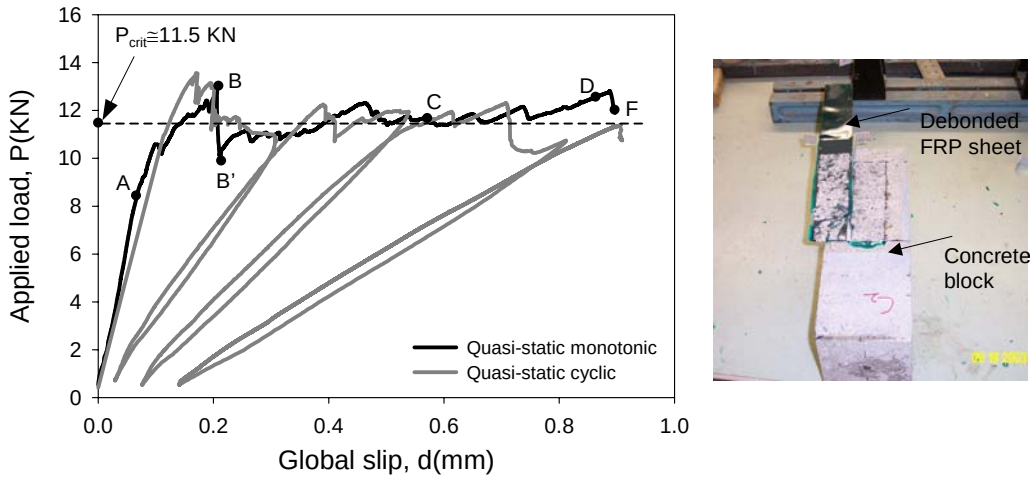

(a) **(b)**

Figure 3.4: Quasi-static monotonic and cyclic load responses; (a) Typical load versus global slip response of FRP bonded to concrete; (b) Photograph of a debonded specimen

3.5.2 Quasi-static monotonic

A typical load versus global slip response obtained from a direct shear test is shown in Figure 3.4a. It can be seen that as the global slip is increased, the initial load

response is approximately linear up to point A. The test response is nonlinear as the load is increased fro 8 to 12 KN (portion AB of the load response). There is a slight drop in the load at point B, following which the load levels off and essentially remains constant at P_{crit} approximately equal to 11.5 KN with increasing global slip up to failure (point F). In the subsequent discussion, the portions AB and BF of the load response are referred to as pre- and post-peak response, respectively. The final failure of the specimen at point F was sudden and produced by debonding, resulting in a complete separation of the FRP composite from the concrete substrate. Observation of the debonded FRP composite sheet indicated that the failure occurred in a thin interfacial layer close to the surface where the primer impregnates the concrete. A photograph of the specimen after failure is shown in Figure 3.4b. Five specimens were tested in the experimental program and the compiled results are shown in Table 3.2.

Table 3.2: Results from the quasi-static monotonic tests performed on FRP composite bonded to concrete

Specimen	P_{crit}(KN)	d(mm) at failure	$\overline{\tau}_{max}$ (MPa)	$\overline{s}_0$ (mm)	$\overline{G}_F$ (MPa.mm)
1	11.5	0.85	4.90	0.069	0.711
2	12.9	0.86	4.69	0.053	0.731
3	12.0	0.87	5.14	0.048	0.737
4	12.8	0.95	5.31	0.031	0.729
5	13.2	0.93	5.11	0.039	0.768
Average	12.48	0.89	5.03	0.048	0.735
Std. Deviation	0.705	0.044	0.239	0.014	0.021

During the quasi-static monotonic loading procedure, digital images were recorded at global slip increments of 0.025mm. Displacements and strain distributions were determined on the entire surface area of the FRP composite and on a 12mm wide

strip of concrete close to the FRP composite. The strain distribution in the FRP composite at distinct points of the load response is shown in Figure 3.5. These contours correspond to the strains in the axial direction (direction of load). In Figure 3.5, the upper edge of the bonded area corresponds to the loaded end of the FRP composite. Figure 3.5a shows the strain distribution in the linear part of the load response corresponding to an applied load equal to 8 KN. It can be seen that the strain is approximately zero up to a distance equal to 130 mm from the bottom. There is a rapid increase in strain (strain gradient) on approaching the loaded end.

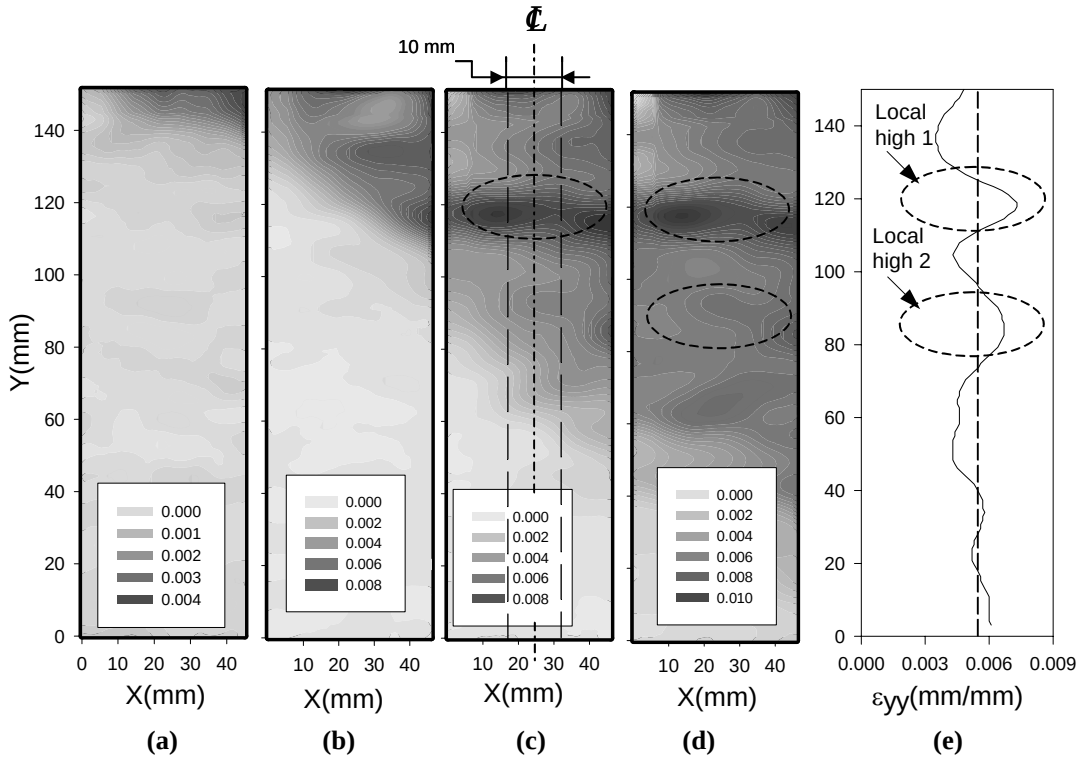

Figure 3.5: Strain contours corresponding to different load points in the load-global slip response: (a) At load point of 8 KN; (b) Load point in the region AB; (c) At point C; (d) At point D; (e) Strain distribution in the debonded FRP sheet at a load equal to 11.5 KN during the direct tensile test

The strain distribution at a typical load point falling between points A and B of the load response is shown in Figure 3.5b. It can be seen that the magnitudes of strain are larger when compared with the strains in the linear portion of the load response

(Figure 3.5a). The region of high strain gradient appears to be shifted downwards when compared with Figure 3.5a. The strain distributions at points C and D in the post-peak part of the load response are shown in Figures 3.5c and 3.5d, respectively. It can be seen that the region of high stress gradient moves further down along the length of the FRP composite as the global slip increases. Also, in Figures 3.5c and 3.5d, the strains appear to level off upon crossing the high strain gradient.

Strain gradients are typically produced by discontinuities such as a notch or a crack. The strain gradient in Figure 3.5a is caused by the notch in the interface close to the free edge of the concrete. The downward shift in the high strain gradient, noticed in Figure 3.5b, suggests that an interfacial crack between concrete and FRP composite initiates in the pre-peak portion of the load response. The images captured in the post peak, Figures 3.5c and 3.5d, confirmed that there is progressive crack propagation as the global slip increases.

3.5.3 Quasi-static cyclic

A typical quasi-static cyclic load response obtained by unloading the specimen from the quasi-static load envelope and reloading is shown in Figure 3.4a. It can be seen that there is a close correspondence between the load envelope obtained from the quasi-static monotonic and the cyclic tests; the quasi-static cyclic load response appears to follow the quasi-static load envelope upon reloading. This suggests that the quasi-static monotonic response acts like an envelope for the quasi-static cyclic response. There is a progressive change in the stiffness (an increase in the unloading compliance) with each additional load cycle. During each quasi-static cyclic test, digital images were recorded just prior to unloading from the load envelope and subsequently after the load reached

the load envelope upon reloading. The strain contours obtained from the analysis of digital images suggested that following each load cycle there was an increase in the crack length with increasing global slip.

3.6 Analysis of results

3.6.1 Quasi-static monotonic

Analysis of the axial strain in the FRP composite during the direct shear test was performed using the averaging procedure described previously. Averaging the strain across the width of a 10mm wide strip was done to minimize the influence of the material variation in the transverse (width) direction, the effect of the edges and possible load eccentricity during a direct shear test. The width of the strip was chosen equal to 10mm after considering the following: (a) averaging the strains across 1, 2 and 10 mm revealed insignificant differences in the axial strain distribution; (b) wider strips tended to smear the strain distribution produced by inclined cracks; and (c) the size of the aggregate used in concrete which forms the basis for deciding a representative volume is equal to 10mm. The strain distribution obtained using the averaging procedure along the length of the FRP obtained from Figure 3.5a corresponding to the linear part of the load response is shown in Figure 3.6a. It can be seen that the strain in the FRP away from the loaded end is approximately zero, after which it starts to increase exponentially as we approach the loaded end. The strain distribution obtained from the linear elastic theory (Taljsten 1997) is also plotted in the graph for comparison. Nominal values of the Young's modulus, the thickness and the width of the FRP composite were used to obtain the theoretical prediction. A good agreement, between the experimental strain

distribution and that obtained from the linear elastic theory, is observed for this load level.

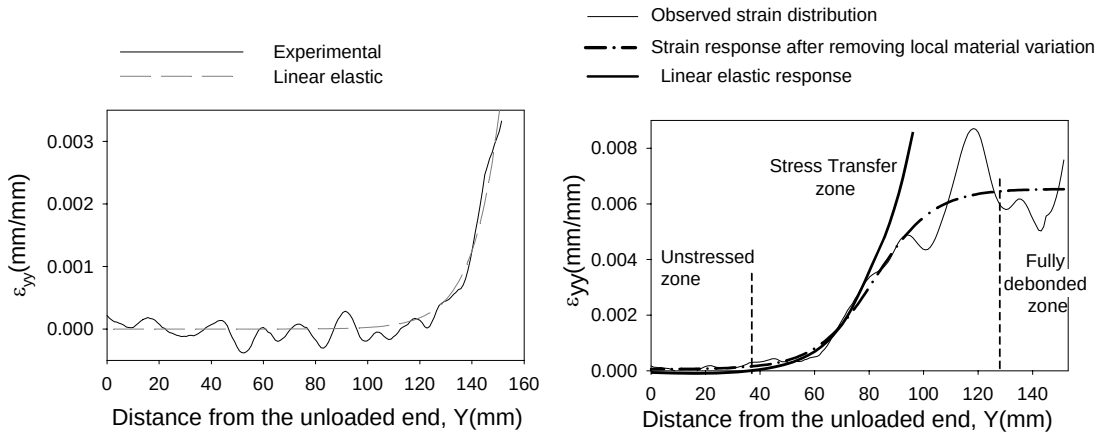

Figure 3.6: Experimental and theoretical strain distribution along the FRP sheet: (a) At early stage of loading; (b) At point C in the post-peak part of the load response

The strain distribution corresponding to point C in the post-peak part of the load-global slip response is plotted in Figure 3.6b. The fluctuations in the measured strain along the length of the FRP composite were found to be due to local material variations in the FRP sheet. The observed strain distribution along the FRP is again essentially equal to zero close to the unloaded end. A rapid increase in strain is observed as we approach the loaded end, following which the value of the strain levels off at a value approximately equal to 6500με. The observed strain distribution can thus be divided into three main regions: (a) the unstressed region; (b) the stress transfer zone; and (c) the fully debonded zone. Within the stress transfer zone, the strain distribution is approximately "S" shaped. The strain distribution obtained analytically from linear elastic theory is also plotted in Figure 3.6b for comparison (Taljsten 1997). It can be seen that the strain predicted by the linear theory approximately coincides with the measured strain initially but there is a significant deviation from the linear elastic

response as we approach the fully debonded zone. In the fully debonded zone, the strains are essentially constant and were found to remain unchanged with continuing loading. Further, the relative pattern of the strain distribution produced by the fluctuations was observed to remain unchanged in the fully debonded portion of the FRP.

To investigate the fluctuations in the axial strain produced by the local material variations in the FRP sheet, a uniaxial tension test was performed on the FRP composite sheet that was debonded from concrete for the specimen shown in Figure 3.5. Digital images were captured during the test. It was observed that the debonded FRP composite sheet behaves elastically up to failure. The ultimate strain and the effective Young's modulus of the debonded FRP composite sheet were found to be approximately equal to 1.9% and 205 GPa, which are comparable to the values for the pristine FRP composite laminates. The strain distribution in the debonded FRP sheet at a load equal to 11.5 KN during the tensile test is shown in Figure 3.5e. It can be seen that the local variations in the axial strain along the length of debonded FRP composite sheet (Figure 3.5e) correspond well with the observed strain variation in the quasi-static shear test. The local highs in the strain of the FRP composite sheet (Figure 3.5e) coincide with the location of the local highs in the strain obtained from the direct shear test (Figure 3.5c and 3.5d).

The nonlinear strain response in the stress transfer zone produced by shear stress transfer, independent of the local material variations of the FRP, was approximated using the following expression:

$$\varepsilon(y) = \varepsilon_o + \frac{\alpha}{1 + e^{(-\frac{y - y_o}{\beta})}} \tag{3.1}$$

where α, β, y_o, and ε_o were determined using nonlinear-regression analysis of the measured DIC strains. For the strain distribution shown in Figure 3.6b, the values of α, β, y_o and ε_o were obtained as 6.3×10^{-3}, 10.87, 82.02, and 5.65×10^{-5} respectively. From the analysis of data, ε_o was found to be approximately equal to the accuracy in the measured strain and was set equal to zero for subsequent analysis. The strain distribution obtained from Equation 3.1 is also plotted in Figure 3.6b, for comparison.

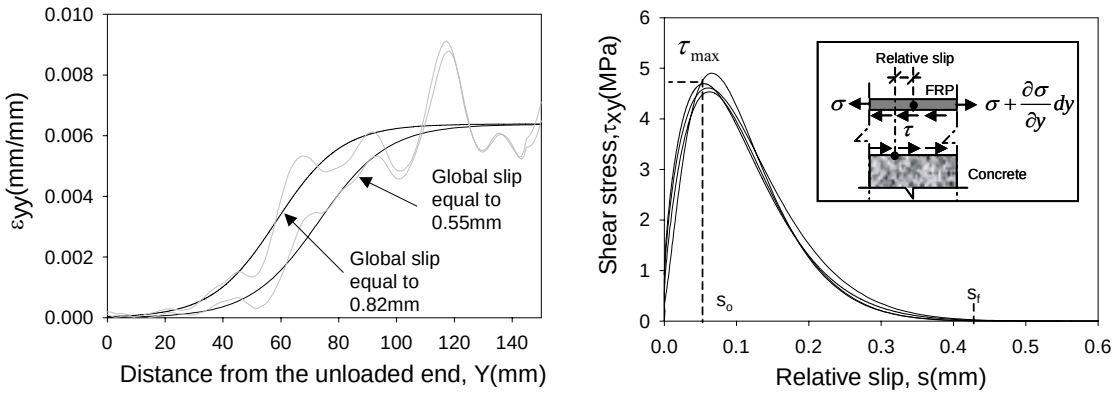

(a) **(b)**

Figure 3.7: FRP Strain distribution and interfacial material law; (a) Strain distribution along the FRP sheet corresponding to two different points in the post-peak part of the load-slip response; (b) Material law of FRP/concrete interface

Figure 3.7a shows the strain distribution along the FRP obtained using Equation 3.1 (after removing the influence of local material variations) at two different points in the post-peak part of the load-global slip response. It can be seen that as the global slip increases, the length of the fully debonded zone increases and the stress transfer zone exhibits a lateral shift, without stretching, towards the unloaded end. It can also be noticed that the size and the shape of the stress transfer zone remain unchanged in the two cases. The length of the stress transfer zone is constant at approximately 90 mm.

Therefore, it can be inferred that the strain distribution in the stress transfer zone in the post-peak part of the load response is self-similar.

The load response of the specimen can now be interpreted in terms of the observed crack growth. Initially, the material response at low levels of load is linear. As the crack initiates and begins to grow, the load response becomes nonlinear. The peak load is reached when the interfacial crack length becomes equal to a critical value. Subsequently, the crack grows in a self-similar manner at a constant load. As the crack advances, the compliance of the specimen (inverse of the stiffness) increases, which manifests itself in increased global slip. The self-similar crack growth is associated with a characteristic length, which corresponds to the stress transfer zone. As the crack advances, the stress transfer zone, which is similar in shape, moves along the bonded length of the FRP as a longer length of the FRP composite is fully debonded.

3.6.2 Material law for interfacial bond

The measured displacements and strain distributions in the FRP composite and the concrete provide a means for determining the material law for the interfacial bond. The interfacial material law provides a relationship between the shear stress and the relative displacement between FRP and concrete. The following assumptions were made in the analysis:

1. The FRP composite is linear elastic up to failure.
2. The thickness and the width of the FRP sheets are constant along the bonded length (the material properties of the FRP composite are based on the net area of the fibers).
3. The interface is subjected only to shear loading.

4. The interface between the FRP and the concrete is assumed to be of infinitesimal thickness.

From the measured strain in the FRP, the interfacial shear stress at any location was obtained using the following relationship (Taljsten 1997):

$$\tau(y) = t\,E\,\frac{d\varepsilon(y)}{dy} \tag{3.2}$$

where $\tau(y)$ is the shear stress distribution along the interface of FRP and concrete at any location y; E is the elastic modulus of the FRP composite; t is the thickness of the FRP composite; and $\varepsilon(y)$ is the axial strain distribution in the FRP. From Equation 3.2, it can be seen that the magnitude of the shear stress depends upon the gradient of the axial strain in the FRP composite. The next step of the analysis consisted of determining the relative slip between the FRP and the concrete along the length of the FRP composite sheet. It was found that the axial displacements measured on the concrete surface were insignificant when compared with that of the FRP composite. The relative slip, s(y), between FRP and concrete at a given location on the FRP was obtained by integrating the axial strain in the FRP up to that point. By combining the shear stress and relative slip at different locations along the length of the FRP, the material law for the FRP/concrete interface was obtained. The interfacial material behavior obtained in this manner for the specimen with the quasi-static monotonic response of Figure 3.4a is shown in Figure 3.7b. The continuous curves in Figure 3.7b correspond to the material law obtained from the strain distribution measured at different points in the post-peak part of the load response for this specimen. A close agreement between the interfacial material responses determined from the different crack locations is observed. This

further confirms the self-similarity of the crack propagation process in the post-peak portion of the load-global slip response.

It can be seen that the shear stress versus relative slip response for the FRP/concrete interface exhibits a softening response. The response is initially approximately linear up to 40% of the maximum shear stress, after which it is nonlinear up to the peak stress (τ_{max}). After τ_{max}, a softening is observed where increasing relative slip results in a decreasing interfacial shear stress transfer along the interface. The shear stress drops to zero when the relative slip is equal to s_f (shown in Figure 3.7b). Increasing relative slip beyond s_f would result in a complete separation of the FRP from the concrete at that location. From the material law, the area under the "τ-s" curve representing the interfacial fracture energy, G_F, is obtained by numerical integration of Equation 3.3 (Bazant & Planas 1998):

$$G_F = \int \tau \, ds \tag{3.3}$$

The average values of τ_{max}, s_o, and G_F corresponding to different points in the post-peak part of the load-global slip response were obtained for all the quasi-static monotonic specimens and are tabulated in Table 3.2. It can be seen that values of the fracture parameters obtained from different specimens are in close agreement.

3.6.3 Quasi-static cyclic

The strain distribution along the length of the FRP just prior to unloading in the second load cycle from the quasi-static cyclic test of Figure 3.4a is shown in Figure 3.8. The strain distribution at the corresponding value of global slip obtained from the quasi-static monotonic load response is also shown in Figure 3.8 for comparison. It can be seen that the strain distribution in the stress transfer zone obtained from the quasi-static

cyclic test is comparable to that obtained from the quasi-static monotonic response. Further, the strain distribution in the stress transfer zone determined for different points on the load envelope from the quasi-static cyclic tests was found to be identical. Thus, it can be concluded that cycling the load to the quasi-static load envelope does not alter the stress distribution in the stress transfer zone on the load envelope. Between successive load cycles, the stress transfer zone was found to move along the bonded length of the FRP composite.

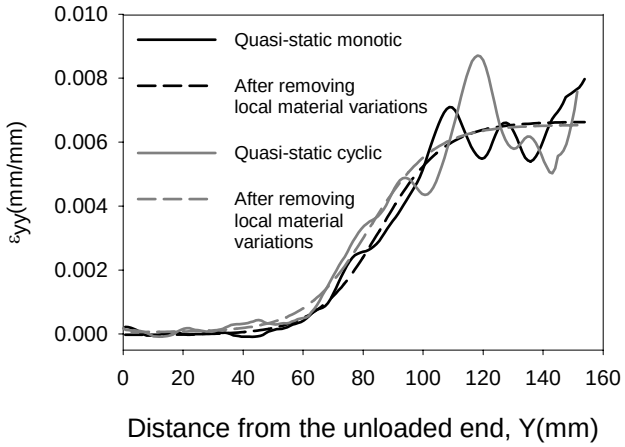

Figure 3.8: Strain distribution versus location along the FRP for quasi-static monotonic and quasi-static cyclic tests

The fracture energy can be calculated from the energy dissipated between two successive load cycles in the load versus global slip curve. The dissipated energy is associated with the increase in the crack length and is graphically obtained as the area enclosed by the load cycles. Therefore, the fracture energy is obtained as the total area between two loading cycles divided by the increase in crack length. The strain energy between two loading cycles, which is equal to the fracture energy required to drive the crack for a length δa, is then obtained from the area under the curve. For the specimen response shown in Figure 3.4, the energy releases rate G_F is calculated as:

$$G_F = \frac{\delta U}{\delta a \times b} = \frac{(Area\ between\ two\ cycles)^{(KN/mm)} \times 10^{3\ (N/KN)}}{\delta a^{(mm)} \times b^{(mm)}}$$
$$= \frac{2.25624 \times 10^3}{(92-22) \times 46} = 0.7\, MPa \times mm \tag{3.4}$$

where δU is the strain energy dissipated in one cycle, δa is the change in crack length in one cycle and b is the width of the FRP. The value of G_F obtained from the load response corresponds closely with that obtained from the material law. This provides an additional check of the validity of the proposed material law.

3.7 Discussion

Experimental evidence suggests that after initiation, crack propagation due to debonding occurs at a constant load. Further, the distribution of stresses in the stress transfer zone is self-similar during this process. This suggests that the energy associated with the stress transfer zone does not change during crack growth. Further, it can be postulated that the stress transfer zone has a constant compliance (stiffness). It has also been shown that once fully debonded, the FRP sheet essentially behaves like an elastic material. The process of debonding between the FRP and concrete can thus be schematically represented as shown in Figure 3.9a. In this representation, the fully debonded FRP sheet and the stress transfer zone are represented by springs having different stiffnesses. The fully debonded FRP sheet has a constant stiffness per unit length and the spring stiffness of the entire stress transfer zone is constant. The load point displacement is thus obtained by considering the compliances of the stress transfer zone (L_c) and the fully debonded length of the FRP (L). As the crack advances, the fully debonded region increases, which can be represented by increasing the length of the spring associated with the fully debonded portion (L+ΔL). The increase in the load point

displacement, δd, is thus a result of the displacement associated with an increase ΔL of the fully debonded spring under a constant load. Since the load remains constant, it can be seen that as the crack grows in length, the elastic energy in the fully debonded portion increases quadratically with the debonded length increment. Thus, close to failure, when the stress transfer zone reaches the end of the bonded region, the release of the elastic energy available in the FRP sheet can produce unstable failure. Further, the larger the fully debonded length at failure, the higher the elastic energy in the debonded spring and hence the more unstable is the final failure.

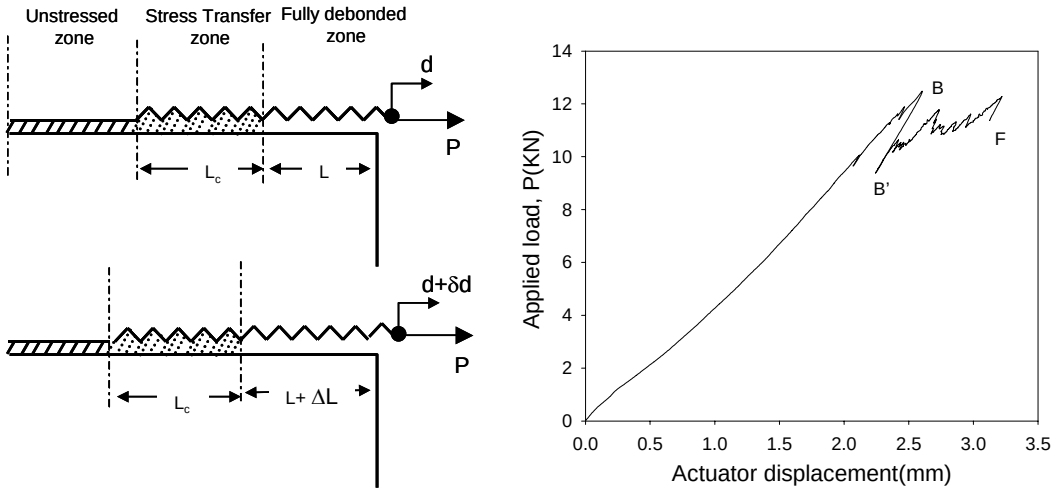

(a) **(b)**

Figure 3.9: Snapback instability; (a) Schematic representation of the debonding process; (b) Snapback instability in the load-displacement response

Considering the schematic representation, it can now be shown that the load-global slip response at failure after significant debonding would exhibit snapback. After significant debonding, the measured global slip includes the elastic deformation of a large length of fully debonded FRP. At this stage, elastic deformations associated with the fully debonded FRP contribute significantly to the overall measured global slip. A

snapback behavior in the load response would result from the elastic unloading of the fully debonded FRP at failure.

The snapback behavior can be illustrated considering the load versus actuator displacement response shown in Figure 3.9b. Actuator displacement includes the elastic deformation of the initially unbonded FRP (L_i of Figure 1c) in addition to the global slip. Thus, the observed drop in load associated with feature $BB^{/}$ of the load-global slip response in Figure 3.4a, manifests itself as snapback in the corresponding load versus actuator displacement response shown in Figure 3.9b. Therefore, it can be inferred that the uncontrolled failure at point F for the test performed in global slip control is due to snapback instability. To better control the test and capture the full load response of the specimen up to complete debonding (down to zero load), the elastic displacement of the debonded FRP sheet has to be subtracted from the global slip using a combined feedback signal (Subramaniam et al. 1998).

3.8 Conclusions

In this chapter, the shear debonding of FRP composite from concrete is studied using digital image correlation. Using the optical technique allowed for the mapping of the complete strain field, which resulted in an accurate estimation of the nonlinear interfacial material law.

Based on the results presented in this chapter, the following conclusions can be drawn:

1) The progressive debonding of FRP attached to a concrete substrate is produced by an interfacial crack, which forms and propagates along the interface between the concrete and the FRP. The load versus global slip response of the FRP/concrete bond can be

divided into pre and post-peak parts. The observed crack initiates in the pre-peak part of the load response.

2) Once the crack initiates in the interface, it initially grows in a stable manner with increasing stress. Once the crack reaches a critical length, it propagates in a self-similar manner at a constant load in the post-peak part of the load response. This steady crack growth is responsible for the increase in the global slip of the FRP relative to concrete.

3) In the post-peak part of the load response, there is a constant stress transfer length between the concrete and the FRP sheets, which was found to be approximately equal to 90 mm. The stress transfer zone advances along the bonded length of FRP as the crack propagates.

4) Direct tensile tests on FRP sheets debonded from the concrete surface confirmed that the load response was identical to that of the pristine FRP composite sheet.

5) The fracture energy, which is required to create a unit surface area of the interfacial crack, was found to be constant and independent of the location of the crack along the interface.

6) The quasi-static monotonic load response acts like an envelope for the quasi-static cyclic response.

7) Cycling the load to and from the quasi-static load envelope does not change the stress distribution in the stress transfer zone. Repeated cycling from and to the load envelope produces a change in the global compliance of the specimen associated with crack propagation.

8) The interfacial stress distribution obtained from points on the post-peak load envelope in the quasi-static monotonic and the quasi-static cyclic were identical.

9) The ultimate failure during debonding of FRP from the concrete substrate is associated with snapback instability.

CHAPTER 4

FREEZE-THAW DEGRADATION OF FRP-CONCRETE INTERFACE: IMPACT ON FRACTURE PARAMETERS

4.1 Overview

In recent years, there has been an increased interest in the application of externally bonded fiber reinforced polymer (FRP) sheets for strengthening deteriorated concrete structures. Although previous studies have demonstrated the merits of using FRP composites for strengthening beams, a number of issues related to the debonding failure in the FRP-concrete interface and the lack of a clear understanding of the long-term performance of FRP-based repairs, are hampering their widespread implementation. Of particular interest is the behavior of the interfacial bond in harsh environmental conditions such as the effect of freeze-thaw cycles. This chapter presents an experimental investigation of the effects of freeze-thaw cycling on the interfacial bond behavior. The strain distributions in the concrete and FRP are determined using the displacements obtained from an optical technique based on digital image correlation (DIC). The results of the strain analysis are used to establish the non-linear material law for shear fracture along the FRP-concrete interface for specimens subjected to freeze-thaw cycles. The influence of freeze-thaw on the parameters of the material law was evaluated using a statistical significance analysis. The results show that freeze-thaw

cycling produces a statistically significant decrease in the ultimate load transferring capacity, interfacial fracture energy and the parameters of the interface material law.

4.2 Introduction

The concrete infrastructure in the United States is deteriorating and highway bridges, many of which were built more than four decades ago, are in need of major rehabilitation. The urgent need to rebuild the nation's infrastructure spurred substantial new research effort to develop effective repair and rehabilitation strategies for existing structures. Specifically, the use of fiber reinforced polymer (FRP) composites has generated considerable interest for application in retrofitting degraded infrastructure in general and bridge structures in particular. Because of the enormity of the problem related to rehabilitating the U.S. bridge inventory, transportation agencies are exploring the possibility of using FRP repair technology on a large scale to extend the useful lives of existing bridges while simultaneously reducing the costs and the disruption to traffic associated with the application of traditional rehabilitation procedures (Hag-Elsafi et al. 2001). Although several pilot studies have demonstrated the merits of using FRP composites and their reliability over the limited period of monitoring, a number of issues are hampering the widespread implementation of this technology. These issues are primarily related to the long-term reliability and durability of FRP materials and the lack of a common set of design specifications for FRP repairs.

Considerable experience with the short and long term performances of FRP composites currently exists as these materials have been in use in various industries for many years, including the aerospace and automobile industries (Daniel and Ishai 1994). A complete understanding of the load response of FRP strengthened concrete structures

and the stress transfer between concrete and FRP is however still emerging (Meier and Kaiser 1991, Saadatmanesh and Malek 1998, Karbhari et al. 1996, De Lorenzis et al. 2001). It has been shown that debonding in the FRP-concrete interface is produced by a crack that propagates along the interface of the two materials and leads to premature failure of the strengthened structure (Triantafillou and Pelvris 1990, Lopez Acevedo et al. 2000). Several experimental investigations of the FRP-concrete bond response have been undertaken and different analytical formulations for the interface material behavior under quasi-static loading have recently been proposed (Taljsten 1997, Ueda et al. 1999, Bizindavyi and Neale 1999, Wu and Niu 2000, De Lorenzis et al. 2001, Yuan et al. 2001, Leung and Tung 2001, Ali-Ahmad et al. 2005). However, the primary concern for the application of FRP to civil infrastructure repair is the long-term behavior of the bond between the FRP composite and the existing structure under harsh environmental conditions. The progressive degradation of the FRP composite and the interfacial FRP-concrete bond, which could result in a steady decrease in the load carrying capacity and hence the service performance of the strengthened/retrofitted structural elements, need to be evaluated. In northern parts of the U.S., the effects of freeze-thaw cycles are of particular concern.

The information in the literature pertaining to the effect of freeze-thaw damage on the interfacial bond is not consistent. For instance, Bisby and Green (2002) observed that little, if any, damage to the FRP-concrete interfacial bond resulted from freeze-thaw cycles, while Mukhopadhyaya et al. (1998) concluded that freeze-thaw cycling affects the stress transfer between the concrete and the FRP as well as the amplitude of the shear stress distribution along the FRP bonded length. Grace and Sing (2005) observed

that freeze-thaw cycling decreases the load-carrying capacity of reinforced concrete beams strengthened using CFRP plates and fabrics by up to 13%. Lopez Acevedo et al. (2000) observed a decrease in the ultimate load and the mid-span deflection in RC beams strengthened using externally bonded FRP sheets with an increase in the number of freeze-thaw cycles. The only consistent results found in the literature pertain to the observed change in the mode of failure and the measured increase in the slip between concrete and FRP, in specimens subjected to freeze-thaw cycles. In beams exposed to freezing and thawing cycles, the failure of the interfacial bond was observed to occur along the FRP-adhesive interface while the failure occurred in the concrete-adhesive interface in beams tested under normal temperatures. Also, no standard accelerated test method for studying the influence of freeze-thaw damage on the interfacial bond is currently available. Therefore, researchers have used different cycling schedules and methods. For instance, Mukhopadhyaya et al. (1998) subjected the specimens to freeze-thaw cycles between -17.8^{o}C and 20^{o}C for one week at the rate of two cycles per day. Freeze-thaw cycling was interrupted by a one-week period where the specimens were immersed in a salt solution. Bisby and Green (2002) subjected strengthened beams to one freeze-thaw cycle a day. Each cycle consisted of freezing in air at -18^{o}C for 16 hours and thawing in water at 15^{o}C for 8 hours. Grace and Sing (2005) exposed RC beams strengthened using FRP to one freeze-thaw cycle every 4 hours. The temperature was varied between -17.8^{o}C and 0^{o}C. Despite the available findings in these limited investigations, a comprehensive evaluation of the influence of freeze-thaw cycling on the material law for the interface and the interfacial fracture parameters is currently not available.

In this chapter, the impact of freeze-thaw cycling on the interfacial bond between FRP and concrete is investigated. Direct shear tests were performed on specimens subjected to 100, 200, and 300 freeze-thaw cycles. The effect of the freeze-thaw cycling on the interfacial fracture parameters and the shear stress transfer between the concrete and the FRP is investigated using a full field optical technique known as digital image correlation (DIC). The non-linear material law for shear fracture along the FRP-concrete interface is also determined. Fracture parameters are obtained for the interfacial crack growth in specimens with and without freeze-thaw damage. The impact of freeze-thaw degradation on the fracture parameters and the stress transfer characteristics is analyzed using a statistical significance analysis.

4.3 Objectives

The objectives of this chapter are: (a) to study the influence of freeze-thaw cycling on the progressive debonding process at the interface between concrete and FRP; (b) to determine the effect of freeze-thaw cycling on the stress transfer between the adherents; (c) to establish the material law for the interfacial bond between the concrete and the FRP in specimens subjected to freeze-thaw cycles; and (d) to evaluate the influence of freeze-thaw cycles on the interface fracture parameters.

4.4 Materials and experimental procedure

In the experimental program, the bond between FRP and concrete was investigated using a direct shear test. Specimens with and without freeze-thaw damage were tested to determine the stress transfer during debonding. The material law for the FRP-concrete interface was then established using the results of the stress analysis.

The concrete specimens used for direct shear tests consisted of prismatic blocks having the following nominal dimensions: length (330mm), width (125mm), and height (125mm) as shown in Figure 4.1. Three prismatic block specimens and companion cylinders (75mm×150mm) were cast from every batch of concrete. The details of specimen preparation and material characteristics are reported in greater detail in Chapter 3.

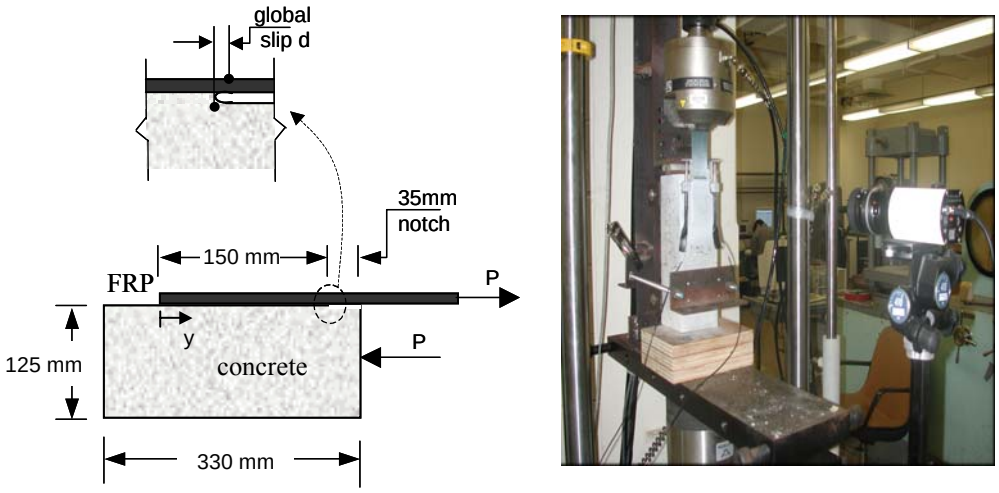

Figure 4.1: Dimensions of specimens used in direct shear tests and the Test setup

After installing the FRP composites, the epoxy was allowed to cure in the laboratory environment for one week before subjecting the strengthened concrete blocks (with FRP attached) to freeze-thaw cycles. Specimens subjected to freeze-thaw cycling were placed in an environmental chamber at 99% RH and 22^{o}C for one day before initiating the thermal cycling. Two specimens from each batch of concrete were subjected to freeze-thaw cycling while the third specimen was stored in the laboratory environment for the same duration and was used as the control specimen. Direct shear tests were then performed on all specimens.

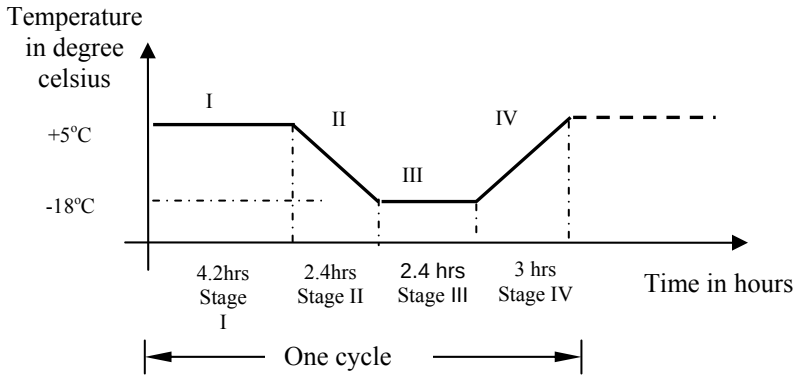

Figure 4.2: Schematic representation of the temperature variation in one freeze-thaw cycle

4.4.1 Freeze-thaw experimental program

An accelerated freeze-thaw testing procedure was developed whereby the specimens were subjected to two cycles of freezing and thawing per day in an environmental chamber. The temperature variation of the chamber during one freeze-thaw cycle is shown in Figure 4.2. One freeze-thaw cycle consisted of four stages. In stage I, the temperature was held constant at +5°C for 4.2 hours. The duration of stage I was found sufficient for the surface temperature of the concrete and the FRP to reach +5°C. Stage II consisted of rapid freezing to -18°C in approximately 2.4 hours. The rate of freezing and cooling in stages II and IV was determined based on the recommendation in ASTM-C666 (2000) for plain concrete. The temperature was held constant at -18°C for 2.4 hours in stage III. The duration of this stage was determined through trial-and-error to ensure thermal equilibrium and the formation of ice on the concrete and FRP surfaces. Stage IV consisted of raising the temperature to +5°C in 3 hours. The temperature profile was programmed into the computer interface provided with the freeze-thaw chamber. To ensure that the concrete surface was kept moist during the thawing phase, water was sprayed in the middle of the thawing phase of the freeze-

thaw cycle every two days to compensate for losses due to evaporation. The concrete surface was kept moist and the entire specimen was not immersed in water as suggested by other researchers (Grace et al. 2005, Green et al. 2002) to simulate field conditions where the FRP composite is applied to the bottom of bridge beams, which does not permit standing water.

4.4.2 Testing procedures and measurements

The direct shear test used for evaluating the FRP-concrete interfacial bond response comprised of the classical "pull-push" configuration (Taljsten 1996, Ueda et al. 1999, Ali-Ahmad et al. 2005). During each test, a tensile force was applied to the FRP composite, while the concrete block was restrained from movement. The sliding displacement between the FRP and the concrete for points initially located at the tip of the notch is referred to as "global slip", d, throughout this chapter (shown schematically in the inset of Figure 4.1a). All direct shear tests were performed using the global slip as the control variable; the global slip was increased at a constant rate of 0.00065 mm/sec up to failure.

The displacements of points at the surface of the FRP composite were obtained using the digital image correlation (DIC) technique (Sutton et al. 1983, Ali-Ahmad et al. 2004). Digital images of the specimen surface prior to loading and at regular intervals during the loading process were captured and stored for later analysis. A photograph of the test setups for the direct shear test and for the image acquisition is shown in Figure 4.1. Surface displacements were determined at each stage of loading using a cross correlation analysis of the digital images (Sutton et al. 1983, 1988, Bruck et al. 1989). A 2-D displacement field was obtained for all points on the FRP surface. The strains were

then computed as the gradients of the displacements. DIC when compared with conventional techniques offers the advantage of obtaining spatially continuous measurements of displacements using normal white light. The accuracy in the measured displacements and the calculated strains, for the setup used in this study, were equal to 1×10^{-6}m and 50με, respectively (Sutton et al. 1983, 1988, Bruck et al. 1989).

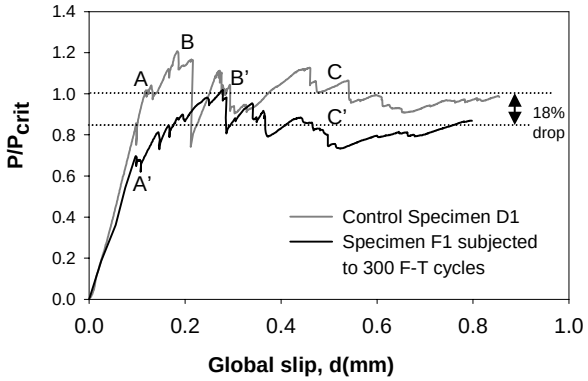

Figure 4.3: Normalized load versus global slip response from direct shear test

4.5 Experimental results

Typical load versus global slip responses of a specimen subjected to 300 freeze-thaw cycles and its control are shown in Figure 4.3. From the load response of the control specimen, the load initially increases linearly with increasing global slip up to point A. The load response becomes non-linear in the portion AB where increasing slip is still associated with an increase in the load up to the peak load. There is a sudden drop in the load at point B. After point B, the load levels off and stays approximately constant at P_{crit}. P_{crit} was determined as the mean value of the load when the global slip varied between 0.35 and 0.7mm. The reason for selecting the stated range for determining, P_{crit}, was based on the results of the strain analysis and is explained later in the chapter. P_{crit} was found to be equal to 11.2 KN for the control specimen of Figure 4.3. In the

subsequent discussion, the portions AB and BC of the load response are referred to as pre- and post-peak responses, respectively. In Figure 4.3, the values on the vertical axis for both specimens have been normalized with respect to P_{crit} of the control specimen.

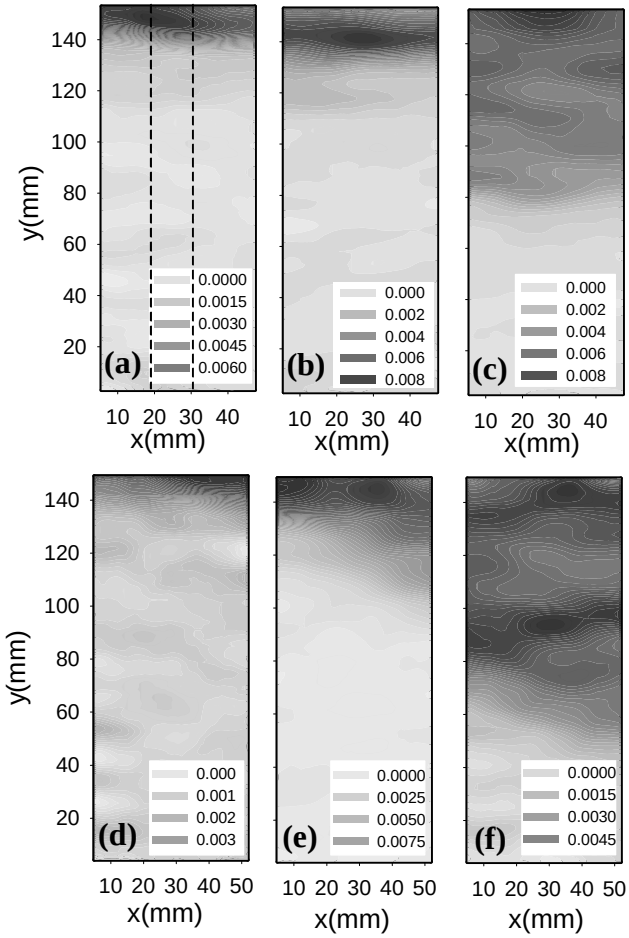

Figure 4.4: Strain contours at different points of the load-global slip responses: (a) at point A; (b) at point B; (c) at point C; (d) at point A' ; (e) at point B' ; and (f) at point C'

During the test, digital images were recorded at global slip increments of 0.025mm. The strain contours for ε_{yy} (strain along the length/axial direction of the FRP) on the FRP surface corresponding to points A, B and C on the load response of the control specimen are shown in Figures 4.4a, 4.4b and 4.4c, respectively. In Figure 4.4, the upper edge of each plot corresponds with the loaded end of the FRP composite.

From the strain distribution at point A in the pre-peak response of the control specimen (Figure 4.4a), it is observed that the lower portion of the FRP has relatively no strain. Moving towards the loaded end, a large strain gradient can be observed in a small region close to the notch. High strain gradients are typically observed in regions close to a stress riser such as a notch or a crack. The region of high strain gradient at point B of the load response is shifted downwards indicating the initiation of an interfacial crack prior to the peak load. The strain distribution at point C of the load response of the control specimen shows that the region of high strain gradient moves further away from the loaded end. This observation confirms that there is progressive crack propagation with an increase in the global slip.

Table 4.1: Compiled data of the fracture parameters

# of f-t cycles	P_{crit}^{cont} (KN)	$\frac{P_{crit}^{F\text{-}T}}{P_{crit}^{cont}}$	E_{FRP} (MPa)	L_{STZ} (mm)	ε_{yy}^{max} (με)	G_F (MPa.mm)	τ_{max} (MPa)	s_o (mm)	s_f (mm)
0	11.44	1	252-216 μ=240 σ=9	100-80 μ[(1)]=92 σ=5.9	6450-5600 μ=6100 σ=300	0.77-0.52 μ=0.65 σ=0.08	7.69-4.70 μ=5.97 σ=0.99	0.069-0.023 μ=0.038 σ=0.010	0.25-0.14 μ=0.18 σ=0.03
100	10.83[(2)]	0.92	280-220 μ=243 σ=20	85-75 μ=82 σ=5.8	5200-4700 μ=5000 σ=200	0.45-0.36 μ=0.41 σ=0.03	6.34-4.87 μ=5.75 σ=0.62	0.033-0.016 μ=0.026 σ=0.005	0.14-0.10 μ=0.11 σ=0.02
200	12.28	0.88	270-205 μ=239 σ=33	85-70 μ=78 σ=4.4	6100-4900 μ=5600 σ=400	0.59-0.39 μ=0.50 σ=0.07	6.30-4.20 μ=5.16 σ=0.66	0.040-0.021 μ=0.034 σ=0.007	0.18-0.1 μ=0.14 σ=0.03
300	11.21	0.83	268-229 μ=247 σ=16	75-60 μ=68 σ=5.3	5000-4350 μ=4700 σ=200	0.53-0.33 μ=0.42 σ=0.07	5.95-3.85 μ=4.85 σ=0.73	0.031-0.018 μ=0.024 σ=0.004	0.15-0.09 μ=0.12 σ=0.02

(1) μ is the mean; σ is the standard deviation;

(2) P_{crit}^{cont} is determined as the average value of the load within one control specimen.

A slight decrease in the initial stiffness and an extended non-linear zone prior to the peak load can be observed in the freeze-thawed specimen relative to the control by comparing regions AB and $A'B'$ in Figure 4.3. There is also a noticeable drop (approximately 18%) in the load carrying capacity in the specimen subjected to freeze-thaw cycles. Similar behavior was obtained from all specimens tested. The values of

$P_{crit}^{F\text{-}T}$ for the freeze-thawed specimens are shown in Table 4.1. The $P_{crit}^{F\text{-}T}$ values in Table 4.1 for specimens subjected to a given number of freeze-thaw cycles were normalized with respect to P_{crit} for the control specimen from the same batch of concrete. The average values obtained from all the specimens subjected to a given number of freeze-thaw cycles are reported in Table 4.1. The results indicate a consistent decrease in $P_{crit}^{F\text{-}T}$ with an increase in the number of freeze-thaw cycles.

The strain contours of ε_{yy} on the FRP surface corresponding to points A', B' and C' on the load response of the freeze-thawed specimen of Figure 4.3 obtained using the DIC procedure are shown in Figures 4.4d, 4.4e and 4.4f, respectively. From Figures 4.4b and 4.4e, it can be seen that there is a larger portion of the high strain region in the freeze-thawed specimen when compared with the control. Comparing the axial strains obtained at C and C' where the global slip in the control and the freeze-thawed specimens is equal to 0.5mm, it can be seen that the area of high strain gradient is lower in the freeze-thawed specimen than that in the control. This indicates a larger crack in the freeze-thawed specimen; which can be attributed to additional damage introduced in the FRP-concrete interface due to freeze-thaw cycling.

After complete debonding, the failure surfaces were examined to study the fracture mechanism. Observations of the debonded FRP sheet indicated that failure occurred in a thin layer close to the surface where the primer impregnates the concrete. A thin layer of concrete is attached to FRP composite sheets detached from the specimens. A slight, yet noticeable change in the failure mode due to freeze-thaw cycling was noticed. Observations on the debonded FRP composite sheets revealed that

the failure occurs through a plane, which is closer to the FRP sheet in the freeze-thawed specimens.

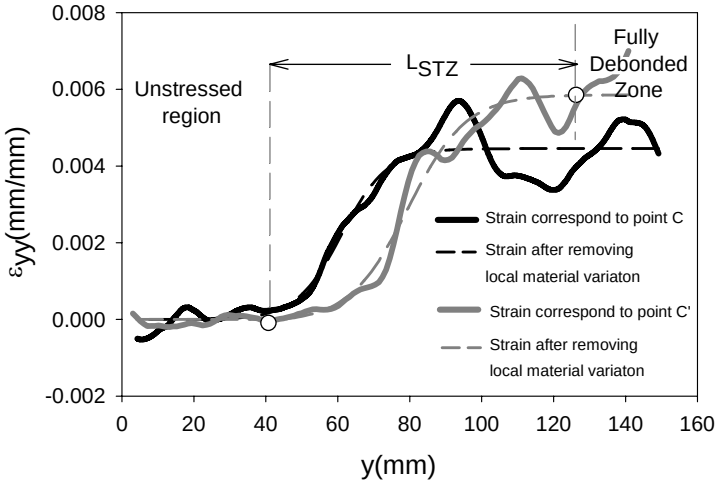

Figure 4.5: Strain distribution along FRP composite at Points C and C' of the control and freeze-thaw specimens, respectively

4.6 Analysis of results

4.6.1 Strain analysis

The strain variation along the length of the FRP was determined by averaging the strains across the width of a 10 mm strip in the center of the FRP composite sheet (as shown in Figure 4.4a by the dotted rectangle). More details on the averaging procedure are given in Ali-Ahmad et al. (2004 and 2005). The axial strains along the length of the FRP corresponding to points C and C' of the load-global slip responses are given in Figure 4.5. The global slip at C and C' in both specimens is equal to 0.5mm. The observed strain along the FRP is essentially equal to zero close to the unloaded end. A rapid increase in strain is observed as we approach the loaded end, following which the values of the strains level off at approximate values on the order of 6100με and 4700με for the control and the freeze-thawed specimens, respectively. The observed strain

distributions in both specimens can thus be divided into three main regions: (a) the unstressed region; (b) the stress transfer zone (STZ); and (c) the fully debonded zone. Within the STZ, the strain distribution is approximately "S" shaped. The stresses are transferred across the interface in the STZ, which is associated with a length, L_{STZ}. The strains within the unstressed and the fully debonded zones remain nominally constant with location at a given point in the load response. The oscillations in the measured strain were previously shown to reflect the presence of material inhomogeneities in the FRP composite and the interface (Ali-Ahmad et al. 2005). The strain variation produced by these material inhomogeneities is superimposed over that produced by the debonding process. The nonlinear strain response in the STZ produced by shear stress transfer, independent of the local material variations of the FRP, was approximated using the following expression:

$$\varepsilon(y) = \varepsilon_o + \frac{\alpha}{1 + e^{(-\frac{y - y_o}{\beta})}} \tag{4.1}$$

The parameters of Equation 4.1 were determined using nonlinear-regression analysis of the measured DIC strains. The strain distribution obtained after removing the influence of the local material inhomogeneities in the FRP composite are plotted using dashed lines in Figure 4.5. The strains in the STZ increase with an increasing distance from the unloaded end and asymptotically approach the constant value of the fully debonded FRP. The length of STZ, L_{STZ}, determined at different points of the post-peak load response from a given specimen was found to be approximately constant. Analysis of the results revealed that the STZ is fully established, free of boundary effects, for global slip in the range of 0.35-0.7mm. The results of this analysis were used to establish the range of global slip used to obtain the value of P_{crit} of the load response.

The effect of the freeze-thaw cycles on the stress transfer during debonding of the FRP composite from the concrete substrate is clearly observed in Figure 4.5. Although the strain distribution in the STZ of the freeze-thaw damaged specimen has the same shape as that observed in the control specimen, there is a decrease in L_{STZ}. Also, it is clearly seen that the strain in the FRP in the fully debonded zone, ε_{yy}^{max}, decreases from an average of 6100 με in the control specimens to 4700 με in the specimens subjected to freeze-thaw cycles. For each specimen tested, the strains in the FRP were determined in the entire post-peak load response at intervals of global slip (d) equal to 0.025mm. Some scatter was observed in the values of L_{STZ} obtained from within one specimen. The values of L_{STZ} and ε_{yy}^{max} obtained from all specimens tested are summarized in Table 4.1. It is clearly seen that there is an overall decrease in L_{STZ} and ε_{yy}^{max} with increasing number of freeze-thaw cycles. This decrease can be attributed to the damage induced by freeze-thaw cycling. It can therefore be inferred that the damage due to freeze-thaw cycling results in a decrease in the length of the FRP involved in transferring the stress across the interface during debonding.

The elastic modulus, E_{FRP}, of the fully debonded FRP composite was obtained using the measured strains, ε_{yy}^{max}, the corresponding applied load and the cross sectional area of the fibers contained in the composite sheet. The E_{FRP} was based on the cross-sectional area of the fibers contained in the composite (Replark System Technical Manual 2000). The average values of E_{FRP} for all specimens are reported in Table 4.1. It can be seen that freeze-thaw cycling did not affect the elastic modulus of the debonded FRP composite sheet. Therefore, this implies that the observed drop in ε_{yy}^{max} can be solely

attributed to a decrease in the load carrying capacity of the interface. Further, it has previously been shown that the elastic modulus of the debonded FRP composite sheet is equal to that of a pristine composite sheet (Ali-Ahmad et al. 2005). Therefore, it can also be inferred that freeze-thaw cycling, within the range considered in this chapter, does not influence the elastic modulus of FRP.

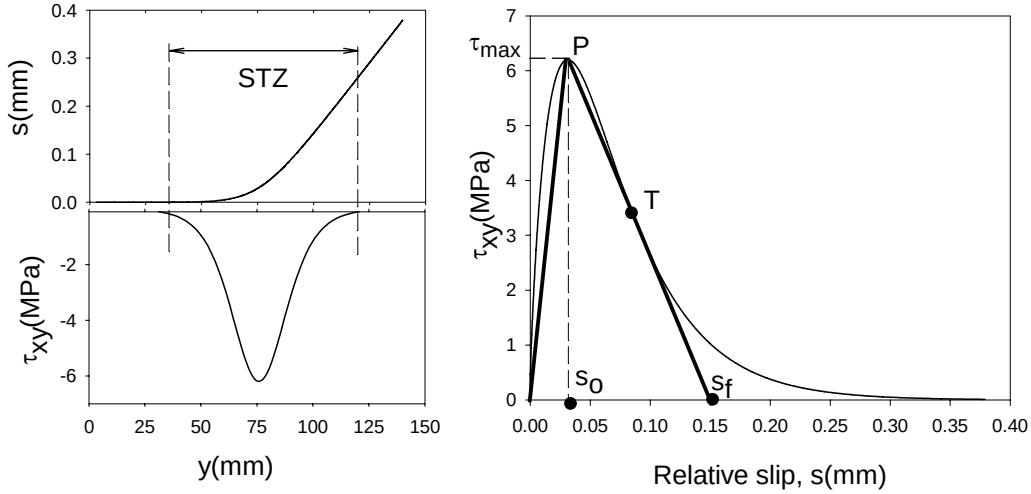

Figure 4.6: Relative slip, interfacial shear stress and material law;(a) Interfacial shear stress and relative slip along the FRP corresponding to point C of the load response; and (b) Material law of the FRP-concrete interface corresponding to point C

4.6.2 Determination of fracture parameters

The material law of the FRP-concrete interface during shear debonding is the relationship between the shear stress/traction and the relative displacement/slip between the two adherents. The relative slip, s, is defined as the difference in the displacements between the concrete and FRP at a given section. The procedure for obtaining the interfacial material law has previously been developed by the authors (Ali-Ahmad et al. 2004 and 2005). In this procedure, the relationship between the interfacial shear stress and the relative slip (τ versus s relationship) across the interface is obtained from the

measured axial strain in the FRP at a given point on the post peak load response. The relative slip, s, is obtained by integrating the axial strain along the length of the FRP. The interfacial shear stress at any location along the length of the FRP is proportional to the gradient of the axial strain in the FRP and is given by the following expression:

$$\tau(y) = t_f E_{FRP} \frac{d\varepsilon(y)}{dy} \tag{4.2}$$

where t_f is the thickness of the fibers contained in the FRP composite and E_{FRP} is the elastic modulus of the FRP composite. The variation in the relative slip and the interfacial shear stress along the length of the FRP for point C in the post peak load response of the control specimen are shown in Figure 4.6. It can be seen that the relative slip between the FRP and concrete increases continuously within the STZ and beyond. Within the STZ, the interfacial shear stress increases up to a peak value and then decreases to a value equal to zero upon approaching the fully debonded region. The interface material law is obtained by combining the relative slip and the shear stress along the length of the FRP and is also shown in Figure 4.6. It can be observed that the interface material law of the FRP-concrete interface exhibits post peak softening behavior. Using this procedure, the interface material law was determined for all specimens for global slip varying between 0.35 and 0.7mm. The material law obtained from one specimen was found to be nominally identical. The material law obtained from specimens with different levels of freeze-thaw exposure was similar in shape as that obtained from the control specimen.

The interfacial fracture energy, G_F, defines the energy required to produce a unit crack area and obtained from the area under the entire "τ-s" response (Ali-Ahmad et al. 2005). The compiled results of G_F, which were obtained from all specimens, are shown

in Table 4.1. It can be seen that while there is a large scatter in the values of G_F for any number of freeze-thaw cycles, the general trend shows a decrease in the magnitude of G_F with an increase in the number of cycles. This indicates that freeze-thaw cycling introduces additional damage in the interface, which results in a decrease in the interfacial fracture energy.

A simplified bilinear representation of the interfacial material law is shown in the bolded lines of Figure 4.6. The material behavior is idealized using a linear relationship up to the peak shear stress, τ_{max}, after which a linear softening is assumed. The linear representation for the softening part of the material law was determined by plotting a straight line that passes through the peak stress and the inflection point of the post-peak softening response (line PT of Figure 4.6). The parameters that define the interfacial material law are the maximum shear stress, τ_{max}, the corresponding relative slip, s_o, and the relative slip at the intercept, s_f. s_f is defined as the horizontal intercept of the linear softening curve. The fracture parameters for each specimen were determined at different values of global slip that corresponds with different crack locations along the length of the FRP. Ten sets of fracture parameters were obtained from each specimen. The values of these parameters obtained from all specimens are compiled and summarized in Table 4.1 and also plotted graphically in Figure 4.7. The values of the facture parameters, obtained from specimens subjected to a given number of freeze-thaw cycles, have been normalized with respect to the corresponding mean values obtained from the control specimens to reduce the effect of variability from the concrete batches. From Figure 4.7, it is clearly seen that there is a decrease in the fracture parameters with increasing number of freeze-thaw cycles. However due to the large scatter in the data obtained from

a given specimen, it is hard to relate the observed changes in different specimens. For this reason, an analysis was performed to determine whether the observed decrease in the different parameters is statistically significant.

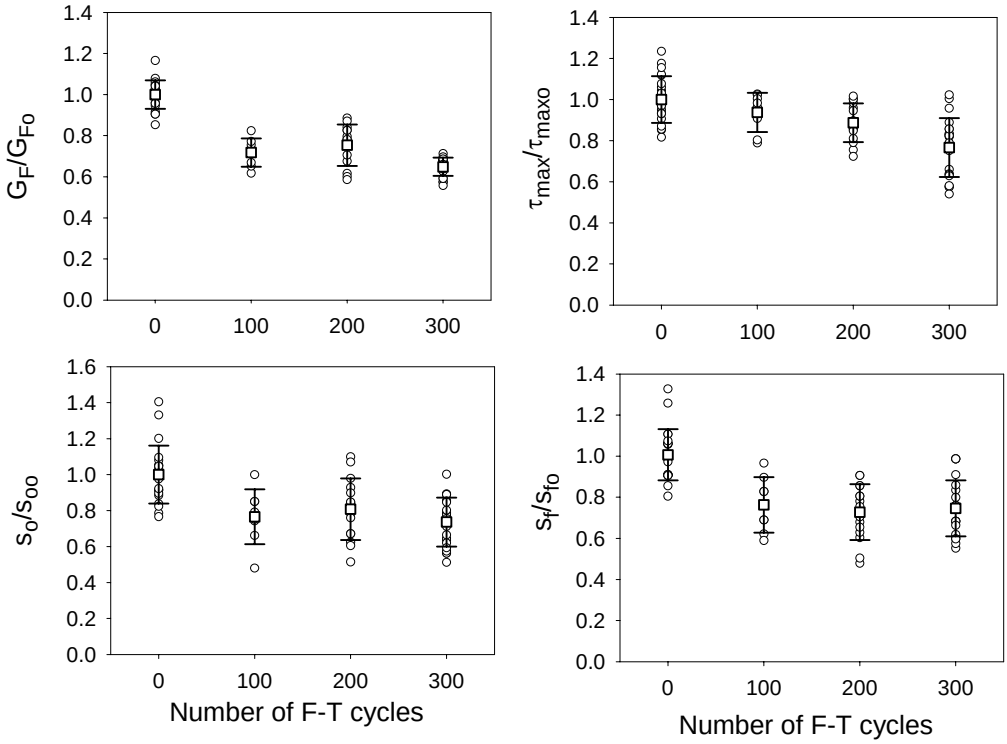

Figure 4.7: Scatter plots of normalized fracture parameters as function of freeze-thaw cycles

4.7 Statistical analysis

The number of specimens tested for a given number of freeze-thaw cycles and the corresponding number of readings obtained from each specimen are given in Table 4.2. The compiled data of the fracture parameters is presented in Table 4.1. Large scatter in the parameters was observed for readings taken within the same specimen and for readings taken from different specimens prepared using the same concrete mix and FRP materials and subjected to the same number of freeze-thaw cycles. In fact, the scatter led to coefficients of variations (C.O.V=standard deviation/mean) exceeding 25% for some

of the calculated fracture parameters defined above. This large C.O.V has meant that in several cases, the values of some parameters calculated for freeze-thawed specimens showed an increase in the fracture parameters rather than the expected decrease. Such observations have also been noted by other researchers (Green et al. 2002). These data anomalies not withstanding, an overall trend of decreasing parameters was observed.

Table 4.2: Number of specimens and readings in each freeze-thaw category

Number of freeze-thaw cycles	Number of specimens	Number of readings
0	4	40
100	2	20
200	2	20
300	4	40

The variability in the measured data can be attributed to three factors: (a) variability between concrete mix from different batches; (b) variability between direct shear specimens prepared from the same concrete batch; and (c) variability in the shear stress and strain values obtained at different locations and during different loading stages of the same sample. This variability is due to the local effects of the concrete, FRP and adhesive properties. In this chapter, emphasis is placed on studying how freeze-thaw cycling affects the average properties of the direct shear specimens given the large variability on the local properties of the adherents. To reduce the effect of the variability from the concrete mix batches, all the measured variables are normalized with respect to a control specimen taken from the same batch that was not subjected to freeze-thaw cycles.

The variables included in the statistical analysis are τ_{max}, s_o, s_f, G_F and L_{STZ}. To determine the probability distributions that best represent these variables, the data points were plotted on normal probability papers. The plots showed that all parameters could be adequately modeled using normal probability distributions. For instance, Figure 4.8

plots the fracture parameter, s_o, on normal probability paper showing a reasonably tight fit along a straight line.

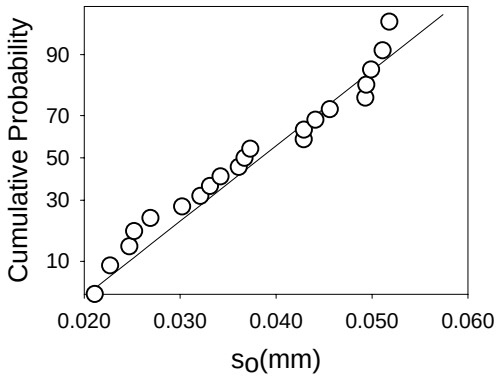

Figure 4.8: Relative slip s_o plotted on normal probability paper

Table 4.3: Compiled results of the significance testing on the mean at the 95% confidence level

95% confidence level					
Interval of F-T cycles	G_F	τ_{max}	s_o	s_f	L_{STZ}
0-100	c=0.0235 $\mu_X-\mu_Y$=0.24>c H_1 passed	c=0.343 $\mu_X-\mu_Y$=0.22<c H_o passed	c=0.0032 $\mu_X-\mu_Y$=0.0120>c H_1 passed	c=0.0107 $\mu_X-\mu_Y$= 0.07>c H_1 passed	c=2.62 $\mu_X-\mu_Y$=10>c H_1 passed
100-200	c= 0.0279 $\mu_X-\mu_Y$=0.09>c H_1 passed	c=0.332 $\mu_X-\mu_Y$=0.59>c H_1 passed	c= 0.0032 $\mu_X-\mu_Y$=0.009>c H_1 passed	c= 0.0132 $\mu_X-\mu_Y$=0.03>c H_1 passed	c=2.67 $\mu_X-\mu_Y$=4>c H_1 passed
0-200	c= 0.033 $\mu_X-\mu_Y$=0.15>c H_1 passed	c=0.353 $\mu_X-\mu_Y$=0.81>c H_1 passed	c= 0.0036 $\mu_X-\mu_Y$=0.004>c H_1 passed	c= 0.0135 $\mu_X-\mu_Y$=0.04>c H_1 passed	c=2.22 $\mu_X-\mu_Y$=14>c H_1 passed
200-300	c= 0.0314 $\mu_X-\mu_Y$=0.08>c H_1 passed	c=0.307 $\mu_X-\mu_Y$=0.31>c H_1 passed	c= 0.0028 $\mu_X-\mu_Y$=0.011>c H_1 passed	c= 0.0122 $\mu_X-\mu_Y$=0.02>c H_1 passed	c=2.12 $\mu_X-\mu_Y$=10>c H_1 passed
0-300	c= 0.028 $\mu_X-\mu_Y$=0.23>c H_1 passed	c=0.319 $\mu_X-\mu_Y$=1.12>c H_1 passed	c= 0.0028 $\mu_X-\mu_Y$=0.014>c H_1 passed	c= 0.009 $\mu_X-\mu_Y$=0.06>c H_1 passed	c= 2.06 $\mu_X-\mu_Y$=24>c H_1 passed

(1) H_1 passed: there is significant difference at the 95% confidence level;
(2) H_o passed: two sets of data belong to the same population at the 95% confidence level.

This section performs a hypothesis testing procedure to verify that the decreasing trend on material properties that is observed in the normalized average values of the fracture parameters due to freeze-thaw cycling is statistically significant (Benjamin & Cornell 1970). An example is provided herein to illustrate how the statistical test is performed for two sets of data collected for τ_{max} from specimens subjected to 0 and 100

freeze-thaw cycles. The data collected for specimens with 0 freeze-thaw cycles are assembled under set X while set Y represents the data after 100 freeze-thaw cycles:

$$X: \tau^{0}_{max,1}, \tau^{0}_{max,2}, \ldots\ldots\ldots\ldots \tau^{0}_{max,n} \tag{4.3}$$

$$Y: \tau^{100}_{max,1}, \tau^{100}_{max,2}, \ldots\ldots\ldots\ldots \tau^{100}_{max,m} \tag{4.4}$$

where n and m are the number of readings given in Table 4.2 for 0 and 100 freeze-thaw categories, respectively. During the test, the null hypothesis H_o is stated as: the difference between two sets of samples is not significant indicating that the sets may belong to the same population or in this case, freeze-thaw cycling does not produce a significant change in the fracture parameters. The alternate hypothesis H_1 can be stated as: there is a significant difference between the means of the two sets of data to indicate that the two sets do not belong to the same population or in our case; freeze-thaw cycling produces a significant change in the fracture properties of the interface. The results of the hypothesis testing revealed that there is a statistically significant drop in the mean values of the parameters τ_{max}, s_o, s_f, G_F and L_{STZ} obtained after subjecting the specimens to freeze-thaw cycling when compared with the mean values of the corresponding control parameters. All testing is based on the 95% confidence level. The testing hypothesis is based on accepting the null hypothesis H_o when the difference in the sample means is less than the acceptance interval "c" given by Equation 4.5:

$$c = 1.64\sqrt{\frac{\sigma_X^2}{n} + \frac{\sigma_Y^2}{m}} \tag{4.5}$$

where σ_X and σ_Y are the standard deviations of sample sets X and Y, respectively. If the difference in the means of the two samples is less than "c" then the two samples belong to the same population and the null hypothesis H_o is accepted. Otherwise, the alternate

hypothesis H_1, i.e. there is a significant difference at the 95% confidence level, is accepted. Table 4.3 summarizes the compiled results of the significance testing. The results summarized in Table 4.3 indicate that all the parameters passed the significance testing at the 95% confidence level. The only parameter that did not pass the significance testing is τ_{max} obtained from specimens subjected to 100 freeze-thaw cycles when compared to the control specimens.

Based on the results of the significance analysis, it appears that there is a significant drop in G_F, s_o, s_f and L_{STZ} with increasing number of freeze-thaw cycles. Interestingly, τ_{max} does not show a significant decrease in the first 100 freeze-thaw cycles. Therefore the decrease in G_F in the first 100 freeze-thaw cycles can be attributed to a decrease in s_o and s_f. Subsequently, the decrease in the interface fracture energy is attributed to a decrease in all three parameters. The results of this analysis suggest that there is a progressive decrease in the fracture parameters with freeze-thaw cycling. Thus, every freeze-thaw cycle introduces additional damage in the interface, which results in a decrease in the fracture parameters and hence the load transferring ability of the interface. The statistical scatter inherent in such testing however precludes developing predictive degradation models using the limited data available. While it has been shown that the change in the variables is significant, the current data does not provide a good estimation of the rate of change in these parameters for a given number of freeze-thaw cycles. Further testing should be performed to verify these results and to generate data for developing predictive models, which account for the different sources of statistical variations.

4.8 Conclusions

In this chapter, the influence of freeze-thaw cycling on the interfacial debonding and the stress transfer between the concrete and the FRP is investigated. A statistical analysis is performed to evaluate the significance of the decrease in the fracture parameters. Based on the results presented in this chapter, the following conclusions can be drawn:

1) A slight decrease in the initial stiffness and an extended non-linear zone prior to the peak load is observed in direct-shear response of the specimens subjected to freeze-thaw when compared with the control specimens.

2) There is no decrease in the elastic modulus of the FRP composite with freeze-thaw cycling.

3) There is a progressive decrease in the load carrying capacity in the specimens subjected to freeze-thaw cycles when compared with the control specimens. In freeze-thawed specimens, the progressive debonding in the post peak load response occurs at a lower load than that of the control.

4) In the post-peak part of the load response, there is a constant stress transfer length between the concrete and the FRP sheets for all specimens. The strain distribution in the stress transfer zone of the freeze-thaw damaged specimen has the same shape as that observed in the control specimen. However, there is a statistically significant decrease in the length of the stress transfer zone and the strain in the FRP at full debonding with an increase in the number of freeze-thaw cycles.

5) The nonlinear material law of the FRP-concrete interface for specimens subjected to freeze-thaw cycling is found to be similar in shape when compared with that obtained

from the control specimens. However, there is a statistically significant decrease in the parameters describing the material law as the number of freeze-thaw cycles is increased.

6) Although the failure in all specimens tested is found to be due to debonding of FRP from the concrete substrate along the interface, there is a slight, yet noticeable change in the failure mode due to freeze-thaw cycling. The failure occurs close to the FRP sheet for the freeze-thawed specimens.

7) The results of the statistical analysis indicate that there is a significant drop in the interfacial fracture energy with freeze-thaw cycling. The results suggest a progressive change with freeze-thaw cycling indicating continuous accrual of freeze-thaw damage in the interface.

CHAPTER 5

ANALYSIS OF INSTABILITY IN FRP-CONCRETE SHEAR DEBONDING FOR BEAM STRENGTHENING APPLICATIONS

5.1 Overview

The debonding mode of failure, which is observed in concrete beams strengthened using externally attached FRP sheets, is analyzed in this chapter. A numerical analysis of the direct-shear response of FRP attached to a concrete substrate is performed to study the initiation, formation and propagation of an interfacial crack between the two adherents. The material response of the bi-material interface, which includes post-peak softening, is considered in the numerical model. An instability in the load response associated with snap-back is predicted close to failure and the arc-length method is used to obtain the entire load response. The effect of the bonded length on the stress transfer between the FRP and concrete and on the ultimate failure is also analyzed. It is shown that there is a scaling in the load capacity when the bonded length does not allow for the establishment of the full stress-transfer zone associated with interface crack growth. The load response is shown to change from softening to snap-back upon

increasing the bonded length of the FRP. From the results of the numerical analysis, a fundamental understanding of interfacial crack propagation and the failure instability of concrete members strengthened with externally bonded FRP is developed. A simple energy based formulation demonstrates that the instability at complete debonding would lead to an explosive failure associated with a sudden release of energy.

5.2 Introduction

Carbon fiber reinforced polymer (CFRP) sheets are being used as external reinforcement for strengthening existing concrete bridge members. In typical flexural strengthening applications, test results (Ritchie et al. 1991, Buyukozturk and Hearing 1998, Lopez et al. 2000, Wu et al. 1997, Saadatmanesh and Ehsani 1991, Meier et al. 1992) have shown that besides the typical failure modes observed in reinforced concrete beams, premature debonding of the FRP from the concrete substrate is an important factor that controls the efficacy of the repair. In beams with bonded plates, where the FRP plate has a large thickness and hence significant flexural rigidity, the final failure is usually caused by the delamination from the end of the bonded plate (Saadatmanesh and Ehsani 1991, Leung 2001). Delamination of the FRP plate has been shown to be caused by the high shear and normal stresses generated at the free end of the plate (Taljsten 1997a, Malek et al. 1998). In another mode of failure, debonding is initiated at the bottom of existing flexure or shear-flexure cracks (Wu et al.1997, Leung 2004). This debonding mode occurs when CFRP sheets or plates with low flexural rigidity are used in beams with span/depth ratios greater than 10 (beams that exhibit flexural failure mode) and where the sheets are continued close to the support (Leung 2004). Similarly, in shear strengthening application, debonding of FRP from concrete has been shown to

be the major cause of failure (Triantafillou 1998, Khalifa et al. 1998). The interfacial shear stress is the primary stress component responsible for the initiation of a crack whose progressive propagation ultimately leads to debonding. As debonding progresses to a complete separation of the FRP from the concrete surface, the ultimate failure is observed to be very sudden and uncontrollable in both flexure (Triantafillou and Pelvris 1992, Spadea et al 1998) and shear strengthening applications (Norris et al. 1997, Khalifa et al. 1998).

Developing rational design guidelines for the application of FRP strengthening techniques to concrete beams requires a fundamental understanding of the shear debonding phenomenon and the associated failure mechanism. Several finite element analyses have been performed to study the shear stress transfer across the FRP-concrete interface and several analytical formulations based on the classical sectional analysis have been proposed for predicting the ultimate load of a strengthened beam (Malek et al. 1998, Arduini and Nanni 1997, Arduini et al. 1997). These previous analyses however did not explicitly consider the material law of the interfacial bond between concrete and the FRP. Recently, researchers have developed various constitutive laws that adequately model the FRP-concrete bond behavior during debonding (Ali-Ahmad et al. 2005, Leung 2004, De Lorenzis et al. 2001, Savoia et al. 2003). Fracture-based analytical and numerical formulations have also been proposed to predict the initiation of shear debonding of FRP from concrete surface (Taljsten 1996, Yuan et al. 2001, Wu and Niu 2000). A limited number of numerical simulations of strengthened reinforced concrete beams, which account for shear debonding, have also been reported in the literature (Leung et al. 2000, Leung and Tung 2001, Wu and Niu 2000). However, the full

understanding of the uncontrolled failure in the strengthened beams, which fail by shear debonding, is still under investigation.

This chapter presents a numerical analysis of the FRP-concrete shear debonding mechanism using the nonlinear material model for the interface previously established in Chapter 3. The analysis is carried out using the finite element method. The numerical investigation is performed on the direct-shear test geometry. The direct-shear test geometry was chosen because it provides a realistic representation of the shear debonding in a beam and allows for a fundamental evaluation of the debonding mechanism free from other geometric effects. An insight into the unstable failure witnessed in shear debonding in beams can also be obtained from this test geometry. From the results of the numerical analysis, a close agreement between the numerical and experimental stress distribution at the FRP-concrete interface is obtained. The numerical analysis was also able to capture the instability in the load response that results in the sudden failure observed in the experimental response. The equilibrium path of the load response after the point of instability in the debonding response of FRP is traced using the arc-length method and the reason for the instability is shown to be the snap-back mechanism. The influence of the bonded length on the observed instability in the test response is also investigated. Finally, the implications of the shear debonding response obtained in the laboratory on the beam strengthening applications are discussed.

5.3 Background

Both flexure and shear strengthening applications using externally attached FRP rely on shear stress transfer across the FRP-concrete interface. It has been shown that when FRP bridges a pre-existing flexure or shear-flexure crack in concrete, very high

interfacial shear stresses are generated close to the edge of the crack (Leung 2004). This stress concentration results in the initiation of an interfacial crack between FRP and concrete. The opening of the pre-existing crack faces in concrete results in the propagation of the interfacial crack, leading to the debonding of a portion of the FRP from the substrate. This shear debonding response of the FRP has previously been studied using direct-shear tests, which allowed for studying the debonding phenomenon and also to extract meaningful material parameters for shear response of the interfacial bond (Ueda et al. 1999, Taljsten 1997b, Ali-Ahmad et al. 2005).

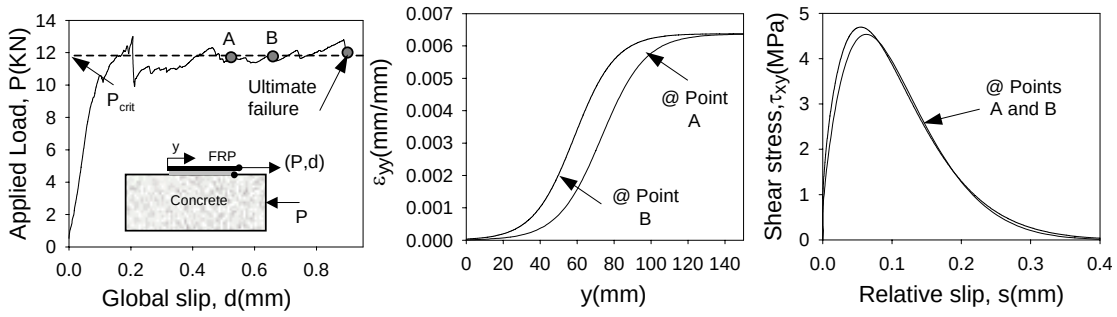

(a) **(b)** **(c)**

Figure 5.1: Experimental results (Ali-Ahmad et al. 2005) ; (a) Typical load versus global slip response of FRP bonded to concrete; (b) Strain distribution along the FRP sheet corresponding to points A and B; and (c) Material law of FRP/concrete interface

An experimental investigation of the debonding failure between the concrete and the FRP in a direct-shear test was conducted in chapter 3 using a high-resolution, full-field optical technique. The direct shear test consisted of the classical pull-push configuration, where an axial force is applied to the FRP sheet bonded to a concrete block which is restrained from movement (shown in the inset of Figure 5.1a). A state of pure shear is introduced in the interface throughout the loading process. The material properties of the FRP-concrete interface were experimentally derived at different points of the load response of the direct-shear specimen from the measured surface strains in

the FRP and the concrete provided by the optical technique. The debonding was produced by an interfacial crack and the load response of the specimen was governed by the crack growth.

A typical load response associated with debonding of the FRP sheet from the concrete substrate is shown in Figure 5.1a. The displacement measured at the point of application of the load at the edge of the bonded area is referred to as global slip, d. It was noticed that as the global slip increases, the load response is initially approximately linear, becomes nonlinear when the debonding is initiated and then levels off and remains approximately constant at P_{crit} with increasing global slip up to failure. The observed crack initiates in the nonlinear part of the load response before the load approaches P_{crit}. Once the crack initiates in the interface, it initially grows in a stable manner with increasing load up to P_{crit}. As the crack reaches a critical length, it propagates in a self-similar manner at a constant applied load. This steady crack growth is responsible for the increase in the global slip of the FRP relative to concrete at the constant load, P_{crit}. When the load levels off at P_{crit}, there is a constant stress transfer length between the concrete and the FRP sheets associated with the crack, which was found to be approximately equal to 85mm. The stress transfer zone advances with the bonded length of the FRP as the crack propagates as shown in Figure 5.1b. The nonlinear interfacial material law that exhibits softening behavior was then established as shown in Figure 5.1c. The final failure of the specimen was produced by the complete separation of the FRP composite sheet from the concrete substrate. It was observed that the ultimate failure in the debonding response of the direct shear specimen occurs at a high load and is sudden and uncontrollable.

Another critical finding of the direct-shear test pertained to the axial strain in the concrete during the test. From the axial strains measured on the front surface, it was found that the axial displacements measured on the concrete surface were insignificant when compared with those of the FRP composite. Further, the strains measured on the sides of the concrete specimen, by placing the FRP sheet close to the edge of the concrete also showed that the strains in the concrete were confined to a small region close to the surface.

From tests using shorter bonded lengths, it has been shown that the load does not level off during debonding or exhibit unstable failure (Taljsten 1997b). Further, a non-proportional scaling in the ultimate stress with bonded length has been reported; the maximum stress in the FRP to achieve a complete debonding has been experimentally shown to increase with an increase in the bonded length (Wu et al. 2004). An understanding of this scaling effect and its relation with the instability at ultimate failure is therefore essential to develop rational design procedures.

The ultimate failure in shear debonding which is sudden and catastrophic is undesirable. Therefore, any design guidelines that are established for the application of FRP repairs of concrete structures that rely on the transfer of the shear stresses across the interface must be developed taking into consideration the possibility of the failure by complete debonding. An understanding of the unstable shear debonding failure and the influence of the bonded length on the observed mode of failure is required.

5.4 Objectives

The objectives of this chapter are to develop a numerical model for studying the shear debonding at the concrete-FRP interface. The specific objectives are: (a) to trace

the equilibrium path of the entire load response during debonding of FRP from concrete; (b) to understand the ultimate failure and the cause of instability in the load response; (c) to study the scaling effect of the bonded length on the stress transfer between concrete and FRP; and (d) to understand the implication of the instability in the debonding on the failure mechanism of strengthened beams.

5.5 Numerical analysis methodology

The numerical analysis presented in this chapter is based on the finite element method. The specimen used in direct shear tests presented in chapter 3 is modeled and a comparison between the experimental and numerical load responses is performed.

5.5.1 FE discretization of the test geometry

The finite element model uses one-dimensional axial elements to represent the behavior of the FRP composite sheet. The bond at the FRP-concrete interface is modeled using spring elements with a simplified bilinear response, which was obtained from the experimentally determined material law for the interface (Figure 5.2c). In the bilinear representation, a linear ascending shear stress versus local slip is obtained up to the peak shear stress, τ_{max}, following which a linear softening corresponding with the initial tangent of the actual softening response is assumed. The average values of the parameters of the bilinear response were obtained experimentally and identified as: τ_{max}= 5.03MPa, s_o= 0.048mm and s_f = 0.23mm (Ali-Ahmad et al. 2005). In the numerical representation, the concrete substrate is assumed to be rigid, based on the observed experimental results, which show that the strain in the concrete is negligible compared to that in the CFRP composite sheets. The finite element model of the test geometry is

shown in Figure 5.2b. The engineering properties of the composite sheets are based on the nominal width and thickness of the fibers contained in the composite sheet and not the gross composite area. The gross composite area is typically not used owing to the difficulties associated with controlling the total composite thickness in the field during a wet lay-up installation process (Replark System 2000). The material response of the CFRP was considered to be linear elastic up to rupture.

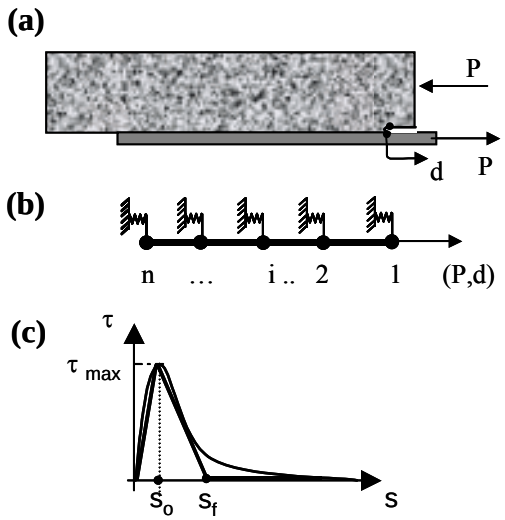

Figure 5.2: Finite element discretization; (a) Direct shear test geometry of FRP composite sheet bonded to concrete substrate; (b) finite element model; and (c) material law of FRP/concrete interface

Numerical analyses were performed for different bonded lengths of the CFRP varying between 25mm and 150mm. The width of the CFRP composite sheet, b, was kept constant equal to 46 mm for all cases. The FRP bonded length was discretized into one-dimensional elements, each of length L_{el} equal to 1mm.

5.5.2 Obtaining the Equilibrium path

The observed uncontrolled failure at a high load in the experimental response of the direct shear tests suggests that the load response becomes unstable at that point. An

ideal analysis method for the nonlinear behavior of structures should be able to trace the equilibrium path of the entire load-displacement response observed experimentally including the representation of possible snapback or snapthrough mechanisms. Traditional non-linear incremental load-control solution procedures based on the Newton-Raphson method was found to be unsuitable for tracing the response, where the load levels-off at a constant value or when the response of the structure exhibits softening. For these reasons, the use of a displacement control method has been proposed to overcome the problems associated with the load-control method (Argyris 1965, Pian and Tong 1970, and Zienkiewicz 1971). However, use of the displacement control method was observed to diverge close to the point of ultimate failure. It was noticed that just prior to the onset divergence in the numerical response, a significant portion of the FRP was still bonded to the concrete. Displacement control methods have been shown to fail when dealing with structures that exhibit snapback behavior (Riks 1972; Bazant and Cedolin 1991, Wempner 1971). In such situations, continuation methods, which add a constraint equation to the original non-linear equation of equilibrium of the problem have been shown to be successful in tracing the solution along any given equilibrium path. An ideal technique for tracing the equilibrium path of the entire load response is known as the arc-length method (Wempner 1971, Riks 1972, 1979, Crisfield 1983, Forde and Steimer 1987). The arc-length method combines the benefits of load and displacement control methods in a sense by varying both the incremental load and displacement at every load step.

The arc-length method was used to trace the path by adding an additional constraint equation and solving the extended set of equations using the Newton-Raphson

method. A brief description of the arc-length method is provided next. The governing equilibrium equation for a nonlinear static structural system requires that the internal forces balance the externally applied forces. This can be expressed in the following form:

$$\underset{\sim}{r}(\underset{\sim}{d},\lambda) = \underset{\sim}{f}_{\text{int}}(\underset{\sim}{d}) - \lambda \underset{\sim}{f}_{ext} = 0 \tag{5.1}$$

where $\underset{\sim}{f}_{\text{int}}(\underset{\sim}{d})$ is a vector represents the internal nodal forces, $\underset{\sim}{f}_{ext}$ is a pre-set basic load distributor of the external load, $\underset{\sim}{d}$ is the displacement vector, λ is a load incrementing factor, and $\underset{\sim}{r}(\underset{\sim}{d},\lambda)$ is the out of balance force vector also known as the residual force vector. In Equation 5.1, the parameter λ is a variable that controls the load. Therefore, the resulting equation has two sets of unknowns, $\underset{\sim}{d}$ and λ, which are determined using an additional constraint equation. The additional equation is established to restrict the search around a circle of radius Δs.

$$\alpha^2 \Delta\lambda^2 \underset{\sim}{f}_{ext}^T \underset{\sim}{f}_{ext} + \Delta\underset{\sim}{d}^T \Delta\underset{\sim}{d} - \Delta s^2 = 0 \tag{5.2}$$

where $\Delta\underset{\sim}{d}$ is the incremental nodal displacement vector, $\Delta\lambda$ is the incremental load parameter, α is a scaling factor to adjust the terms of Equation 5.2 to have the same basic units, Δs is a fixed radius of the desired intersection of the arc represented by Equation 5.2 with the equilibrium path represented by Equation 5.1 as illustrated in Figure 5.3. The scaling factor, α, used to achieve the unit adjustment was obtained from the diagonal of the tangential stiffness matrix, K_T, as shown below

$$\alpha^{-1} = \frac{\sum_{m=1}^{n} K_T(m,m)}{n} \tag{5.3}$$

where n is the total number of degrees of freedom.

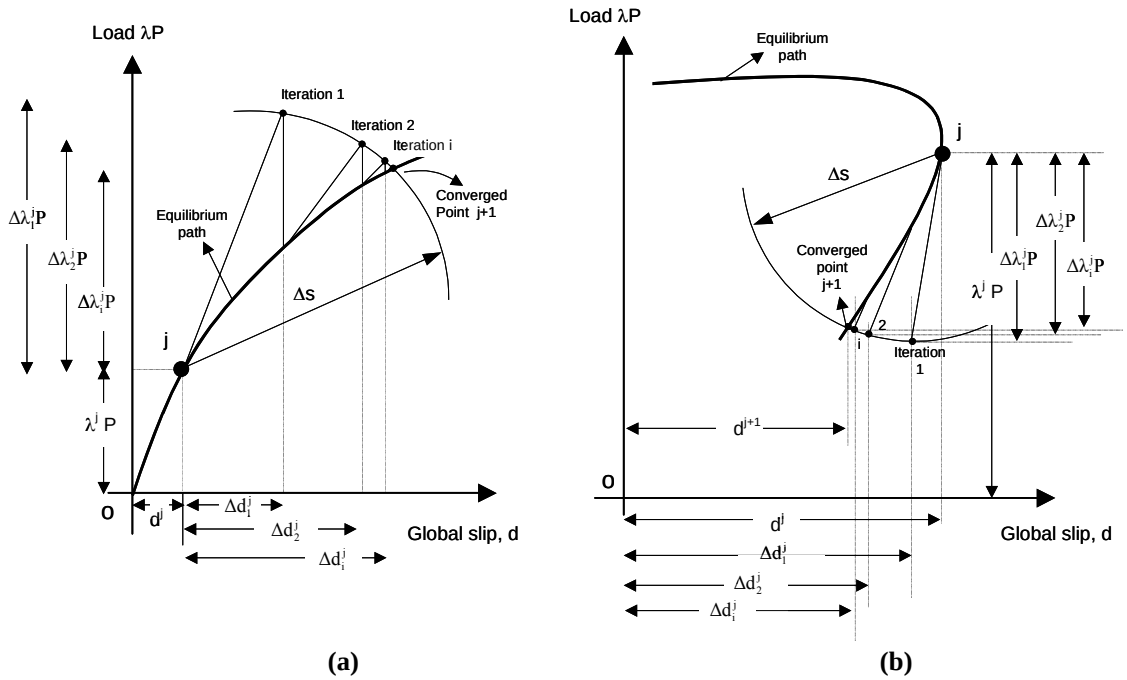

Figure 5.3: A schematic representation of the arc length procedure; (a) increasing portion of the response; and (b) snapback response

In each step, starting from a known solution $(\underset{\sim}{d}^{j}, \lambda^{j}\underset{\sim}{f}_{ext})$, the subsequent solutions are calculated for a given Δs, using an iterative procedure to obtain the converged equilibrium solutions $(\underset{\sim}{d}^{j+1}, \lambda^{j+1}\underset{\sim}{f}_{ext})$. With some simplifications, Equations 5.1 and 5.2 can be combined and re-written in matrix form as functions of the incremental changes of the displacement vector and load parameter within each load step.

$$\begin{Bmatrix} \delta\underset{\sim}{d} \\ \delta\lambda \end{Bmatrix} = \begin{bmatrix} \underset{\sim}{K}_T & -\underset{\sim}{f}_{ext} \\ 2\Delta\underset{\sim}{d}^T & 2\alpha\Delta\lambda\,\underset{\sim}{f}_{ext}{}^T\,\underset{\sim}{f}_{ext} \end{bmatrix}^{-1} \begin{Bmatrix} \underset{\sim}{r}_i \\ -p_i \end{Bmatrix} \tag{5.4}$$

where $\delta\underset{\sim}{d}$ is the iterative change in nodal displacement, $\delta\lambda$ is the iterative change in load parameter, $\underset{\sim}{K}_T$ is the tangential stiffness matrix, $\underset{\sim}{r}_i$ and p_i are the values of the residual force vector and the arc length and are given as

$$\underset{\sim}{r}_i = \lambda_i \underset{\sim}{f}_{ext} - \underset{\sim}{f}_{\text{int}}(\underset{\sim}{d}_i, \lambda_i) \tag{5.5}$$

5.5.3 Analysis procedure and Implementation

The analysis was started using the classical load-control procedure with Newton-Raphson method up to an initial point within the linear elastic range. The arc length method was then applied for all subsequent points along the loading curve. The step size for the incremental analysis, Δs, used in the analysis was kept fixed at 0.001. The step size was chosen after a trial and error procedure in such a way that smaller step size did not result in an improvement in the load response. Within each step j, the previous converged solution, $(\underset{\sim}{d}^{j}, \lambda^{j} \underset{\sim}{f}_{ext})$, was used to obtain a starting value of $(\underset{\sim}{d}^{j} + \Delta\underset{\sim}{d}_{i}^{j}, \lambda^{j} \underset{\sim}{f}_{ext} + \Delta\lambda_{i}^{j} \underset{\sim}{f}_{ext})$ at the first iteration (i=1). The stiffness matrix was updated after each iteration to account for the softening in interfacial spring elements, which are loaded past s_o. The convergence criterion for each iteration "i" of a given load step "j" was based on the normalized form of the residual force vector. The procedure used to predict the continuation direction so that the solution does not track back the current path was based on the sign of the current tangent stiffness determinant as suggested by Feng et al. (1995):

$$sign(\Delta\lambda_1^j) = sign\left|K_T\right| \tag{5.6}$$

Figure 5.4 shows a flowchart that summarizes the algorithm for an explicit iteration using arc length procedure. The analysis procedure for explicit iteration consisted of the following steps:

1- Starts from an initial point $(\underset{\sim}{d}^{j}, \lambda^{j} \underset{\sim}{f}_{ext})$ within the linear elastic range obtained from the load control procedure with Newton-Raphson method.

First iteration of load step j

2- The residual forces in the first iteration (i=1) are zero. The incremental displacement vectors and the incremental load parameter are calculated using:

$$\Delta \underset{\sim}{d}_I^j = \underset{\sim}{K}_T^{-1} \underset{\sim}{f}_{ext} \tag{5.7}$$

$$\Delta\lambda = \Delta\lambda_i^j = p \times \sqrt{\frac{\Delta s^2}{\alpha^2 + \left|(\Delta \underset{\sim}{d}_I^j)^T . \Delta d_I^j\right|}} \tag{5.8}$$

$$\Delta \underset{\sim}{d} = \Delta \underset{\sim}{d}_i^j = \Delta\lambda_i^j \times \Delta \underset{\sim}{d}_I^j \tag{5.9}$$

$$\underset{\sim}{d}_i^j = \underset{\sim}{d}^j + \Delta \underset{\sim}{d}_1^j \tag{5.10}$$

$$\lambda_i^j = \lambda^j + \Delta\lambda_i^j \tag{5.11}$$

where $p = +1$ if $|K_T| > 0$ and $p = -1$ if $|K_T| < 0$

Iterations within the load step j

3- For iteration i, $\delta \underset{\sim}{d}$ and $\delta\lambda$ are determined as follows:

$$\underset{\sim}{r}_i = \lambda_i^j \underset{\sim}{f}_{ext} - \underset{\sim}{f}_{\text{int}}(\underset{\sim}{d}_i^j, \lambda_i^j) \tag{5.12}$$

$$p_i = \alpha^2 \Delta\lambda^2 \underset{\sim}{f}_{ext}^T \underset{\sim}{f}_{ext} + \Delta \underset{\sim}{d}^T \Delta \underset{\sim}{d} - \Delta s^2 \tag{5.13}$$

$$\begin{Bmatrix} \delta \underset{\sim}{d} \\ \delta\lambda \end{Bmatrix} = \begin{bmatrix} \underset{\sim}{K}_T & -\underset{\sim}{f}_{ext} \\ 2\Delta \underset{\sim}{d}^T & 2\alpha\Delta\lambda \underset{\sim}{f}_{ext}^T \underset{\sim}{f}_{ext} \end{bmatrix}^{-1} \begin{Bmatrix} \underset{\sim}{r}_i \\ -p_i \end{Bmatrix} \tag{5.14}$$

4- Update the displacement vector and the external force vector:

$$\underset{\sim}{d} = \underset{\sim}{d}_i^j = \underset{\sim}{d}_{i-1}^j + \delta \underset{\sim}{d} \tag{5.15}$$

$$\Delta \underset{\sim}{d} = \Delta \underset{\sim}{d}_i^j = \Delta \underset{\sim}{d}_{i-1}^j + \delta \underset{\sim}{d} \tag{5.16}$$

$$\Delta\lambda = \Delta\lambda_i^j = \Delta\lambda_{i-1}^j + \delta\lambda \tag{5.17}$$

$$\lambda = \lambda_i^j = \lambda_{i-1}^j + \delta\lambda \tag{5.18}$$

5- Calculate the new residual vector $\underset{\sim}{r}_i$ of Equation 5.12 and check whether the convergence criterion $\sqrt{\sum_{m=1}^{n} \underset{\sim}{r}_i^2(m)} \le \varepsilon_0$ is satisfied where ε_0 is a prescribed value

equal $\frac{1}{1000}\times\lambda^j \underset{\sim}{f}_{ext}(n)$. If the convergence criterion is not met, repeat steps 3, 4 and 5 until convergence.

6- When the solution converges $(\underset{\sim}{d}^{conv.}, \lambda^{conv.}\underset{\sim}{f}_{ext})$, repeat steps 2 through 5 with the latest values of $\underset{\sim}{d}^{conv.}$ and $\lambda^{conv.}$ as starting points for the new step j=j+1.

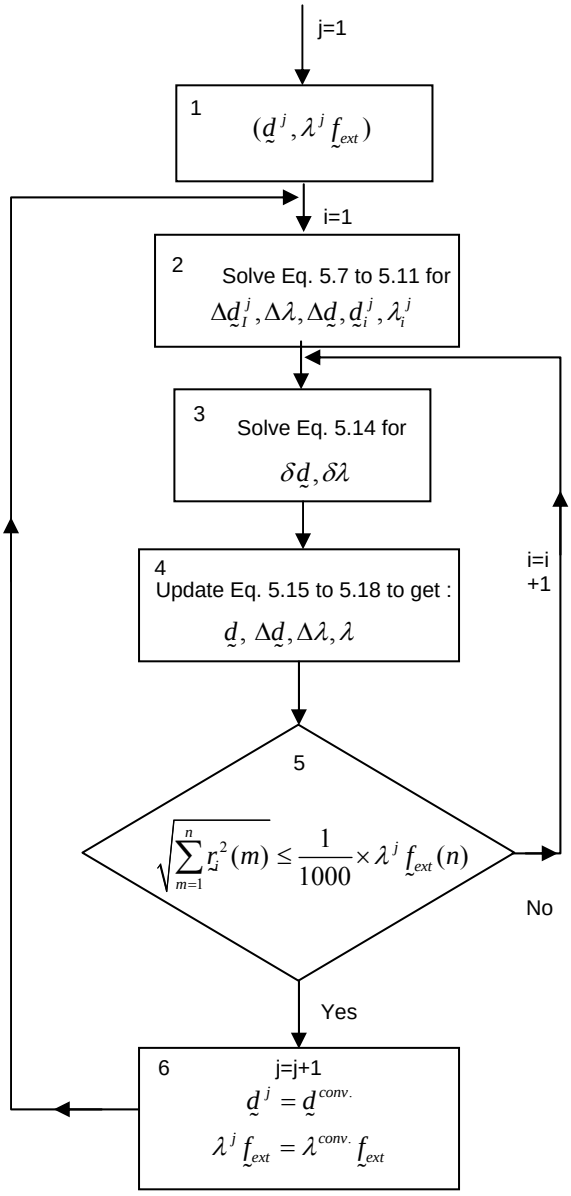

Figure 5.4: Flowchart for the algorithm of an explicit iteration using arc-length method

5.6 Results of the numerical analysis

A typical load versus global slip response obtained experimentally from a direct shear test for FRP bonded length equal to 150mm is shown in Figure 5.5 and compared to the response obtained from the numerical analysis showing a good agreement. The numerical analysis predicts that the load levels off at P_{crit} equal to 11.5 KN. Close to the point of observed ultimate failure in the experimental response, the load predicted by the numerical model starts to decrease below P_{crit}. It is also noted from Figure 5.5 that the load response obtained from the numerical analysis exhibits snapback beyond this point. The experimental load response does not capture the snapback since the test was performed in global slip control, which was set to increase at a constant rate and cannot accommodate a reversal in global slip (Bazant and Cedolin 1991).

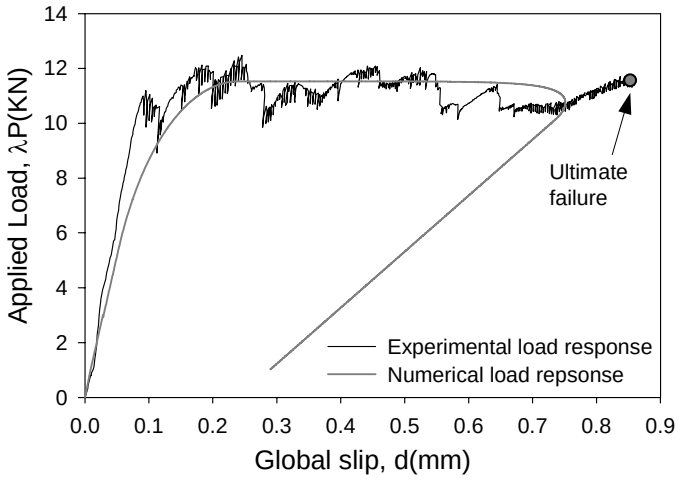

Figure 5.5: Comparison between experimental and numerical results for 150mm bonded length

Numerical results showing the load versus global slip for different bonded lengths of the FRP are presented in Figure 5.6. It is clearly seen that the bonded length significantly affects the load response. For bonded length smaller than 75mm, a post-peak softening is observed in the debonding response of the specimen. As the FRP

bonded length increases beyond 75 mm, the load response at failure exhibits snapback. Further increase in the bonded length beyond 75 mm results in an increase in the intensity of the snapback where the unloading stiffness of the specimen in the snapback portion decreases in magnitude. There also appears to be an increase in the maximum load transferred across the interface with an increase in the bonded length up to 85mm. However, if the bonded length is increased beyond 85mm, no additional increase in the ultimate capacity is possible.

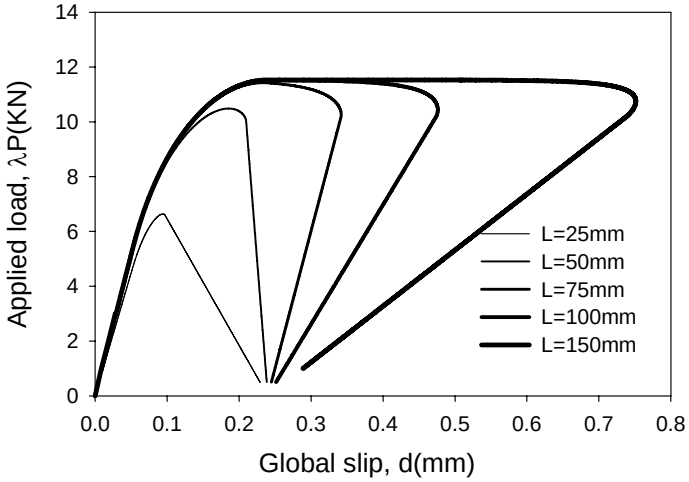

Figure 5.6: Numerically derived load versus global slip response for different FRP bonded lengths

The load response and the strain distributions along the FRP composite sheet at different values of global slip for a specimen with bonded length equal to 150mm are shown in Figures 5.7a and 5.7b, respectively. The corresponding relative slip between the concrete substrate and the FRP along the length of the FRP are shown in Figure 5.7c. It is observed that the load response becomes non-linear once the first interface element begins to soften when its relative slip exceeds s_o equal to 0.048mm. The load levels off at P_{crit} once the first interface material element is fully debonded, i.e. when the displacement of the first spring element exceeds s_f equal to 0.23mm. Analysis of strains

in the FRP for any point within the constant load, P_{crit}, portion of the load response demonstrates the existence of a constant stress transfer zone (STZ). Within the STZ, the relative shape of the strain distribution remains relatively fixed. At one end of the STZ, the strain in the FRP is essentially zero while at the other end it levels off at a constant value approximately equal to 6000με. The axial strain in the FRP reaches 6000με when the relative slip in interfacial spring element directly below the FRP is equal to s_f, i.e. when this portion of the interface has fully debonded and no longer transfers stress from FRP to concrete.

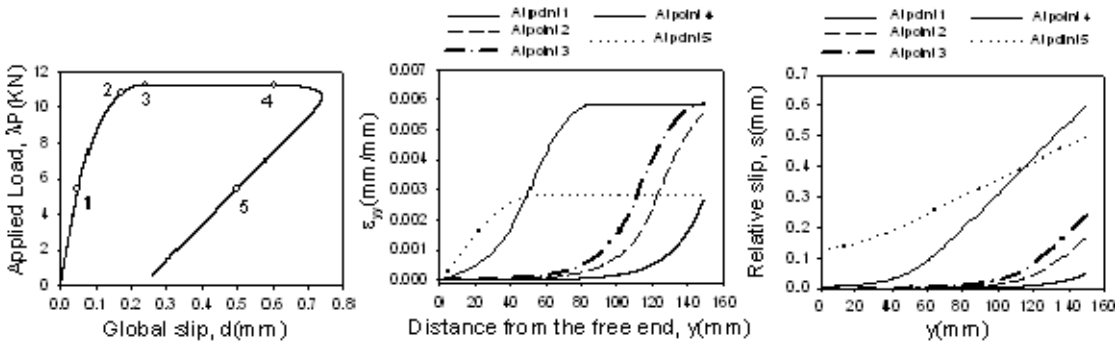

(a) **(b)** **(c)**

Figure 5.7: Numerical results for FRP bonded length equal to 150mm; (a) Load versus global slip response of FRP bonded to concrete; (b) Strain distributions along the FRP composite sheet at different global slip level; and (c) Relative slip versus location at different global slip level

The length of the constant stress transfer zone at P_{crit} is independent of the location of the crack along the FRP-concrete interface. As the crack propagates, a longer length of FRP is fully debonded from the concrete substrate. As the interface crack approaches the end of the bonded length, the load response exhibits snapback. During snapback, the decrease in the load is associated with the decrease in load carrying capacity of the remaining bonded length with an increase in the crack length. The decrease in the load point displacement is caused by the elastic unloading of the fully debonded FRP although the relative slip in the interface spring elements continues to

increase until complete debonding (shown in the strain distribution and relative slip corresponding to Point 5 of the load response in Figures 5.7b and 5.7c, respectively).

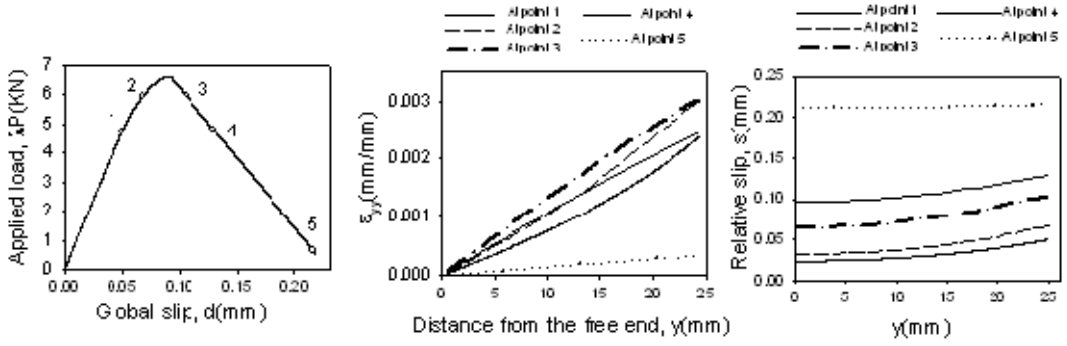

(a) **(b)** **(c)**

Figure 5.7: Numerical results for FRP bonded length equal to 150mm; (a) Load versus global slip response of FRP bonded to concrete; (b) Strain distributions along the FRP composite sheet at different global slip level; and (c) Relative slip versus location at different global slip level

The axial strain in the FRP and the relative slip in the interface for a specimen with bonded length equal to 25mm are shown in Figure 5.8b and 5.8c, respectively. Figures 5.8b and 5.8c indicate that the stress transfer is never fully established when the FRP bonded length is equal to 25mm. The relative slip between FRP and concrete at all points along the bonded length continue to increase throughout the loading process. The strain distribution in the FRP, however, initially increases with increasing load and then shows a decreasing trend as the load response exhibits softening. It is interesting to note that the first interface element does not completely debond when the load response exhibits softening. The softening in the load response begins when the relative slip in the first element reaches 0.0899mm. Thus, the load response exhibits softening when the relative slip in the first interfacial spring element exceeds s_o but lower than s_f and the first interface spring element stays bonded throughout the entire loading procedure.

Table 5.1: Statistical data of the fracture parameters

Random variables	$x=\tau_{max}$	$y=s_o$	$z=s_f$
Mean, μ	5.85	0.0384	0.18
Standard deviation, σ	1.23	0.0107	0.05
Correlation coefficient, ρ	ρ_{xy}=-0.87	ρ_{yz}=0.981	ρ_{xz}=-0.897

5.7 Effect of randomness in fracture parameters

Previously reported tests (chapter 3) on material properties of FRP composite laminates showed large variations in the ultimate strain. However, these tests also showed that Young's modulus of the FRP composite laminate is approximately constant and therefore can be assumed to be deterministic. In chapter 3, direct shear tests on FRP-concrete blocks showed that the strain on the concrete surface is practically negligible compared to that on the FRP surface and thus the concrete can be assumed rigid. Therefore, the load-global slip response of the specimen geometry of Figure 5.2 is primarily dependent on the material law of the FRP-concrete interface. On the other hand, large scatter were observed in the parameters of the material law for readings taken within the same specimen or for readings taken from different specimens prepared using the same concrete mix and adhesives. For this reason, the fracture parameters of the material law are treated as random variables to study the effect of the uncertainties in determining these parameters on the ultimate capacity and the failure mechanism of the FRP-concrete blocks. As discussed earlier, these parameters that define the material law are maximum shear stress, τ_{max}, the corresponding local relative slip, s_o, and the local slip at failure, s_f. All these parameters are considered as random and their means, standard deviations and correlation coefficients are provided in Table 5.1. It is clearly seen that the correlation between the fracture parameters is significant. To determine the

probability distribution type, the data points are plotted on normal probability papers. The plots showed that all three random parameters could be adequately modeled using normal probability distribution. For instance, Figure 5.9 plots the fracture parameter, s_f, on normal probability paper.

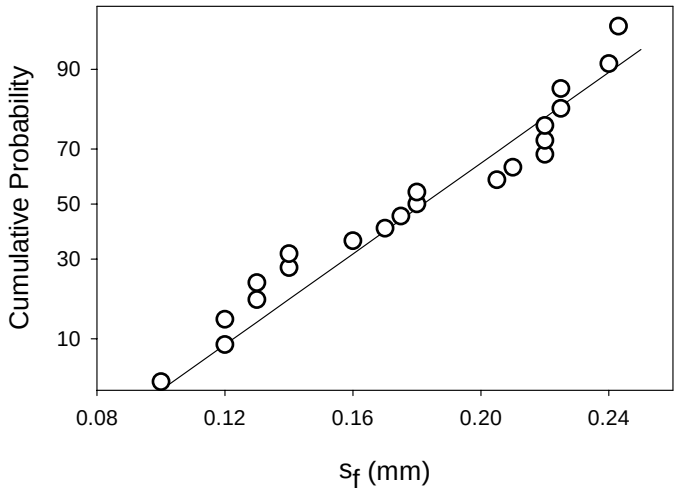

Figure 5.9: Relative slip s_f plotted on normal probability paper

To study the effect of the randomness in the three parameters on the specimen geometry of Figure 5.2, a Monte Carlo simulation is performed taking into consideration the correlation between the parameters. Pseudo-random data is generated for the fracture parameters ($x=\tau_{max}$, $y=s_o$) by correlating them to the third parameter ($z=s_f$) and a random variable r, using the relationships:

$$\begin{aligned} x &= \sigma_x (a_1 Z + R_1) + \mu_x \\ y &= \sigma_y (a_2 Z + R_2) + \mu_y \\ z &= \sigma_z Z + \mu_z \end{aligned} \tag{5.19}$$

where μ_x, σ_x, μ_y, and σ_y are the means and standard deviations of x and y respectively; Z, R_1 and R_2 are standard normal random variables with means equal to zero and standard deviations equal to 1; a_1 and a_2 are given by the following expressions:

$$a_1 = \frac{\rho_{xz}}{\sqrt{1-\rho_{xz}\rho_{xz}}}$$
$$a_2 = \frac{\rho_{yz}}{\sqrt{1-\rho_{yz}\rho_{yz}}} \tag{5.20}$$

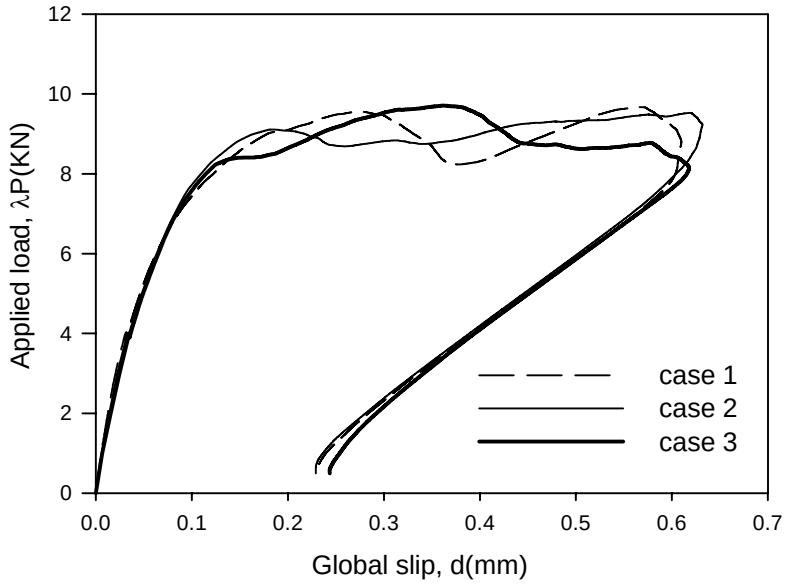

Figure 5.10: Load versus global slip response of FRP bonded to concrete generated for three different sets of fracture parameters

The analysis procedure described earlier in this chapter is applied for each set of parameters to determine the load versus global slip response of FRP bonded to concrete. The only difference in this analysis is that every spring of Figure 5.2b has one set of fracture parameters generated randomly, which differ from those of the other springs. This would simulate the effect of the random nature of the fracture parameters at the local level. The load versus global slip response for the specimen analyzed herein is shown in Figure 5.10. It is clearly seen that the load response does not level off at a constant load value as reported in Figure 5.5. The fluctuation shown in Figure 5.10 is due to the effect of the randomness of the fracture parameters. It is noticed that the overall load response is not affected by this local variation. The results of the numerical

analysis suggest that the uncontrolled and sudden response obtained experimentally at ultimate failure in the shear debonding of FRP from concrete is associated with snap-back instability.

5.8 Parametric studies

In the previous section, the results of the statistical analysis provided a means to understand the effect of the randomness in the fracture parameters on the load carrying capacity and the failure mechanism of the FRP-concrete blocks. This section presents a parametric study to gain a better understanding on how the number of FRP plies and the variation in the fracture parameters affect the debonding mechanism and the load response of the FRP bonded to concrete. In all studies, the bonded length is kept constant equal to 300mm. The results of the parametric study are summarized in Tables 5.2 and 5.3 and shown graphically in Figures 5.11, 5.12, 5.13 and 5.14.

Table 5.2: Variation of geometric variables

		Input/Given					Output/Results		
Study	Case	τ_{max} MPa	s_o mm	s_f mm	G_F MPa.mm	# plies	P_{max} KN	ε_{max} με	L_{stz} mm
1 # plies	I	5.74	0.048	0.23	0.66	1	10.39	5852	125
	II	5.74	0.048	0.23	0.66	2	14.68	4140	170
	III	5.74	0.048	0.23	0.66	3	17.99	3380	200
	IV	5.74	0.048	0.23	0.66	4	23.21	2620	255

In the first study, all fracture parameters were kept constant while the number of FRP plies was varied. It is clearly seen in Figure 5.11 that the load carrying capacity increases as the number of plies increases. The maximum strain, ε_{max}, and the relative

displacement between concrete and FRP decreases as the number of plies increases. It can also be noticed that the stress transfer length increases with the increase in the number of plies. This implies that the stresses are transferred through a longer length between the adherents.

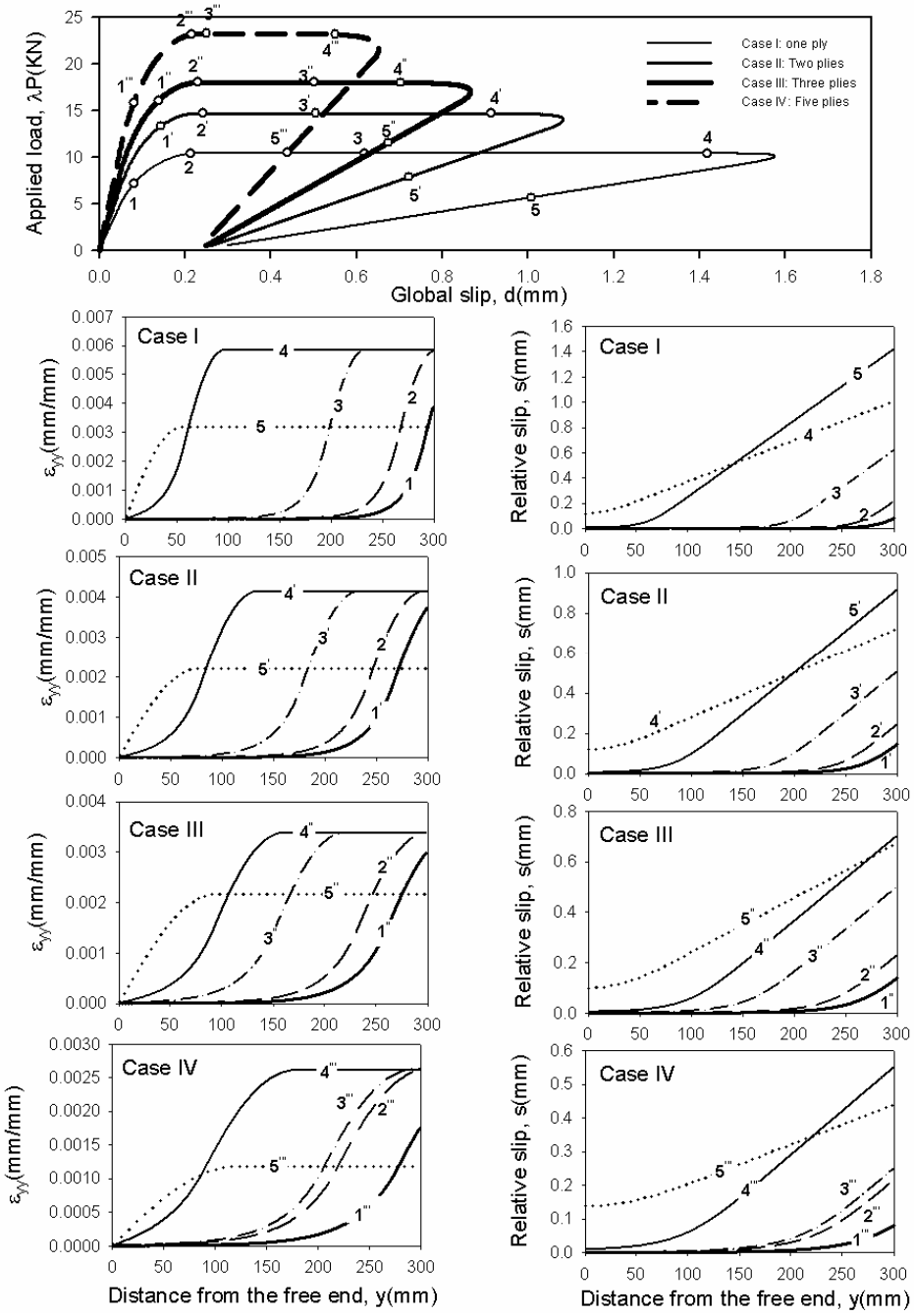

Figure 5.11: Parametric study 1 (different number of FRP plies)

Table 5.3: Variation of interracial fracture parameters

		Input/Given					Output/Results		
Study	Case	τ_{max} MPa	s_o mm	s_f mm	G_F MPa.mm	# plies	P_{max} KN	ε_{max} με	L_{stz} mm
2 G_F=constant	I	2.87	0.048	0.46	0.66	1	10.39	5852	200
	II	5.74	0.048	0.23	0.66	1	10.39	5852	125
	II	11.48	0.048	0.12	0.66	1	10.39	5852	85
3 τ_{max} varies	I	2.87	0.048	0.23	0.33	1	7.35	4145	175
	II	5.74	0.048	0.23	0.66	1	10.39	5852	125
	III	11.48	0.048	0.23	1.32	1	14.68	8277	95
4 s_f varies	I	5.74	0.048	0.12	0.33	1	7.5	4230	110
	II	5.74	0.048	0.23	0.66	1	10.39	5852	125
	III	5.74	0.048	0.46	1.32	1	14.68	8277	155

The second study consisted of three cases. τ_{max}, and s_f were varied from case to another while G_F and s_o were kept constant. The load versus global slip responses of all cases are shown in Figure 5.12. It is clearly seen that the ultimate load, P_{max}, remains constant for the three cases. This implies that if the bonded length and the number of FRP plies are kept constant, the load carrying capacity of the bond depends only on the interfacial fracture energy G_F. This is a significant finding, which states that if the bonded length is greater than L_{stz}, the load carrying capacity of FRP-concrete interface, P_{max}, depends only on the interface fracture energy, G_F. Therefore when G_F is constant, any variation of the three fracture parameters will not result in any change in P_{max}. Further, since ε_{max} depends on P_{max} and the elastic modulus of FRP, therefore ε_{max} depends only on G_F. However, the nonlinear zone (zones 1-3, 1'-3' and 1"-3" of Figure

5.12) and the intensity of the snapback phenomenon (zones 4-5, 4'-5' and 4"-5" of Figure 5.12) of each load response depends on the three parameters, τ_{max}, s_o and s_f even though G_F remains constant. Figure 5.12 also shows the axial strain distribution versus location from the free end. It is clearly seen that the maximum strain, ε_{max}, remains constant yet there is a decrease in the stress transfer length by comparing the three cases of Figure 5.12 (also shown in Table 5.3).

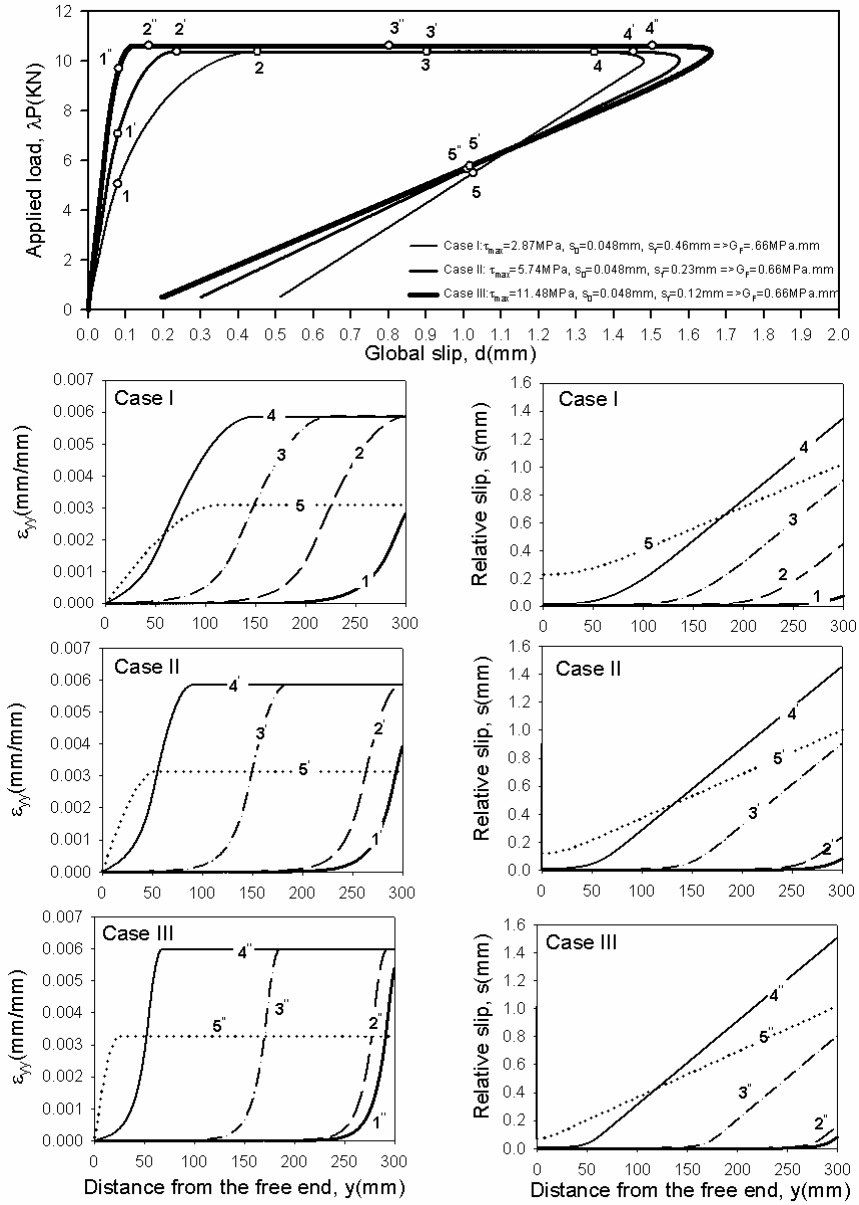

Figure 5.12: Parametric study 2 (G_F is constant)

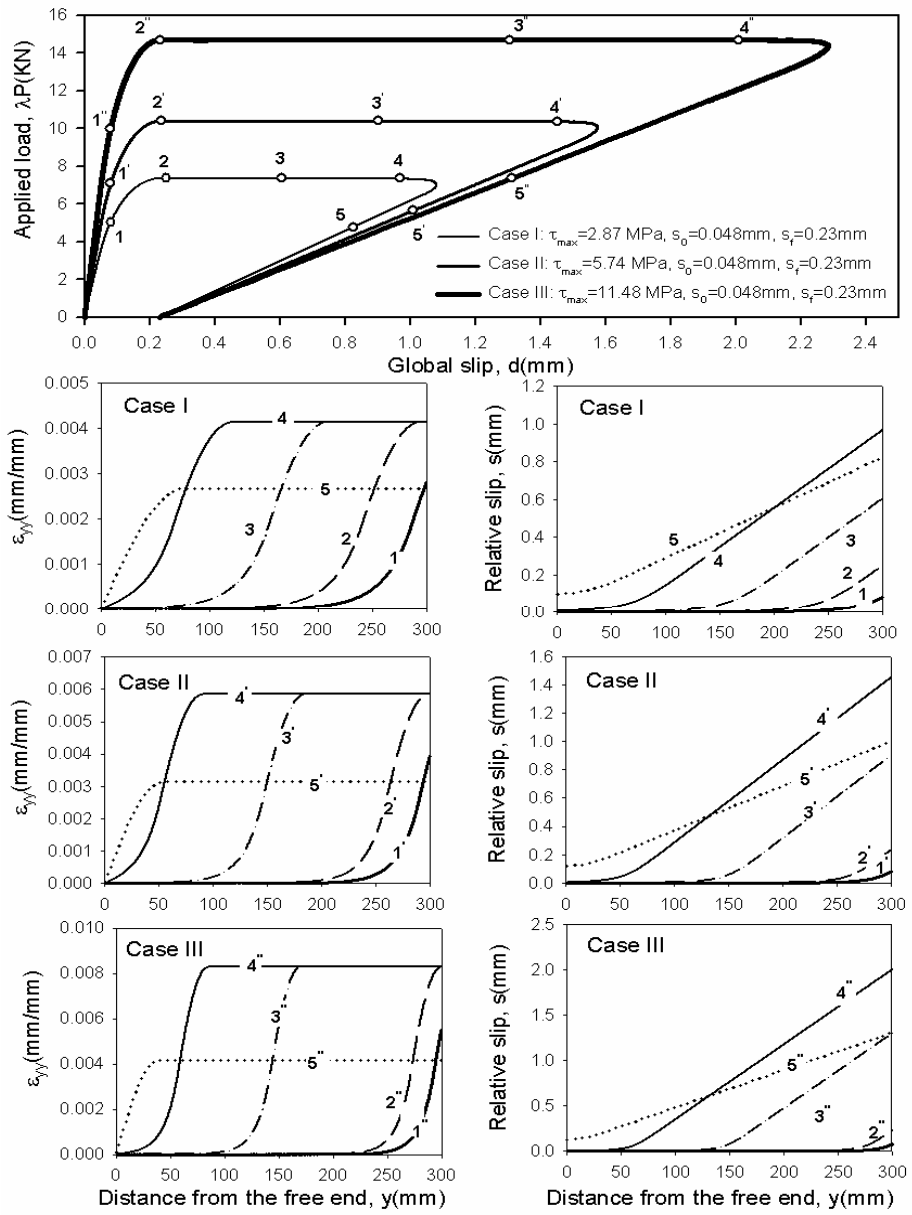

Figure 5.13: Parametric study 3 (Interfacial shear stress τ_{max} varies)

It can be noticed from Figure 5.13 that the load carrying capacity, P_{max}, and the maximum strain, ε_{max}, increases with the increase of τ_{max}. However, the stress transfer length decreases with the increase in τ_{max} and therefore with the increase in G_F. Although the relative slip s_f remains constant for the three cases of Figure 5.13, it is clearly seen that the global slip increases with the increase in τ_{max}.

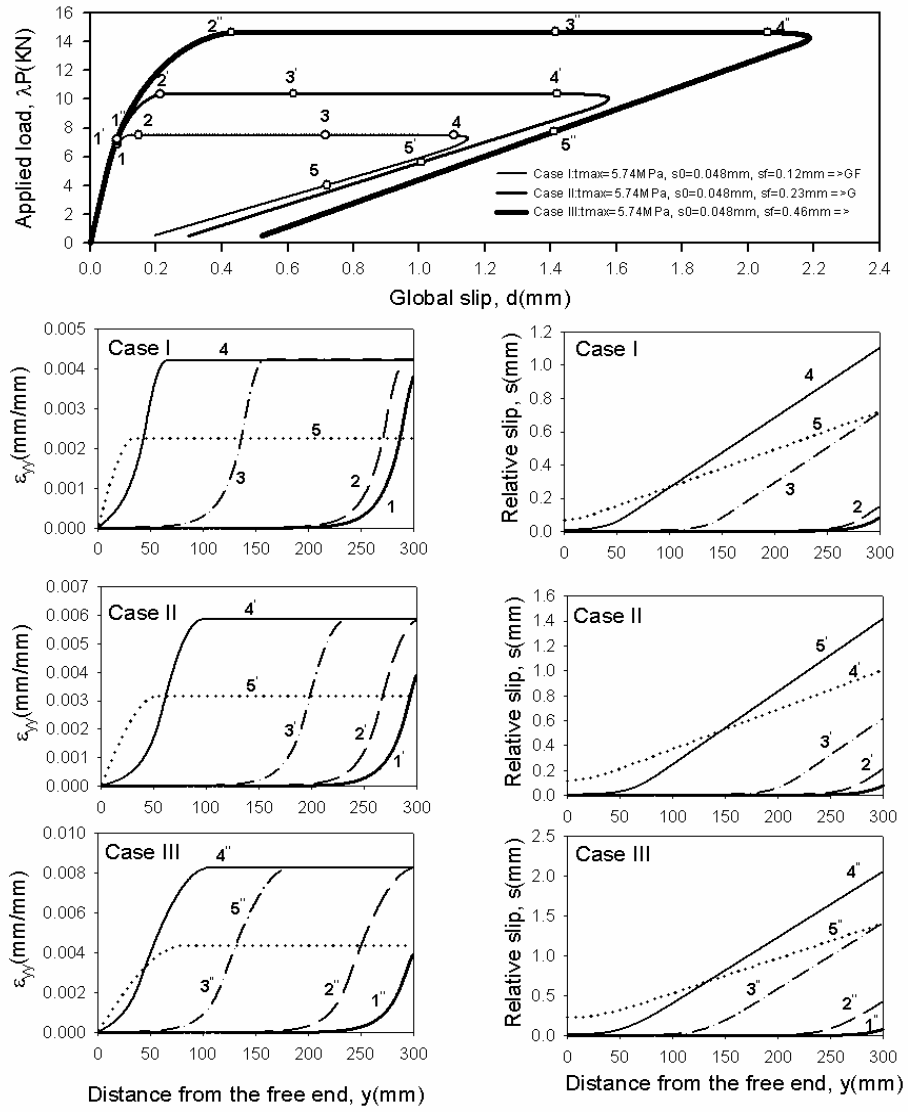

Figure 5.14: Parametric study 4 (horizontal intercept with softening curve, s_f, varies)

In the last study, the effect of the change in the slope of the softening curve on the stress transfer between concrete and FRP is investigated. It is clearly seen from Figure 5.14 that the ultimate capacity, P_{max}, and the maximum strain, ε_{max}, increases as the slope of the softening curve decreases. However, the stress transfer length slightly increases with the decrease in the slope of the softening curve.

For a given set of geometric variables and from the compiled results presented in Figures 5.12, 5.13 and 5.14, the variation in the fracture parameters is associated with

the following influence in the direct shear load-response: (a) the linear part of the load response depends on the initial slope of the τ-s curve as shown in Figure 5.14. Further in study 2, when s_o is fixed and τ_{max} is increased, the initial slope of the linear portion increases as shown graphically in Figure 5.12; (b) it has been previously established that the initiation of nonlinearity and attainment of P_{max} in the load response corresponds with the relative slip of the interfacial spring reaching s_o and s_f, respectively. The nonlinear ascending branch of the load response therefore depends upon s_f-s_o. Larger s_f-s_o corresponds with a larger nonlinear portion of the load response; (c) the load carrying capacity of the interfacial bond, P_{max}, depends only on the interfacial fracture energy, G_F.

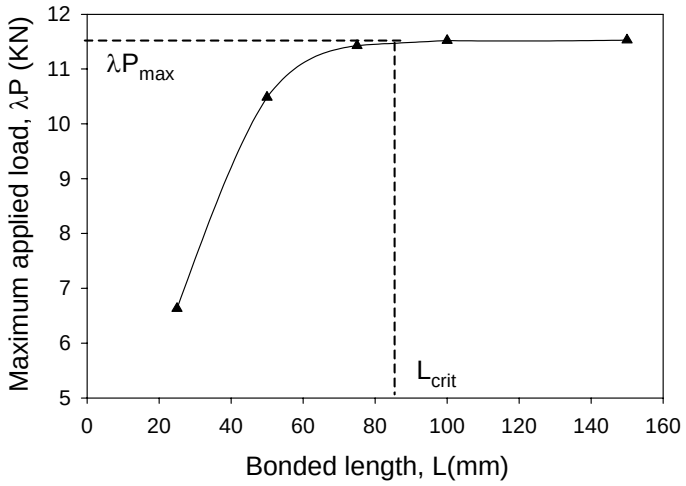

Figure 5.15: Maximum applied load versus FRP bonded length

5.9 Discussion

Figure 5.15 shows the maximum load that the FRP/concrete bond can sustain as a function of the bonded length. It is clearly seen that the maximum load increases with increasing bonded length up until it asymptotically reaches its highest possible value of P_{crit} equal to 11.5 KN. This highest value is reached when the bond length is

approximately equal to 85mm, which is equal to the length of the stress transfer zone, STZ. This confirms the presence of a critical length that is responsible for transferring the stresses between concrete and the FRP composite sheets. When the bonded length increases above 85mm, the maximum load level does not go any higher although the global slip increases. For bonded length greater than 85mm, self-similar crack growth is achieved in the portion of the load response where the load stays constant at P_{crit}; the stress distribution in the FRP remains constant relative to the crack. The stress transfer zone in this case is fully established, free from boundary effects.

It is interesting to note that when the bonded length is less than 50mm no snapback is observed and failure of the bond shows a softening response until the whole bond fails. Snapback is observed for cases when the bonded length exceeds 75mm, which indicates that the snapback occurs before the stress transfer zone is fully established.

The snapback part of the equilibrium becomes more pronounced (and thus more dangerous) as the bonded length increases. Once the crack propagates to a point close to the end of the bonded area, the load carrying capacity of the uncracked ligament starts to decrease with additional crack growth. Snapback results from the elastic unloading of the FRP. This phenomenon, which is associated with a sudden release of elastic energy, would result in a catastrophic failure of the bond and becomes more dangerous as the bonded length increases. Therefore, the observed snapback in the shear debonding response may lead to catastrophic failures in large structures as the interfacial crack approaches the end of the bonded length.

Snap-back has been reported in other structures and specimens geometries where the failure is associated with localized damage confined to a small region relative to the specimen size (Janson and Shah 1997, Bazant and Cedolin 1991, Subramaniam et al. 1998). Obtaining the complete test response experimentally, including the snap-back, is often very challenging. To capture the full experimental load response of the specimen up to complete debonding (down to zero load), the elastic displacement of the debonded FRP sheet has to be subtracted from the global slip using a combined feedback signal (Subramaniam et al. 1998).

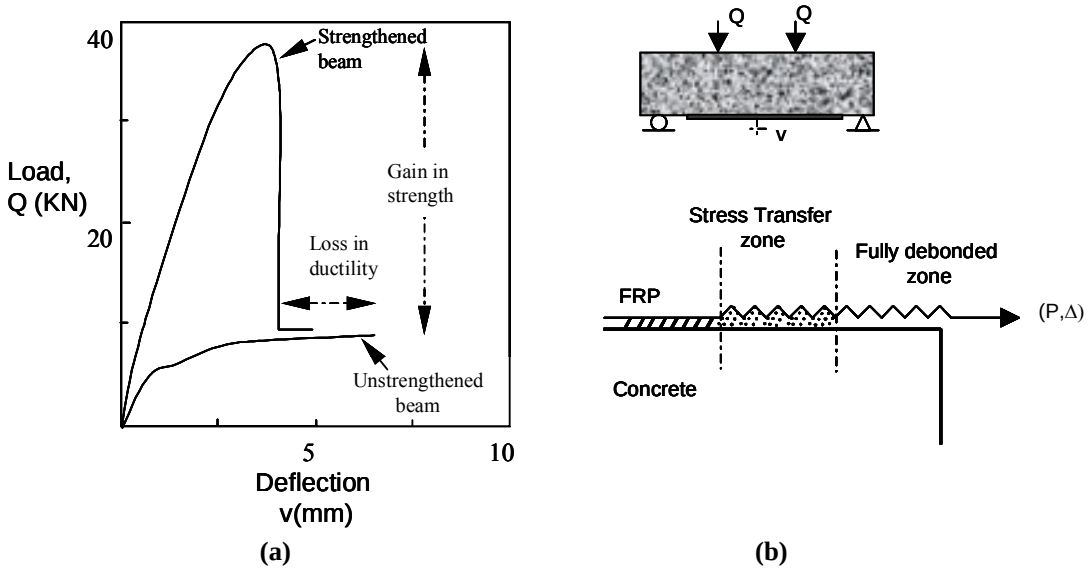

Figure 5.16: Load defection response for CFRP-strengthened concrete beam (Triantafillou and Pelvris 1991); (a) Load-deflection curve; and (b) Schematic representation of the crack propagation along the FRP-concrete interface

The numerical results presented in this chapter combined with the experimental results reported in chapter 3 provide a means for providing a conceptual explanation of the explaining the load response of strengthened concrete beams as described in Figure 5.16a. Assuming that the bonded length of FRP is greater than the stress-transfer length, the debonding of the FRP will be initiated at an existing flexure or a shear-flexure or a shear crack. Once initiated, the increase in length of the interfacial crack is associated

with a constant load in the FRP at the location of the crack. Further, since the stress transfer length does not change with the crack location, the stress transfer region can be assumed to be of fixed compliance. As the crack propagates, a longer length of FRP is fully debonded from the concrete substrate. Therefore, the compliance of the fully debonded FRP increases with interfacial crack growth.

The propagation of a crack in the FRP-concrete interface can be schematically represented by two springs in series attached to a concrete substrate as illustrated in Figure 5.16b. The springs in Figure 5.16b represent the stress transfer zone and the fully debonded FRP composite sheet. While the spring constant associated with the stress transfer length is of fixed magnitude, the spring that represents the portion of the FRP that is completely debonded increases in length as the crack advances. The spring associated with fully debonded FRP however has a fixed stiffness per unit length. Since there is no drop in load associated with crack propagation, this implies that the strain energy stored in the fully debonded portion of FRP increases quadratically with an increase in the crack length. Finally, when the crack propagates to the end of the bonded region, the FRP completely separates from the beam. However, at this point the strain energy accumulated in the stressed FRP is suddenly released. At the same instant, the capacity of the beam that has been completely detached from the FRP strip has decreased to the capacity of the unstrengthened beam. The sudden release of energy associated with the complete detaching of the FRP will result in dynamic response of the unstrengthened beam which could potentially cause a catastrophic failure.

In this simplified formulation the effect of friction along the length of the fully debonded FRP is ignored. If friction between FRP and concrete was considered, friction

would oppose the relative shear movement of the fully debonded FRP relative to the concrete surface. The applied force required to produce debonding at a given location would then increase as the interfacial crack progressed along the length of the FRP. This would result in higher elastic energy stored in the fully debonded FRP and hence a more catastrophic failure when the energy is released. This release of energy would result in a dynamic response of the unstrengthened beam, which might collapse depending upon the magnitude of the energy released and the capacity of the unstrengthened beam.

This qualitative analysis demonstrates that the complete debonding of FRP from the concrete beam produces a sudden failure. For this reason, the conditions that lead to a debonding mode of failure become very important to analyze. Debonding does not simply return the beam's strength to its original value but may cause a catastrophic failure, which may lead to the collapse of the structure. This indicates that any analysis to predict the load-deflection response of FRP strengthened bridge girder must consider the progressive debonding failure and should not rely on the modeling of the strength of fully bonded beams.

5.10 Conclusions

Based on the results presented in this chapter the following conclusions can be drawn:

1) Shear debonding between FRP and the concrete substrate can be adequately modeled using an experimentally derived material law for the interface, which exhibits softening behavior.

2) The arc-length method provides a means to numerically analyze the full behavior of debonding at the FRP-concrete interface.

3) The results of the numerical analysis demonstrate that the shear failure of the FRP-concrete bond from concrete may lead to snap-back instability.

4) The results of the numerical analysis confirm the presence of a critical length that is responsible for transferring the stresses between concrete and the FRP composite sheets. However, using a bonded length greater than the critical length does not improve the ultimate capacity of the bond.

5) The observed snap-back in the load response depends upon the bonded length of the FRP. It is shown that the short bonded lengths do not exhibit snap-back, while the intensity of the snapback increases with an increase in the bonded length beyond 85mm.

6) The progressive shear debonding at the FRP-concrete interface may produce a sudden release of energy associated with the snapback mechanism resulting in catastrophic failure.

7) The randomness in the fracture parameters does not significantly affect the overall load response of concrete externally strengthened with FRP.

8) The higher the fracture energy the better load carrying capacity of the bond. Any change in the fracture parameters, τ_{max}, s_o and s_f with a constant G_F will not affect the load carrying capacity and the maximum strain in the FRP. The load carrying capacity is increased with the increase on the FRP axial stiffness.

CHAPTER 6

FAILURE ANALYSIS OF FRP-STRENGTHENED CONCRETE BEAMS

6.1 Overview

In this chapter, analysis of the load response of concrete beams strengthened using externally attached FRP sheets is presented. The nonlinear material law of the FRP-concrete interface, which considers the shear-debonding mode of failure, is incorporated into a numerical model for predicting the load-deflection response of FRP-strengthened beams. The load response obtained numerically is compared with existing experimental results. Previous researchers have shown that the initiation of debonding at the FRP-concrete interface in FRP-strengthened concrete members is due to the rapid propagation of localized flexural cracks (Yin and Wu 2003, Teng et al. 2004). The objective of the numerical analysis performed in this chapter is to obtain a fundamental understanding of the interfacial crack propagation phenomenon in FRP-strengthened concrete beams using the material law developed in the earlier chapters. The strain distributions from the numerical analysis are compared with the strains obtained using the conventional sectional analysis. The results show that the recommendation suggested by ACI to use strain-based failure criteria obtained from direct shear tests is not valid for

beams strengthened in flexure. The strain-based criterion can however be used for predicting debonding in shear strengthening applications. Finally, a debonding failure criterion for flexural strengthening based on the strain gradients along the FRP composite is proposed.

6.2 Introduction

Carbon fiber reinforced polymer (CFRP) sheets are being used as a strengthening solution to retrofit deteriorated concrete structures. In typical strengthening applications, the FRP is used to increase the existing shear or flexural capacity of the beam. In such applications, the FRP-concrete interfacial bond becomes a key factor that controls the efficiency of the repair. In recent years, efforts have been made to study the interfacial stress transfer between concrete and FRP. In shear strengthening applications, the FRP composite provides tensile forces across the shear crack, which prevents the opening of the crack, thereby increasing the overall load carrying capacity of the beam. The high shear stress concentration along the FRP-concrete interface close to the crack edge results in the initiation of an interfacial crack. The understanding of the interfacial debonding mechanism and the ultimate failure of the FRP strengthening system developed from direct shear tests is directly applicable for the case of shear strengthening of beams. In beams where FRP sheets provide flexural strengthening, the stress concentration at the flexural cracks causes the initiation of a crack in the FRP-concrete interface that propagates from the middle of the beam towards the supports (Wu et al. 1997, Leung 2004). Several analytical models have been proposed to investigate the load response of RC beams externally strengthened with FRP (El-Milhimy & Tedesco 2000, Arduini et al. 1997, Wang and Ling 1998). In these models, it

is implicitly assumed that the failure of the strengthened beam can usually be achieved before the failure of the bond between the FRP and concrete. When debonding initiates from the center of the beam, the assumption of perfect bond between the adherents is no longer valid and therefore models based on sectional analysis become unreliable in predicting the ultimate load and the load-deflection response of the beam.

Many researchers presented numerical models based on the finite element analysis for predicting the load response of FRP strengthened beams and for studying the stress redistribution along the FRP sheets/plates (Malek et al. 1998, Arduini et al. 1997, Wu and Niu 2000, Lopez et al. 2000). In these models, the simplified assumption of perfect bond between FRP and concrete was utilized. Such analyses accurately predict the stress in the FRP resulting from a change in length produced by curvature and can also potentially predict the shear stress concentration along the interface close to a flexural crack. However, the initiation and propagation of the interfacial crack can not be studied under the assumption of perfect bond. A few detailed numerical analyses aimed at studying the effect of flexural cracking in concrete on the debonding behavior in FRP strengthened beams have recently been reported in the literature (Wu and Yin 2003, Teng et al. 2004). In these studies, the beam was modeled as a plane stress problem and the FRP-concrete interface was modeled using fictitious crack models. The simulations performed by Wu and Yin (2003) were based on assumed interfacial fracture parameters. The experimental and numerical results obtained by Teng et al. (2004) however did not show favorable comparison after initiation of debonding. A clear understanding of the initiation of debonding in the beam and the influence of debonding on the load response and the load carrying capacity of the strengthened beam is still

emerging. Several key questions that remain unanswered are: (a) can the initiation of debonding be predicted in a strengthened beam using the conventional sectional analysis procedure? (b) what is the influence of debonding on the load response of a strengthened beam? (c) is the strain-based criterion recommended by ACI for failure in beams that exhibit debonding safe? (d) should initiation of debonding be considered as the ultimate failure criterion of the strengthened beam? and (e) how can the information generated from the direct shear test be used for predicting debonding in beams?

In this chapter, the behavior of plain concrete beams that are strengthened in flexure using externally attached FRP composite sheets is analyzed. A preliminary analysis based on the simplistic assumptions of linear elastic fracture mechanics is performed to study the debonding mechanism at the FRP-concrete interface. This analysis is used to establish a fundamental basis for the interfacial debonding. In the second part of this chapter, a three-dimensional finite element analysis considering the cohesive material law for the FRP-concrete interface and smeared cracking for concrete in tension is presented. The load response obtained numerically from the latter analyses is compared with existing experimental results. The initiation of interfacial debonding, the progressive crack growth and the ultimate failure of FRP-strengthened concrete beams are investigated. It is shown that after initiation of debonding, the load-deflection response exhibits a softening behavior associated with progressive interfacial crack growth. A comparison of the ultimate load capacity and initiation of debonding predicted by sectional analysis is also performed. The implications of these findings on the current practice are discussed.

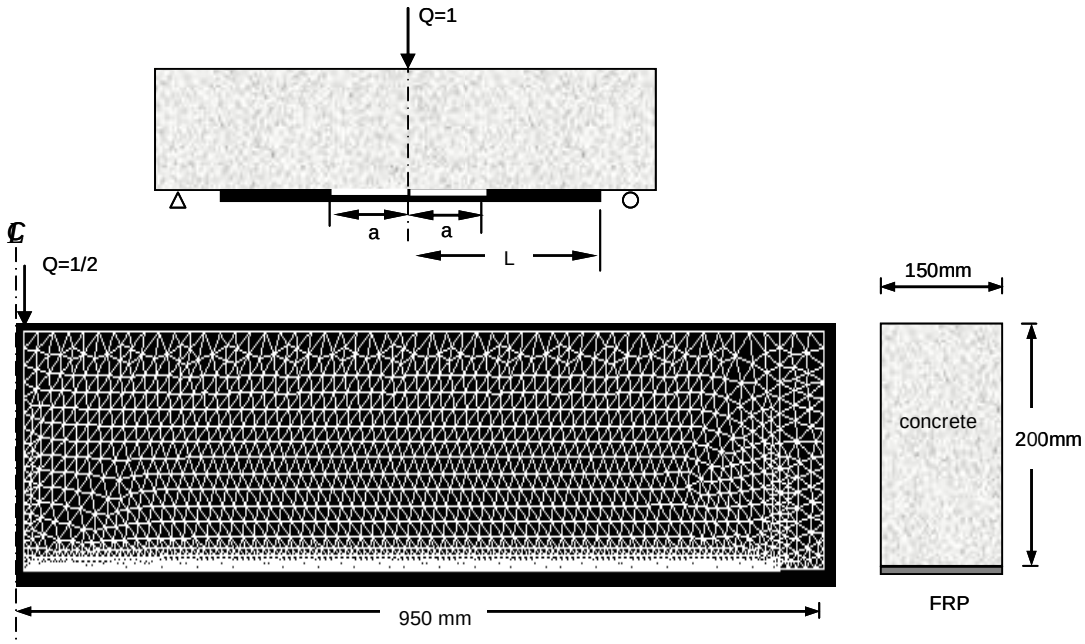

Figure 6.1: Discretized geometry of the strengthened beam modeled using the concept of LEFM

6.3 Linear elastic fracture analysis

The concept of linear elastic fracture mechanics (LEFM) is applied in this section to gain a general understanding of the debonding mechanism at the FRP-concrete interface in a concrete beam externally strengthened using FRP composite sheet. The objectives of this analysis are: (a) to study if progressive debonding is possible under flexural loading; and (b) to check if a stable load response can be obtained in a beam that exhibits interfacial debonding between FRP and concrete.

To study the stated objectives, a simplistic modeling approach is considered where debonding between FRP and concrete is the only damage mechanism. All materials are assumed to be linear elastic and the crack growth between the FRP and the concrete is dictated by the critical stress intensity factor. Numerical analyses were performed for the strengthened beam shown in Figure 6.1 by varying the interface crack

length. The nominal dimensions of the concrete beam are as follows: length (1900mm), width (150mm) and height (200mm). The thickness and the bonded length of the FRP were equal to 0.1mm and 850mm, respectively. Because of the symmetries in the beam geometry and the loading condition, only half of the beam was considered for the analysis. The beam and the FRP were modeled using six-noded triangular elements available in FRANC2D (Ingraffea and Wawrzynek 1994). The concrete and FRP were assumed to be linear elastic. Singular quadratic elements where the mid-side nodes were placed in the quarter points are used at the crack tip. Perfect bond between the FRP and concrete was assumed.

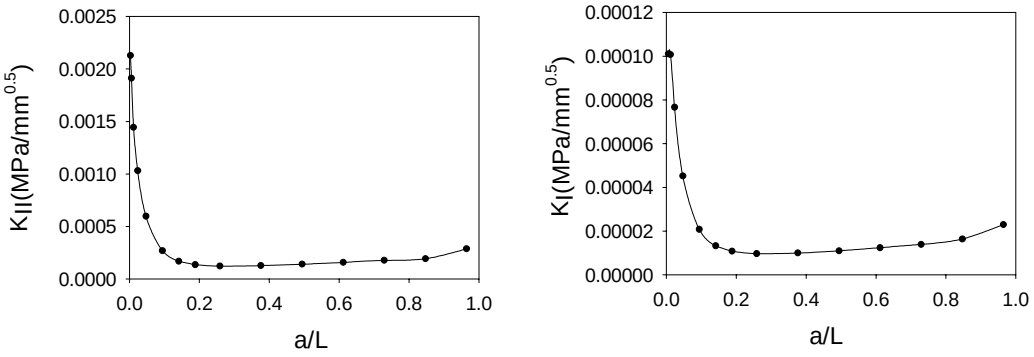

(a) **(b)**

Figure 6.2: Stress intensity factors; (a) K_{II} versus normalized crack length; and (b) K_I versus normalized crack length

The strengthened concrete beam is loaded in three-point bending where a unit load is applied at midspan. An interfacial crack of length, a, between the FRP and concrete was introduced. The analysis was performed using the finite element solver available within FRANC2D, considering a unit-applied load on the beam. The results of the analysis were used to determine the mode I and II stress intensity factors at the crack tip. The analysis procedure was repeated for incrementally larger interfacial crack

lengths. The stress intensity factors, K_I and K_{II} for the given geometry are plotted in Figure 6.2 as a function of the interface crack length. It is clearly seen that the value of K_{II} is an order of magnitude larger than that of K_I. Thus, the interface crack propagation can be treated as a mode II problem. Further, it can also be seen that K_{II} obtained from a unit applied load decreases rapidly with an increase in the crack length. The crack growth along the interface can now be predicted using the failure criterion obtained from LEFM, which is given as,

$$K_{II} = K_{IIc} \tag{6.1}$$

where K_{IIc} is the critical mode II stress intensity factor for the interface. K_{IIc} is considered a material constant in this analysis. From the failure condition given in Equation 6.1, the maximum applied load can be estimated for each crack length as

$$Q(a) = \frac{K_{IIc}}{K_{II}(a)} \tag{6.2}$$

where Q(a) is the maximum applied load for a given crack of length equal to a. Using an assumed value of K_{IIc} equal to 346 MPa.mm$^{-0.5}$, the value of Q(a) determined for the different crack lengths is plotted in Figure 6.3. The assumed value for K_{IIc} is obtained from the linear elastic portion of the material law obtained in earlier chapters and is assumed to be valid in this example for the purpose of obtaining an understanding of the crack propagation phenomenon. The following sections of this chapter utilize a nonlinear fracture analysis that would more realistically model the true behavior of the strengthened beam. In Figure 6.3, the load has been normalized with respect to the maximum applied load, Q_{max}. It is clearly seen that the applied load initially increases with an increase of crack length up to Q_{max}. The load reaches the peak when the ratio a/L is approximately equal to 0.25. After Q_{max}, an increase in a/L is associated with a

decrease in the applied load. This simple analysis demonstrates that interface crack growth in a strengthened beam is associated with a stable load response until the crack grows to a critical length.

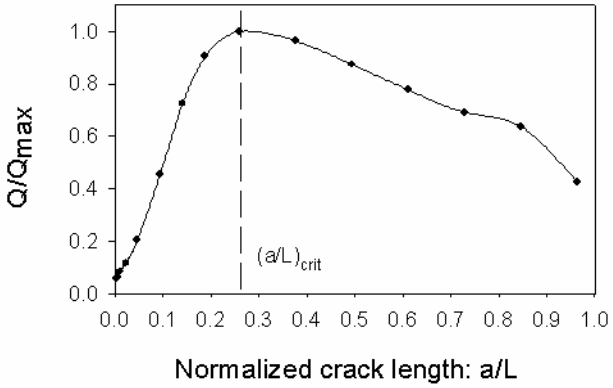

Figure 6.3: Normalized applied load versus normalized crack length

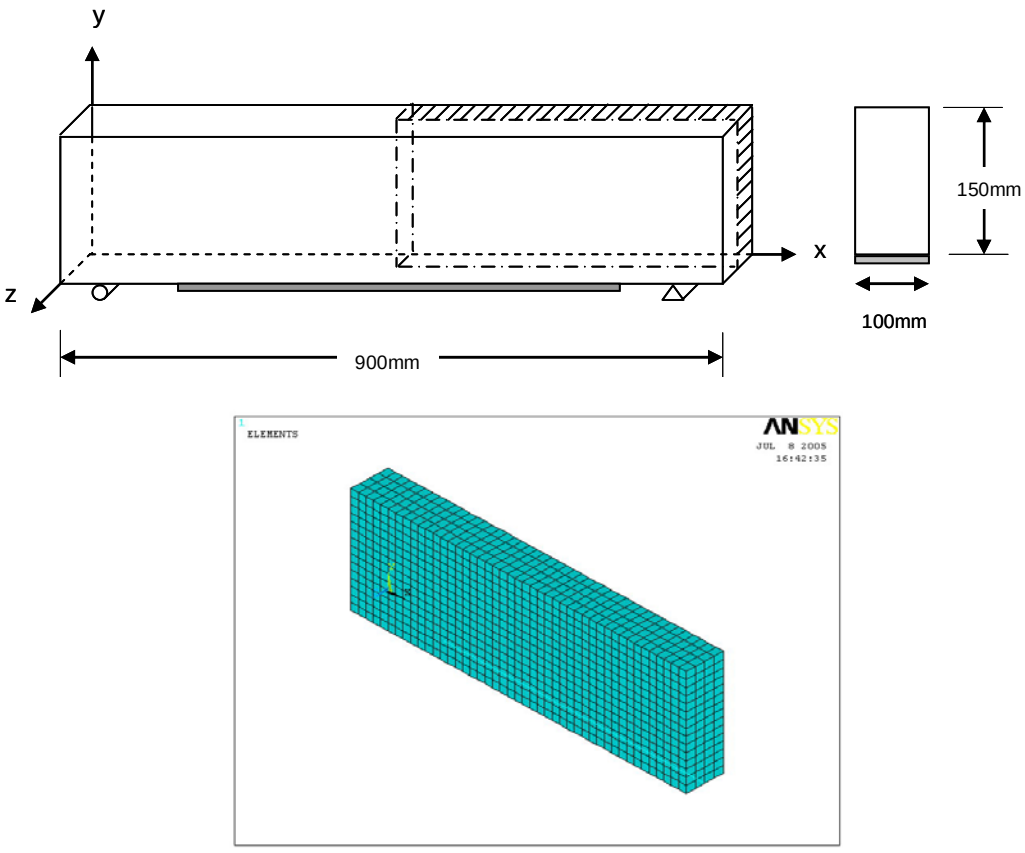

Figure 6.4: Quarter symmetry of the finite element model of the FRP-strengthened concrete beam

Based on the results of the preliminary analysis presented in this section, the following conclusions can be drawn: (a) the mode II crack propagation is the predominant component when debonding is initiated close to the midspan; (b) a FRP-concrete interfacial crack that forms at midspan will propagate towards the support; and (c) the interfacial crack growth is stable up to $(a/L)_{crit}$; increasing load is required to drive the crack growth. After $(a/L)_{crit}$, the load response shows softening. This indicates that the maximum load decreases with an increase in crack length past $(a/L)_{crit}$. In order to validate these conclusions, the following sections present more sophisticated analyses based on the nonlinear finite element method. The numerical results are compared with experimental results published in the existing literature.

6.4 Nonlinear finite element analysis

A finite element analysis of two plain concrete beams strengthened using externally bonded FRP sheets is presented in this section. The two beams have identical dimensions but different material properties. The strengthened beams are loaded in a three-point bending configuration. The dimensions of the concrete beams are: length (900mm), width (100mm), and height (150mm) as shown in Figure 6.4. The FRP composite was attached to the tension side over the full width of the specimen using an epoxy based adhesive with a bonded length equal to 700mm. The experimental load response of the beam was obtained experimentally by Wu et al. 1998. Details of the finite element discretization, analysis of results of the numerical analysis and a comparison between the experimental and numerical load responses are presented in the following sections.

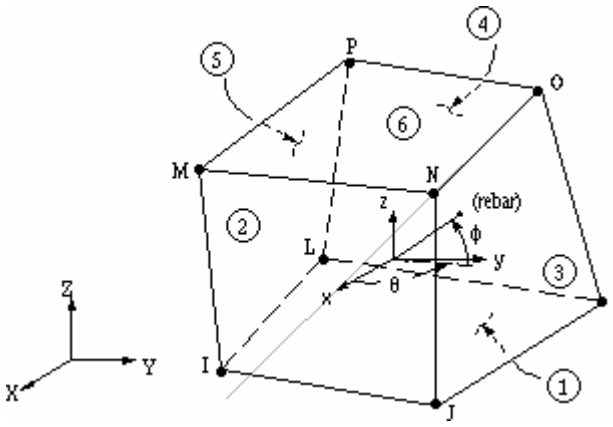

Figure 6.5: SOLID65 three-dimensional reinforced concrete element (ANSYS™ 6.0)

6.4.1 FE discretization

The commercial software, ANSYS, was used to build a three-dimensional model of the concrete beam externally strengthened with FRP composite sheets. By taking advantage of the symmetries, only a quarter of the strengthened beam is modeled as shown in Figure 6.4. The displacements perpendicular to the planes of symmetry are set to zero. A three-dimensional solid element, SOLID65, which is capable of treating material nonlinearities, cracking in three orthogonal directions, crushing, creep and plastic deformation was used to model the concrete (Figure 6.5). A two node three-dimensional axial element, LINK10, with no bending stiffness was used to model the FRP composite sheet. The FRP-concrete interface was modeled using a two-node-three-dimensional nonlinear spring element, COMBIN39. This element is capable of handling softening where increasing displacement is associated with a decrease in the spring force.

6.4.2 Material properties and failure criterion

In order to compare the numerical load response with that observed experimentally by Wu et al. 1998, the material parameters for the FRP-concrete

interfacial material law are taken from the study performed by the same authors (Wu and Yin 2003). The interfacial material law is expressed in terms of the interfacial shear stress, τ, and the relative displacement, s, between the FRP and concrete. A bilinear representation of the interfacial material law is assumed as shown in Figure 5.2. The parameters of the bilinear response used in this analysis are summarized in Table 6.1. It can be seen that the values of τ_{max} and s_f for beam 1 are almost double those for beam2. Thus, the toughness of the FRP-concrete interface of beam1 is higher than the toughness of the interface in beam 2.

Table 6.1: Material and fracture properties

Beam Label	Material properties of concrete			FRP-concrete interface fracture parameters (Mode II)		
	E_c(MPa)	f_c' (MPa)	f_t (MPa)	τ_{max}(MPa)	s_o(mm)	s_f(mm)
1	27036	26	2.0	3.0	0.0112	1.33
2	27139	30	3.30	1.8	0.0112	0.56

The material properties of the FRP composite are based on the thickness of the fibers contained in the composite sheet. The material response of the CFRP is considered to be linear elastic up to failure. The fiber thickness, t, Young's modulus, E_{FRP}, and Poisson's ratio, ν of the FRP composite are equal to 0.11mm, 2.3×10^5 MPa and 0.3, respectively.

The material properties of concrete for the two beams are given in Table 6.1. It can be seen that the concrete in beam 2 has a significantly higher tensile strength when compared with that of beam 1. Concrete is modeled as a multilinear isotropic hardening

material. The failure criterion for concrete due to multiaxial stress state is expressed in the following form (William and Warnke 1974):

$$\frac{F}{f_c^{'}} - S \geq 0 \tag{6.3}$$

where F is a function of the principal stress state (σ_1, σ_2, and σ_3); S is a failure surface expressed in terms of the principal stresses as well as the compressive and tensile strengths $f_c^{'}$, and f_t. In typical conditions of beams subjected to flexural loadings ($\sigma_1 \geq \sigma_2 \geq 0 \geq \sigma_3$), the functions F and S takes the following forms:

$$F = \sigma_i;\ i = 1,2 \tag{6.4}$$

$$S = \frac{f_t}{f_c^{'}}\left(1 + \frac{\sigma_3}{f_c^{'}}\right);\ i = 1,2 \tag{6.5}$$

If the failure criterion is satisfied for i=1 and 2, cracking occurs in the planes perpendicular to principal stresses σ_1 and σ_2, respectively. The presence of a crack at an integration point is modeled through modification of the elastic isotropic stress-strain matrix, $\underset{\sim}{D}_c$. In this case, $\underset{\sim}{D}_c$ is adjusted by introducing a plane of weakness in the direction normal to the crack face and becomes $\underset{\sim}{D}_c^{ck}$.

$$\underset{\sim}{D}_c^{ck} = \begin{bmatrix} \underset{\sim}{D}_n & \underset{\sim}{0} \\ \underset{\sim}{0} & \underset{\sim}{D}_s \end{bmatrix} \tag{6.6}$$

where $\underset{\sim}{D}_n$ is function of the elastic modulus of concrete, E, Poisson's ratio,ν, and the tensile softening modulus, R^t; $\underset{\sim}{D}_s$ is function of E, ν and the shear transfer coefficients for closing and opening cracks, β_c and β_t, respectively.

In ANSYS, a total of nine concrete material parameters are required to define the failure criterion including the cracking and crushing options. These parameters are: (a)

shear transfer coefficients for an open crack; (b) shear transfer coefficients for a closed crack; (c) uniaxial tensile cracking stress, f_t; (d) uniaxial crushing stress, $f_c^{'}$; (e) biaxial crushing stress; (f) ambient hydrostatic stress state; (g) biaxial crushing stress under the ambient hydrostatic state; (h) uniaxial crushing stress under the ambient hydrostatic stress state; and (i) stiffness multiplier for cracked tensile condition. A value of -1 for f_t or $f_c^{'}$ removes the cracking or crushing capability. In this analysis, the crushing capability of concrete is removed and both shear transfer coefficients were set to be equal to 0.5. Typical shear transfer coefficients vary from 0 to 1, where 0 represents a smooth crack while 1 represents a rough crack. Convergence problems occurred when the shear transfer coefficient for the open crack was chosen to be equal 0.3. No change in the load response was observed with the change of the coefficients. Therefore, both coefficients were chosen to be equal to 0.5. The constants of (e) through (i) were assigned the default values as recommended by William and Warnke (1974) for low hydrostatic stress component. The default values are specified as functions of the ultimate uniaxial compressive concrete strength.

6.4.3 Analysis procedure and convergence criterion

The load response of the strengthened beam was obtained by increasing the midspan vertical displacement in fixed incremental steps. In the analysis procedure available in ANSYS, the vertical displacement within each step is applied in increments over a certain number of substeps to obtain an accurate solution. The number of steps, maximum number of substeps and minimum number of substeps were specified by trial and error procedure so that a higher number of substeps did not result in an improvement in the load response. The sparse direct solver that is based on a direct elimination of

equations was used as the solution option. This solver is suited for nonlinear analyses where robustness and speed are required. Since the sparse direct solver is based on direct elimination, poorly conditioned matrices do not pose any difficulty in producing a solution (ANSYS^{TM} 6.0). The convergence criterion for each substep was based on the square root sum of the squares (SRSS) of the force imbalances against a prescribed value, which is the SRSS of the applied load multiplied by a tolerance equal to 0.5%.

6.5 Results of the numerical analysis

6.5.1 Results of beam 1

The load versus defection response obtained experimentally from a strengthened beam tested by Wu et al. (1998) is shown in Figure 6.6 and compared to the response obtained from the numerical analysis showing reasonably good agreement. The load response obtained from the finite element analysis is almost linear up to the point where the first flexural crack forms in the bottom fibers of the concrete. The initial flexural crack forms near the midspan of the strengthened beam at a load approximately equal to 9 KN. This load is found to be lower than the load observed experimentally. This cracking is associated with a sudden decrease in the flexural stiffness of the section at midspan, which manifests itself by a sudden drop of load observed in the numerical results. After the first flexural crack, cracking occurs at other locations as the applied load increases. The occurrence of these cracks in concrete is associated with drops observed in the load response. The final failure predicted by the finite element analysis is due to the rupture of the FRP at a location close to the midspan of the beam. This agrees with the experimental observation of Wu et al. (1998).

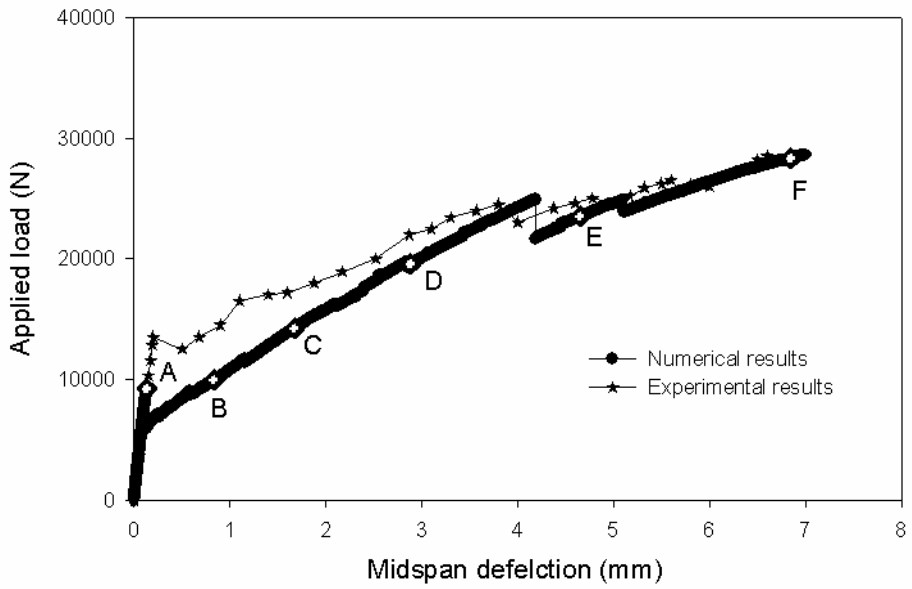

Figure 6.6: Comparison between experimental and numerical load responses of beam 1

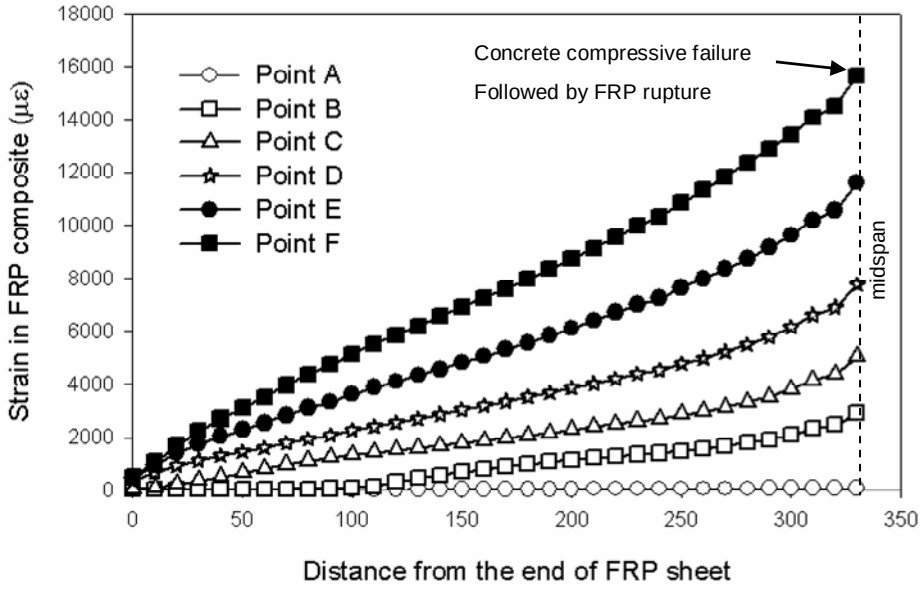

Figure 6.7: Strain distribution in the FRP composite corresponding to different points in the load response of beam 1

Figure 6.7 shows the strain distributions along the length of the FRP sheet at points A, B, C, D, E and F of the load response. It is clearly seen from Figure 6.7 that at any load level the strain in the FRP increases monotonically from the free edge to the midspan. Further, as the load increases the stress distribution keeps increasing up to

failure. The continued increase in the axial strains at all points along the length of the FRP up to failure suggests active stress transfer from the concrete substrate. This implies that the interfacial fracture parameters are high enough to prevent debonding up to failure of the beam. This fact agrees well with the experimental observation of Wu et al. (1998).

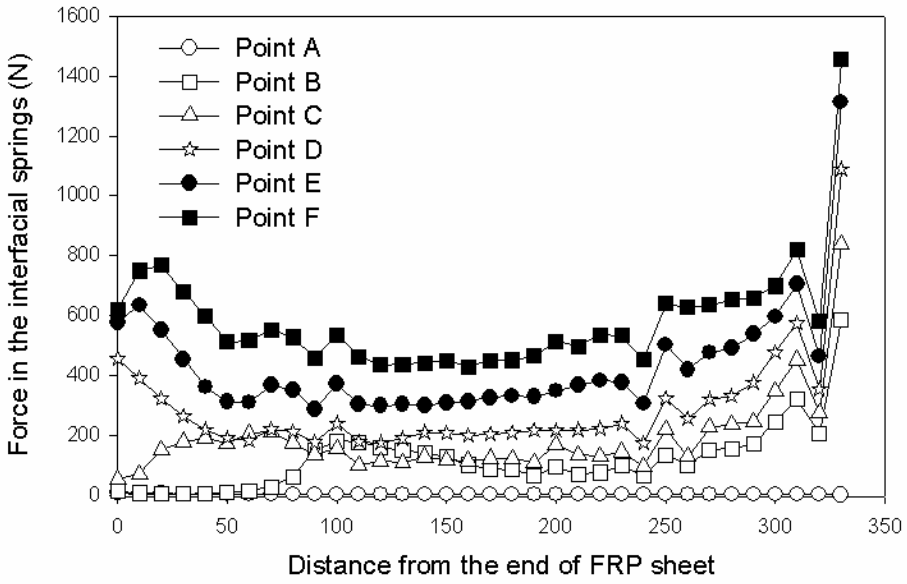

Figure 6.8: Forces in the nonlinear springs that modeled the FRP-concrete interface of beam 1

Figure 6.8 shows the force in the interfacial springs as a function of location along the FRP-concrete bonded length at different points of the load response. It is clearly seen that at Point A of the load response the force in the interfacial springs is approximately constant at a very small value along the length of the FRP. After the formation of flexural cracks in the concrete, the interfacial springs close to midspan register higher forces clearly showing the effect of the stress concentrations near the crack. The stress concentration at the free end of the FRP also results in an increase in the interfacial spring forces close to the supports. The variation in the interfacial spring forces along the length of the FRP can be broadly classified into three distinct regions

each associated with a specific load action or effect: (a) a region with a rapid change in the spring force per unit length produced by the stress concentrations associated with the flexural crack; (b) a region where the interface spring force is approximately constant in the middle third of the length of the FRP. The interfacial spring forces in this region are due to bending and are not affected by stress concentrations; and (c) a region with a gradient in the spring forces close to edge of the FRP in the last third of the bonded length.

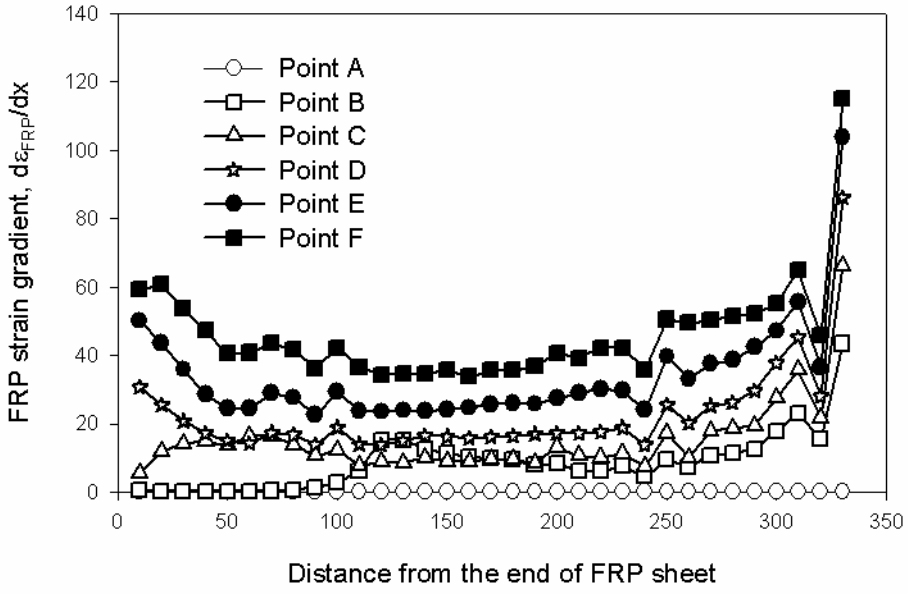

Figure 6.9: FRP axial strain gradient versus location along the bonded length of beam 1

Figure 6.9 shows the axial strain gradient in the FRP along the bonded length. It can be seen that the strain gradient distribution pattern is similar in shape to that of the spring forces of Figure 6.8.

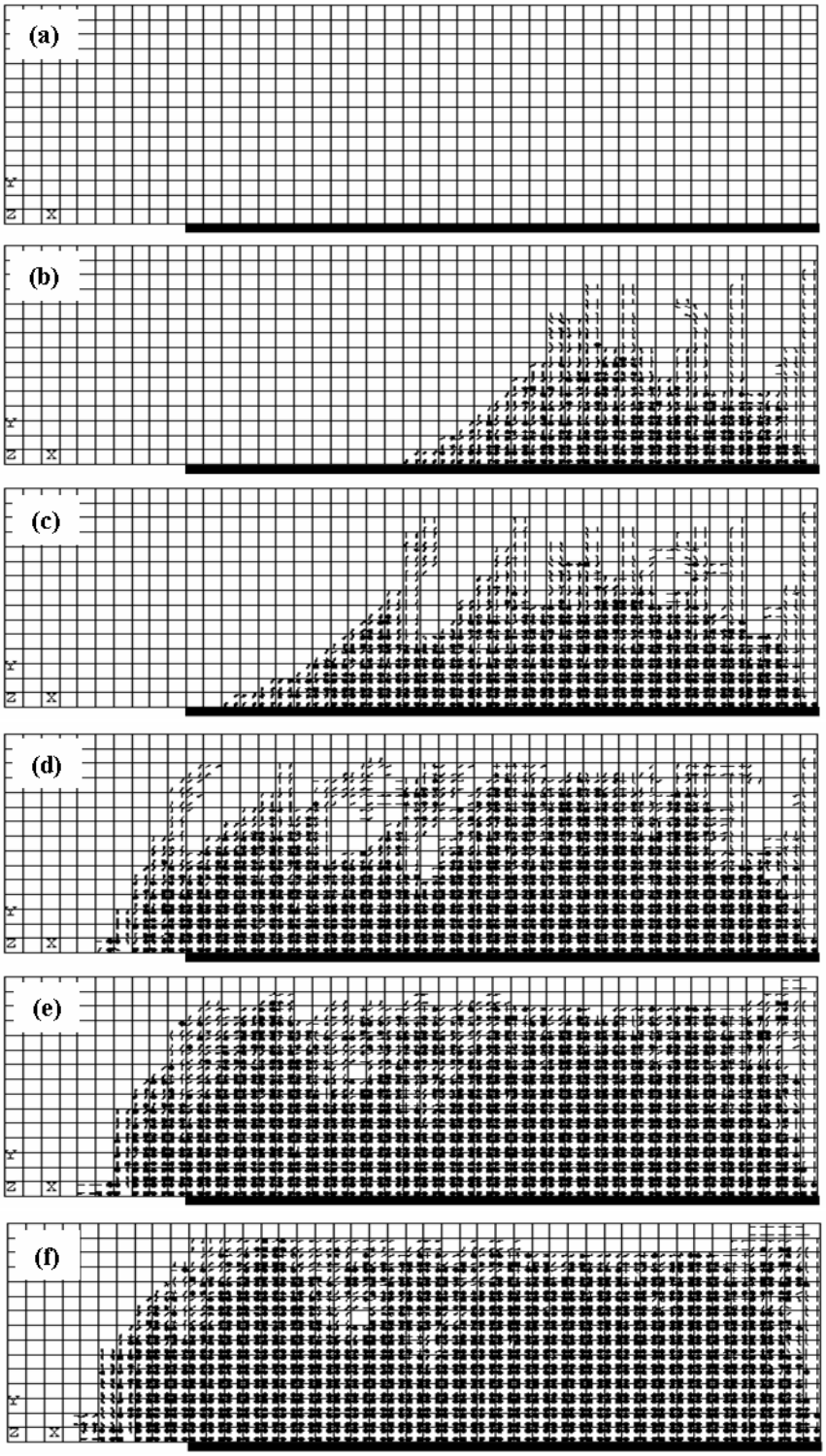

Figure 6.10: Cracking distribution at different points of the load response of beam 1

The crack patterns in concrete at different points of the load response are shown in Figure 6.10. As mentioned in the previous section, Point A is located in the linear elastic range and therefore no cracking is yet present in concrete. The crack pattern after initiation of flexural cracking in the concrete at Point B of the load response is shown in Figure 6.10b. It is clearly seen that the cracks are almost vertical close to midspan while those away from midspan and close to the neutral axis are inclined at 45^o. With increasing load, cracking spreads out towards the supports. In the crack pattern corresponding to Point C of the load response, the flexural and diagonal shear cracks can be clearly delineated. At Point D, both the flexural and diagonal tension cracking regions start to expand. At Points E and F, it is clearly seen that most of the concrete in tension has already cracked and also the stress in some fibers in the upper concrete at midspan reaches the maximum compressive strength $f_c^{'}$.

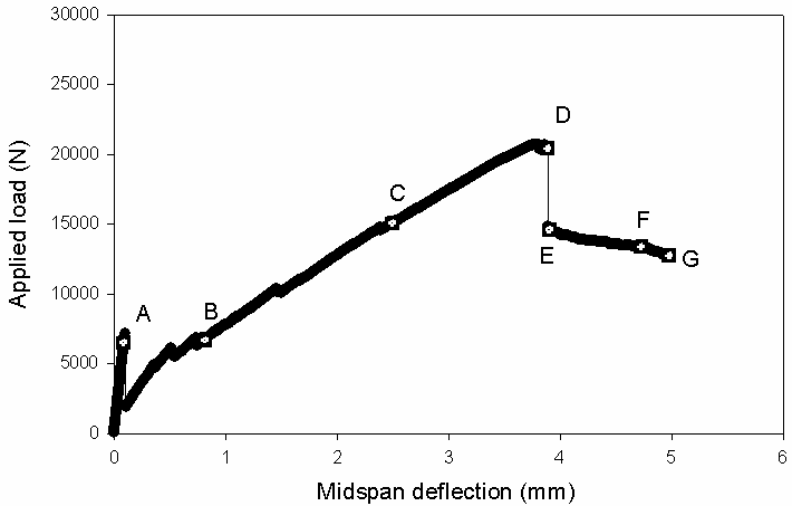

Figure 6.11: Applied load versus midspan deflection of beam 2

6.5.2 Results of beam 2

The load versus deflection response of beam 2 obtained from the finite element analysis is shown in Figure 6.11. The load initially increases linearly with deflection up

to the point where the first flexural crack occurs in the bottom concrete fibers. This corresponds with a drop in load due to a decrease in the flexural stiffness at the cracked section. After first crack, the load becomes nonlinear and increases up to Point D. This increase in the load in the nonlinear region of the response is associated with cracking at other locations along the span of the beam. Interfacial debonding initiates at Point C of the load response where the interfacial spring at midspan exhibits softening. As the load increases, more interfacial springs start to soften until the load reaches Point D. After Point D, there is a sudden drop in the load at a constant deflection. A stable continuous equilibrium path could not be established between Points D and E resulting in a sudden load drop. At Point E, stable equilibrium could only be established at the same deflection as Point D with a significant increase in the interfacial crack length. After this sudden unstable crack growth, which results in a load drop, the softening behavior of the load response is associated with progressive debonding as it is explained in more detail in the coming section.

Figure 6.12 shows the strain distributions along the length of the FRP at points A, B, C, D, E, F and G of the load response of beam 2. At Point A the strains in the FRP is relatively constant at small value. As the load increases, the strain distribution keeps increasing up to Point D where the strains in the FRP reach a maximum value at midspan approximately equal to 10500 με. The stress concentration close to the flexural crack is clearly seen at Points B, C and D. The unstable load drop from Point D to Point E is associated with a drop in the axial strain at midspan. At Point E, the axial strain in the FRP levels off at approximately 6500 με for a distance of 150mm from midspan. With continued loading, a larger portion of the FRP shows a constant strain. The strain

distributions at Points E, F and G are similar to those obtained during progressive debonding from a direct shear test.

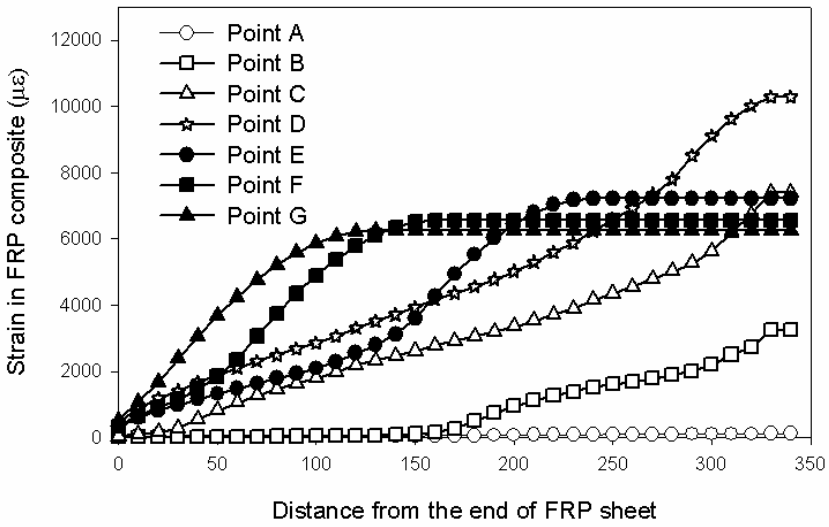

Figure 6.12: Strain distribution in the FRP composite corresponding to different points in the load response of beam 2

Figure 6.13 shows the forces in the interfacial springs at different points of the load response. It is clearly seen that at Point A the forces in the springs are relatively constant along the length of the beam. As cracking starts to form in concrete, the interfacial springs close to midspan start to register higher forces due to the shear stress concentration at the flexural crack. It can be noticed that the forces in the interfacial springs close to the flexural crack increase very rapidly due to shear stress concentration while those away from the crack show constant values associated with flexure. At Point D, the relative displacements in four interfacial springs closest to midspan exceed s_o and therefore exhibit softening. Just after the unstable drop in the load, the relative displacement in nine interfacial springs exceeded s_f indicating no stress transfer through these springs. Therefore, it can be concluded that the drop in the load, from Point D to E,

is associated with a sudden interfacial crack growth that results in a fully debonded portion of FRP approximately equal to 90 mm in length. The spring forces corresponding to Points E, F and G of the load response clearly indicate that the interfacial crack propagates towards the supports. Therefore, the progressive debonding is associated with a decrease in the applied load.

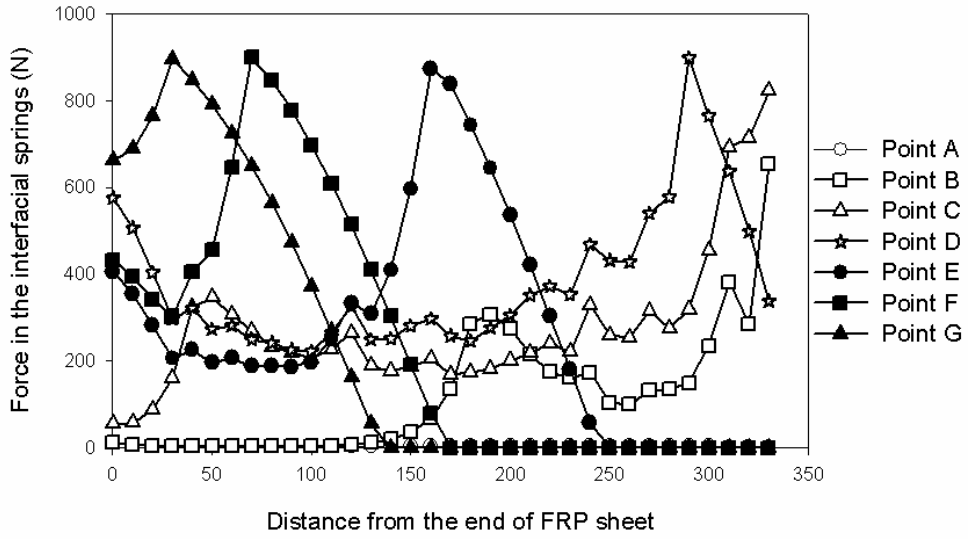

Figure 6.13: Forces in the nonlinear springs that modeled the FRP-concrete interface of beam 2

The FRP strains and interfacial spring forces indicate that the portion of the load response between Points E and G is associated with progressive debonding of the FRP. It can be noticed that after debonding initiates at Point C, the strain in the FRP continues to increase up to Point D. This implies that the strain in the FRP cannot be used as debonding initiation criterion as implied in the ACI recommendations. On the other hand, the previous chapters of this report have demonstrated how the fracture material law can be derived from the measured strain gradient. For this reason, the FRP strain gradient versus location along the length of the FRP is plotted as shown in Figure 6.14 to come up with a criterion that combines both initiation of debonding and ultimate failure.

There is a similarity in shape and pattern between Figure 6.13 and Figure 6.14. This implies that the debonding criterion should be based on the FRP axial strain and its gradient and not only on the critical value of strain as will be explained in greater detail in the following sections.

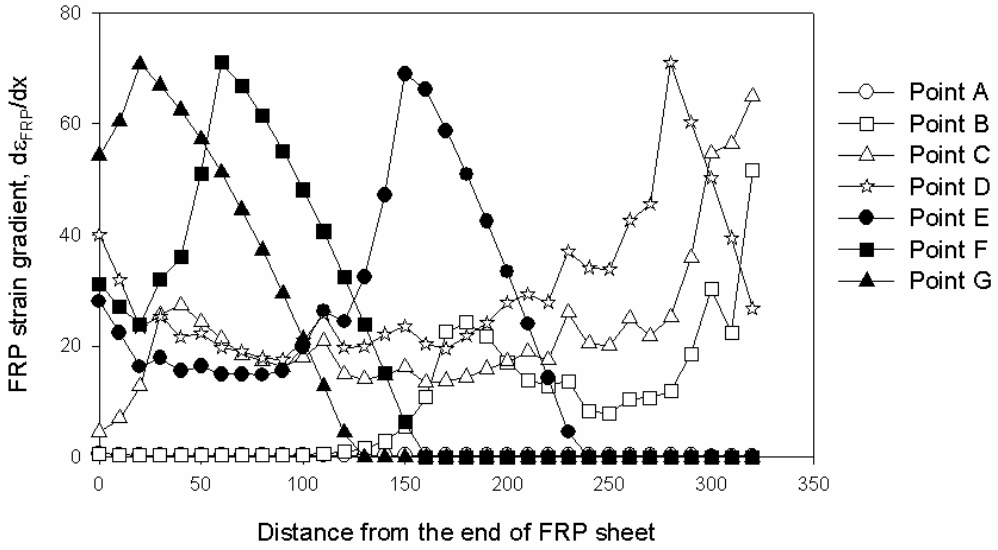

Figure 6.14: FRP axial strain gradient versus location along the bonded length of beam 2

Figure 6.15 shows the crack pattern in the concrete beam at different points of the load response. There is no cracking in concrete when the load is still in the linear elastic range. After Point A, the load drops due to the initiation of a flexural crack close to midspan. Points B and C are in the nonlinear potion of the load response. With continued loading, flexural cracks continue to form and diagonal shear cracks start to spread towards the support. In this analysis, an interfacial notch was introduced in the FRP-concrete interface and extended under two concrete elements. The effect of this notch is very noticeable in the crack pattern of the first two columns of concrete elements close to midspan where no cracking is present. The unstable drop from Point D to Point E is associated with an interfacial crack growth. After Point E, the softening

behavior in the load response is associated with progressive debonding in the FRP-concrete interface. It is clearly seen that the concrete in tension has mostly cracked while the compressive stresses in the concrete close to midspan are smaller than $f_c^{'}$. By comparing the crack patterns in beams 1 and 2, it can be noticed that the crack distribution is spread over a larger region in beam 1 due to the fact that the interfacial parameters are relatively higher and therefore provided a stronger strengthening system. Also the failure mode of beam 2 is due to the complete debonding of the FRP from the concrete rather than reaching the concrete compressive failure followed by FRP rupture as observed in beam 1.

A flexural crack of 40 mm was introduced at midspan of beam 2 and the previous analysis was repeated on the pre-cracked beam. The load responses of the pre-cracked and un-cracked beams are shown in Figure 6.16. It is clearly seen that the maximum applied load for the pre-cracked beam occurs at lower value when compared to the un-cracked beam. After the first flexural crack forms, the responses of both beams are similar in shape up to the peak of the pre-cracked beam. After the peak, a slight drop in the load is observed which is smaller and more gradual than that observed in the pristine beam. This implies that the pre-cracked load response is more stable at the point where the first interfacial spring exceeds s_f.

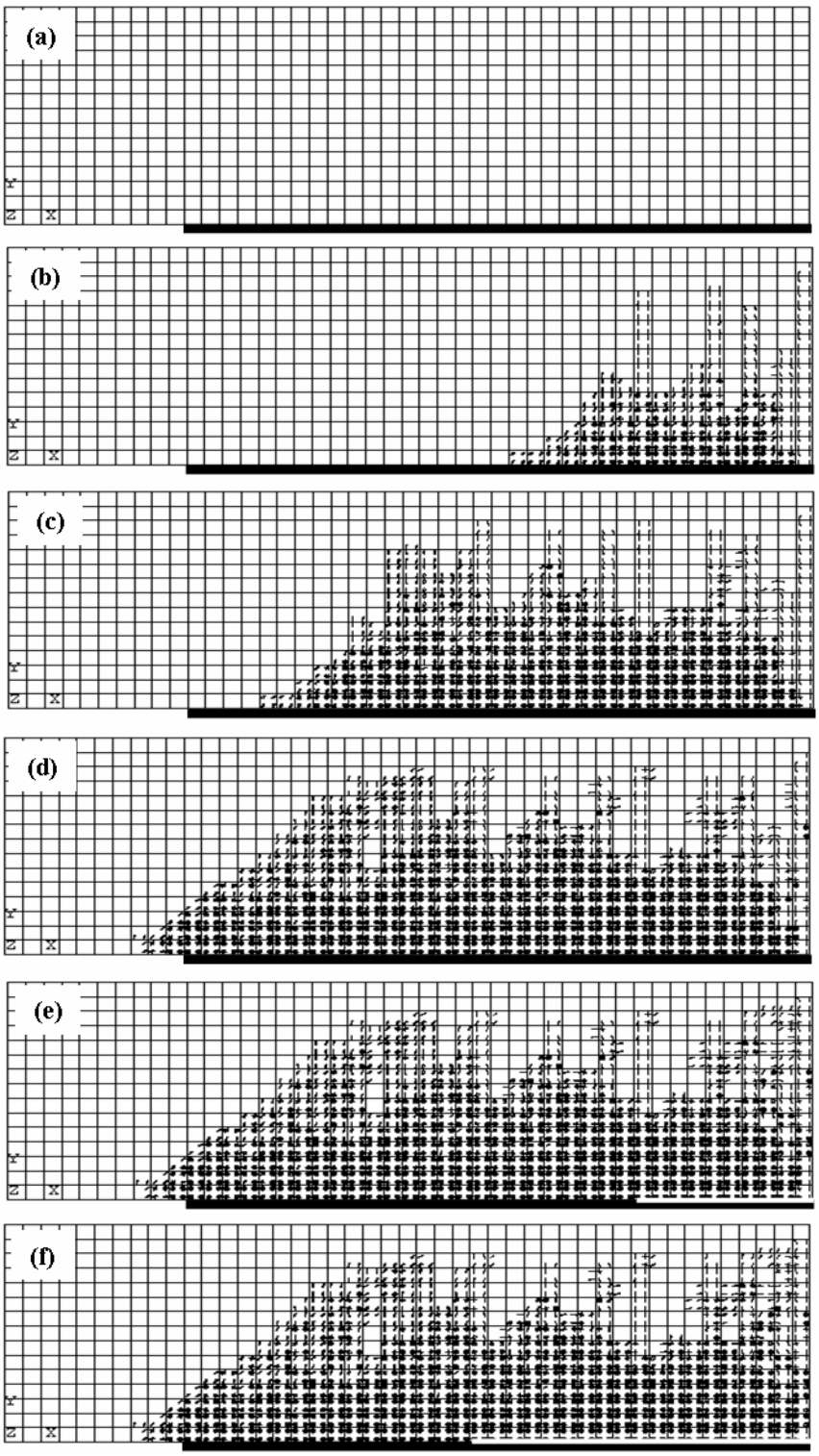

Figure 6.15: Cracking distribution at different points of the load response of beam 2

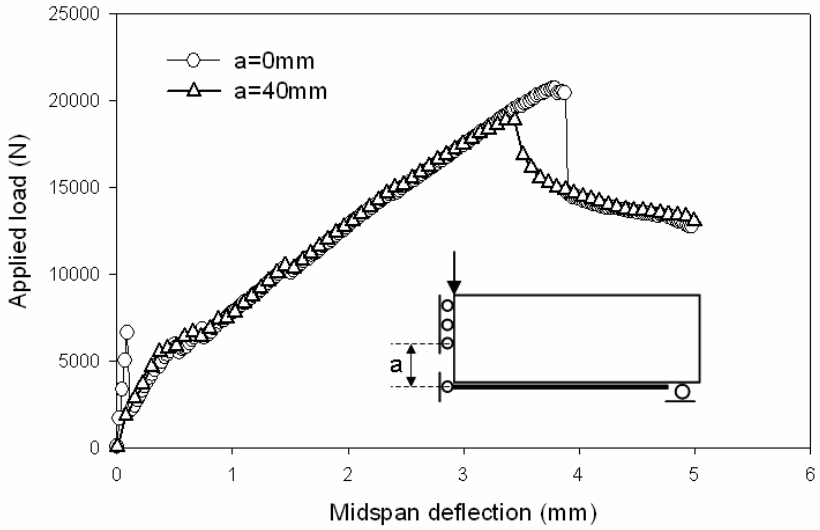

Figure 6.16: Comparison between the load responses of pre-cracked and un-cracked beams

6.6 Sectional analysis

All conventional design procedures for FRP-strengthened beams are based on sectional analysis. This section presents an analytical model to determine whether the sectional analysis provides a reasonable approach. In this analysis, the following assumptions are made: (a) small deformations; (b) linear strain distribution throughout the depth of the beam; (c) shear deformation is negligible; and (d) perfect bond between concrete and FRP (i.e. no relative slip between the concrete and FRP). The nonlinear stress-strain relation of concrete in compression used in the analysis is shown in Figure 6.17. The concrete is assumed to be linear elastic up to the tensile strength after which it exhibits a softening behavior. Sectional analysis based procedure, which do not consider the debonding mode of failure, overestimate the moment capacity in beams, which fail by debonding. For this reason, ACI and other codes have recommended to use a maximum strain limit in the FRP as an additional criterion to avoid the initiation of debonding.

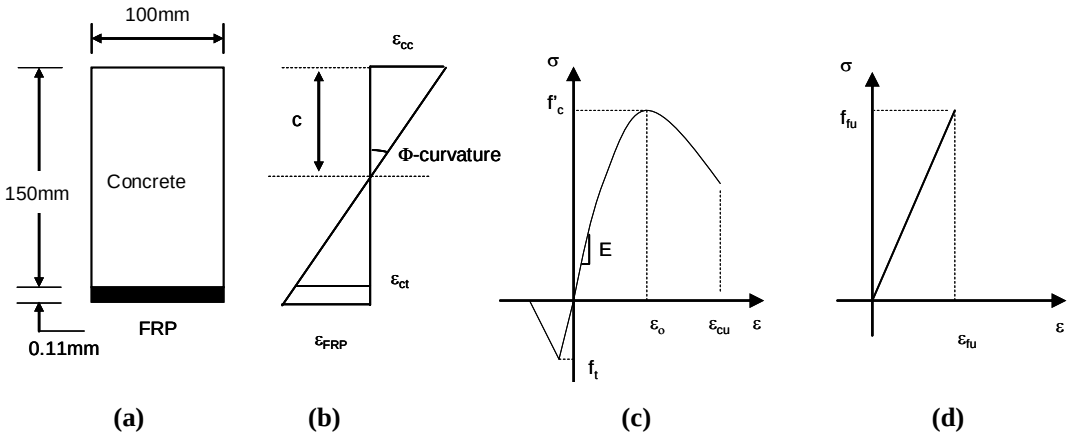

Figure 6.17: The analyzed cross section using strain compatibility method: (a) beam's cross sectional area; (b) strain diagram; (c) stress-strain relationship of concrete; and (d) stress-strain relationship of FRP composite

For implementing the sectional analysis based procedure, the first step requires establishing the moment curvature (M-Φ) relationship for the beam cross section. The (M-Φ) curve for a given cross section is generated such that for any given applied moment the following conditions of equilibrium are satisfied: (a) the internal forces sum to zero; (b) the resultant of internal moment is equal to the externally applied moment. Once the equilibrium is satisfied, the strains in the materials and hence the curvature can be determined. The procedure adopted for determining M-Φ relationship for the given beam cross section comprised of determining the equilibrium moment for a given concrete strain, ε_{cc}^{i}. For each ε_{cc}^{i}, the curvature of the section is determined as the ratio of the strain at the extreme fiber to the depth of the neutral axis, c_i.

$$\phi_i = \frac{\varepsilon_{cc}^{i}}{c_i} \tag{6.7}$$

$$\varepsilon_{FRP}^{i} = \phi_i \times (h - c_i) \tag{6.8}$$

Once equilibrium is satisfied, the internal bending moment M_i and the strain in the FRP are calculated. This process is continued until the strain in the concrete reaches its ultimate value.

6.7 Comparison of finite element analysis to sectional analysis

6.7.1 FRP strain distributions for beam without debonding

The strain distributions and strain gradients along the length of the FRP are determined from two different methods and compared in this section. The results obtained from the finite element analysis are compared with the results obtained from sectional analysis. The tensile strength of concrete is accounted for in both methods.

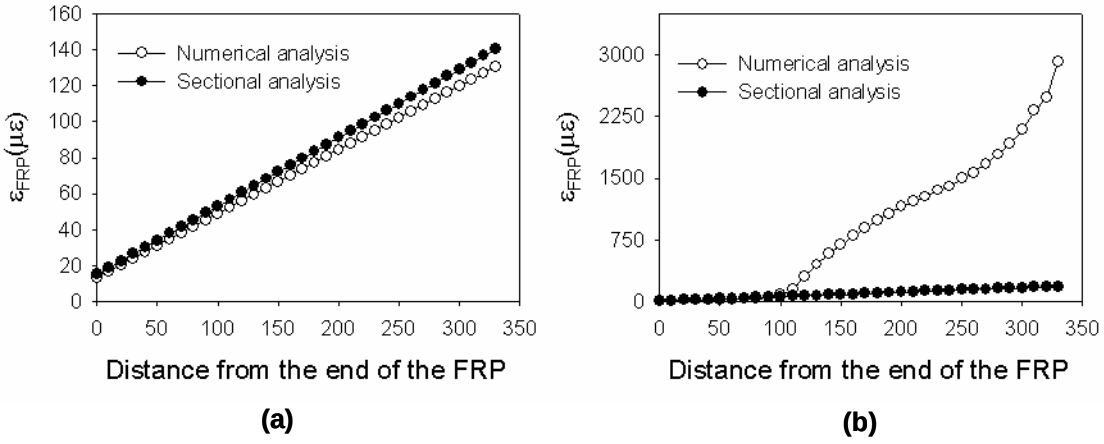

Figure 6.18: Strain distributions obtained numerically and from sectional analyses performed on beam 1: (a) at point A; and (b) at point B

Figure 6.18 shows the strain distributions along the length of the FRP at Point A and B of the load response of beam 1. In Figure 6.18a, it is clearly seen that the strains in the FRP obtained from sectional analysis and the numerical analysis are reasonably close. Figure 6.18b shows the strain distribution along the FRP that corresponds to Point B of the load response where a flexural crack forms close to midspan. The strains

obtained numerically start to deviate from the strains obtained from sectional analysis as we move towards the midspan. The reason for this difference in the strains is due to the fact that sectional analysis cannot predict the stress concentrations close to the flexural crack.

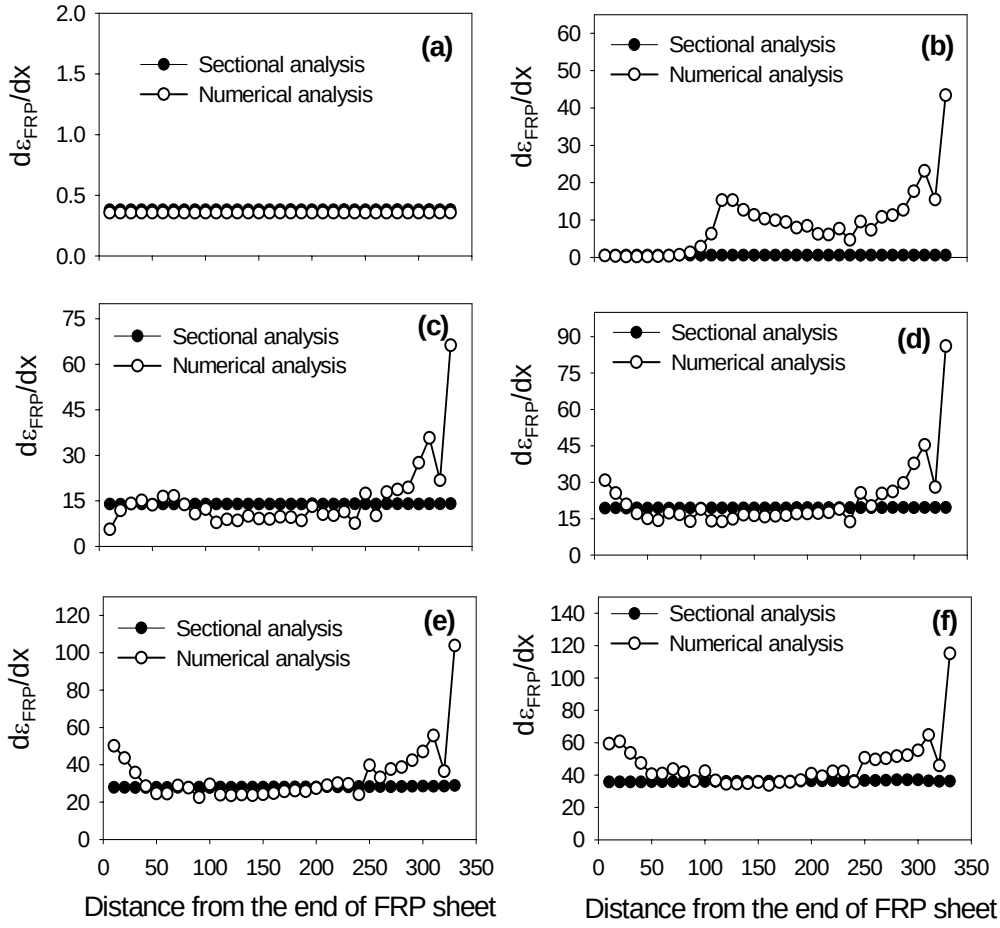

Figure 6.19: Strain gradients obtained numerically and from sectional analyses performed on beam 1: (a) at point A; (b) at point B; (c) at point C; (d) at point D; (e) at point E; and (f) at point F

The strain gradients versus location along the length of the FRP are shown in Figure 6.19. It is clearly seen that the strain gradients obtained from both methods match well in the region away from the edges, i.e. the match is reasonably good in the regions where there are no stress concentrations. Figure 6.19a implies that the strain gradients

from both methods are identical in the linear elastic range. As flexural cracks start to form, the strain gradients obtained from the sectional analysis start to deviate from those obtained numerically in the region of high interfacial stress concentration close to the flexural crack. The strain gradient predicted using sectional analysis is only due to the curvature effect and does not include the stress concentration close to flexural crack. It is also noted that even when debonding is not the mode of failure, the strain gradient obtained from the two methods do not match along the full bonded length.

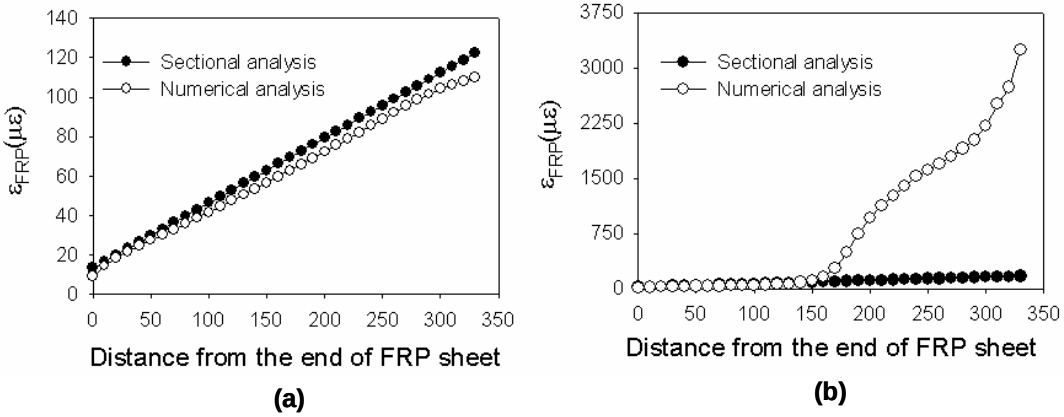

Figure 6.20: Strain distributions obtained numerically and from sectional analyses performed on beam 2: (a) at point A; and (b) at point B

6.7.2 FRP strain distributions for the beam that exhibits debonding

The strain distributions corresponding to points A and B of the load response of beam 2 are shown in Figure 6.20. As described in the previous sections, Point A corresponds to a point chosen in the linear part of the load response. Figure 6.20b shows the strain distributions corresponding to Point B after the concrete close to midspan starts to crack. It is clearly seen that the strains from both methods match very well in the linear part of the load response as shown in Figure 6.20a. The strain distributions obtained numerically match the strains obtained from sectional analysis in the region

away from midspan as shown in Figure 6.20b. The difference in the strains becomes more evident as we approach the midspan where the interfacial strain concentration is the predominant component of the strains and not the strains due to curvature.

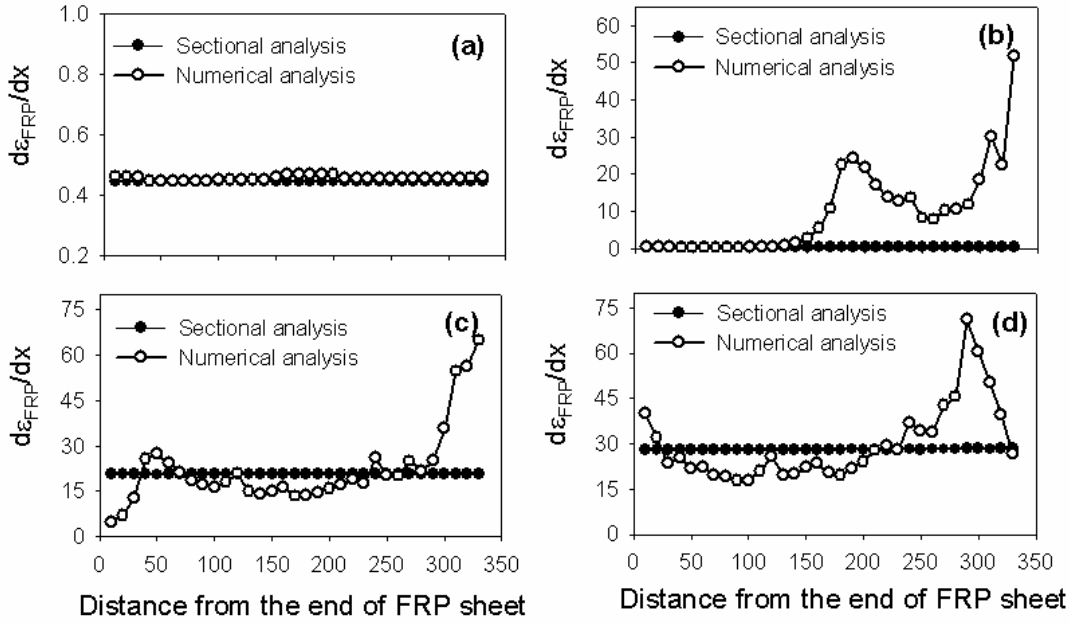

Figure 6.21: Strain gradients obtained numerically and from sectional analyses performed on beam 2: (a) at point A; (b) at point B; (c) at point C; and (d) at point D

The strain gradients along the length of the FRP at load corresponding to Points A, B, C and D of the load response of beam 2 are shown in Figure 6.21. Figure 6.21a shows no significant difference in the gradients obtained from both methods. The strain gradients consist of two components: (a) gradient due to curvature which is accounted for in both methods; and (b) gradient due to the stress concentration which is accounted for only in the numerical analysis. It is clearly seen that the strain gradient predicted using sectional analysis is lower than that obtained from the numerical analysis in the stress transfer region.

6.7.3 Ultimate load and initiation of debonding

The ultimate loads for both beams presented earlier are determined from two different methods and compared in this section. The procedure for determining the ultimate load as recommended by ACI committee (ACI 440.2R-02) is based on sectional analysis where the axial strain in the FRP is limited to an allowable value to account for the potential of debonding and delamination failures of externally bonded systems. The allowable strain is given as

$$\varepsilon_{fub} = \kappa_m \varepsilon_{fu} \tag{6.9}$$

where ε_{fu} is the FRP design rupture strain and is equal to 0.017. The value of κ_m is given as (ACI 440.2R-02)

$$\kappa_m = \begin{cases} \dfrac{1}{60\varepsilon_{fu}}\left(1 - \dfrac{nE_f t_f}{360{,}000}\right) \le 0.90 \quad for\ nE_f t_f \le 180{,}000\ \text{N/mm} \\ \dfrac{1}{60\varepsilon_{fu}}\left(\dfrac{90{,}000}{nE_f t_f}\right) \le 0.90 \quad for\ nE_f t_f > 180{,}000\ \text{N/mm} \end{cases} \tag{6.10}$$

where n, E_f and t_f are the number of FRP plies, the tensile modulus and the nominal ply thickness of FRP, respectively. The values of n, E_f and t_f used in this analysis are equal to 1, 230GPa and 0.11mm, respectively. It is important to note that Equation 6.9 does not include the effect of existing internal longitudinal or transverse steel, concrete strength, the properties of the adhesive layer bonding the FRP to the concrete or the width of the FRP laminate relative to the concrete width (ACI 440.2R-02).

Table 6.2 summarizes the compiled results of the ultimate loads obtained from the sectional analysis (as per ACI 440.2R-02) and the numerical analysis presented earlier in this chapter. It can be noticed that the ultimate loads for both beams 1 and 2 are considerably overestimated using the sectional analysis method recommended by the

ACI committee 440. The reason for this difference is due to the fact the recommendations made by ACI do not account for the interfacial material properties, the concrete strength and the width of the FRP. It can be noticed from this comparison that the strain-based approach with sectional analysis is not a conservative approach. The ultimate load obtained from sectional analysis is higher than the load obtained experimentally and from finite element analysis. From this comparison, it is also obvious that by keeping the material properties of concrete the same and increasing the fracture toughness and the tensile strength of concrete, the mode of failure changes as observed from the finite element analysis. However, the mode of failure remained unchanged in both beams when using the ACI approach.

Table 6.2: Compiled results from sectional analysis and FE analysis

	Sectional analysis as per ACI 440.2R-02			FEM		
	k_m	P_u(N)	Mode of failure	P_{init}(N)	P_u(N)	Mode of failure
Beam 1	0.9	30800	Debonding	---	28500	Compressive concrete failure
Beam 2	0.9		Debonding	15500	21000	Debonding

6.8 Discussion

In shear strengthening applications, the FRP sheets are attached to the side of the concrete beam. The stresses are transferred from concrete to the FRP through the interfacial bond. In this case, the failure criterion of the strengthening system can be based on the maximum strain obtained from the direct shear tests presented in Chapter 3 where bending effect is not present. In other words, interfacial debonding only occurs when the value of the axial strain in the FRP reaches a maximum value.

In flexural strengthening applications, the FRP sheets are attached to the tension side of the beam. In this case, the initiation of debonding is caused by the combination of curvature and stress concentration close to a flexural crack in the concrete. Comparisons of the strains in the FRP predicted by sectional analysis and by finite element analysis show that the strains associated with curvature change are significantly smaller than those due to stress concentrations. Therefore, a strain based criterion for debonding obtained from sectional analysis as recommended by ACI cannot be used to predict debonding.

The analysis performed in this chapter indicates that interfacial debonding is initiated in the beam when the interfacial slip at the material element closest to the flexural crack exceeds s_o. Any increase in slip past s_o results in a softening response from the interface material element. s_o is a material property that depends only on the two adherents and is independent of geometry and loading configuration. Therefore, any rational design procedure which accounts for debonding should be based on the interfacial slip at the face of an existing flexural crack. However, interfacial slip cannot be determined or measured directly in beams but can be assessed from the strain gradients in the FRP as verified in Chapter 3 of this report. When the interfacial slip equals s_o, the interfacial shear stress is equal to τ_{max}, which is the maximum stress in the interfacial material law. Therefore, when the interface slip equals to s_o, the shear stress in the FRP at that location reaches its ultimate value. Therefore, the initiation of debonding should be based on a critical value of strain gradients in the FRP and not a critical value of the strain as recommended by ACI. The critical value of strain gradient

for initiation of debonding can be obtained from direct shear tests as demonstrated in Chapter 3.

6.9 Conclusions

In this chapter, the behavior of concrete beams strengthened using externally attached FRP sheets is analyzed. Based on the results presented in this chapter, the following conclusions can be drawn:

1) The mode II crack propagation (shear cracking mode) is the predominant component when debonding is initiated close to the midspan of concrete beams externally strengthened by FRP sheets.

2) If the FRP-concrete interfacial crack forms at midspan, it propagates towards the support. A stable interfacial crack growth is associated with increasing load up to a critical crack length after which the load response shows softening.

3) Initiation of debonding and ultimate failure should be based on the critical strain in the FRP as well as the strain gradients.

4) A comparison between the strain-based ACI approach and the finite element analysis performed for two beams that have different interfacial fracture toughness revealed that the strain-based failure criterion obtained from the conventional sectional analysis method is not a safe criterion.

CHAPTER 7

CONCLUSIONS AND RECOMMENDATIONS

7.1 Summary

A review of the-state-of-the-art in the applications of FRP for strengthening concrete structures concluded that the state of practice relies on conventional mechanics of materials based approaches to predict the load-deflection response of FRP strengthened beams. A review of the literature also revealed that in flexural strengthening, sectional analysis did not allow for modeling the debonding phenomenon, which was the most observed failure mechanism. Information required to establish appropriate material law that model the debonding in the FRP-concrete interface was not available. Furthermore, the impact of freeze-thaw on the bond between FRP and concrete was not completely understood and the results in the literature were often contradictory. For these reasons, this study embarked on a comprehensive review of the behavior of the interfacial bond between the concrete and FRP sheets which combined experimental investigation of the FRP-concrete bond and the development of appropriate numerical models.

The experimental program studied the fracture behavior of the FRP-concrete interfacial bond using an optical technique known as digital image correlation (DIC). The following conclusions were drawn from the experimental results: (a) the progressive debonding of the FRP is produced by a crack, which forms and propagates along the interface between the concrete and the FRP; (b) the load versus global slip response of the FRP-concrete bond can be divided into pre and post-peak parts; (c) the crack initiates in the pre-peak part of the load response; (d) once the crack initiates at the interface, it propagates in a self-similar manner at a constant load in the post-peak part of the load response. This steady crack growth is responsible for a constant increase in the global slip of the FRP; (e) in the post-peak part of the load response, where the crack propagates, there is a constant stress transfer length between the concrete and the FRP composite sheets, which was found to be approximately equal to 90 mm. The stress transfer zone advances along the bonded length of FRP as the crack propagates; (f) the fracture energy, which is the energy required for a cracking zone to increase by a one unit area, was found to be constant and independent of the location of the crack along the interface; (g) good agreement was obtained between the fracture energy calculated from direct shear tests with that obtained from cyclic tests; (h) the quasi-static monotonic load response acts like an envelope for the quasi-static cyclic response. Cycling the load to and from the quasi-static load envelope does not change the stress distribution in the stress transfer zone. Repeated cycling from and to the load envelope produces a change in the global compliance of the specimen associated with crack propagation; and (i) using the digital image correlation (DIC) system allowed for the mapping of the complete strain field, which resulted in an accurate estimation of the

interfacial fracture parameters as represented by the material law and the fracture energy release rate.

The influence of freeze-thaw cycling on the interfacial debonding and the stress transfer between the concrete and the FRP was also investigated. A statistical analysis was performed to evaluate the significance of the decrease in the fracture parameters. Based on the freeze-thaw results, the following conclusions were drawn: (a) a slight decrease in the initial stiffness and an extended non-linear zone prior to the peak load is observed in direct-shear response of the specimens subjected to freeze-thaw when compared with the control specimens; (b) there is no decrease in the elastic modulus of the FRP composite with freeze-thaw cycling; (c) there is a progressive decrease in the load carrying capacity in the specimens subjected to freeze-thaw cycles when compared with the control specimens. In freeze-thawed specimens, the progressive debonding in the post peak load response occurs at a lower load than that of the control; (d) in the post-peak part of the load response, there is a constant stress transfer length between the concrete and the FRP sheets for all specimens. The strain distribution in the stress transfer zone of the freeze-thaw damaged specimen has the same shape as that observed in the control specimen. However, there is a statistically significant decrease in the length of the stress transfer zone and the strain in the FRP at full debonding with an increase in the number of freeze-thaw cycles; (e) the nonlinear material law of the FRP-concrete interface for specimens subjected to freeze-thaw cycling is found to be similar in shape when compared with that obtained from the control specimens. However, there is a statistically significant decrease in the parameters describing the material law as the number of freeze-thaw cycles is increased; (f) although the failure in all specimens

tested is found to be due to debonding of FRP from the concrete substrate along the interface, there is a slight, yet noticeable change in the failure mode due to freeze-thaw cycling. The failure occurs close to the FRP sheet for the freeze-thawed specimens; and (g) the results of the statistical analysis indicate that there is a significant drop in the interfacial fracture energy with freeze-thaw cycling. The results suggest a progressive change with freeze-thaw cycling indicating continuous accrual of freeze-thaw damage in the interface.

A numerical model was developed to study the instability in FRP-concrete interface for beams strengthening applications. Based on the results of the numerical analysis, the following conclusions were drawn: (a) shear debonding between FRP and the concrete substrate can be adequately modeled using an experimentally derived material law for the interface, which exhibits softening behavior; (b) the arc-length method provides a means to numerically analyze the full behavior of debonding at the FRP-concrete interface; (c) the results of the numerical analysis demonstrate that the shear failure of the FRP-concrete bond from concrete may lead to snap-back instability; (d) the results of the numerical analysis confirm the presence of a critical length that is responsible for transferring the stresses between concrete and the FRP composite sheets. However, using a bonded length greater than the critical length does not improve the ultimate capacity of the bond; (e) the observed snap-back in the load response depends upon the bonded length of the FRP. It is shown that the short bonded lengths do not exhibit snap-back, while the intensity of the snapback increases with an increase in the bonded length beyond 85mm; (f) the progressive shear debonding at the FRP-concrete interface may produce a sudden release of energy associated with the snapback

mechanism resulting in catastrophic failure; (g) the randomness in the fracture parameters does not significantly affect the overall load response of concrete externally strengthened with FRP; and (h) the higher the fracture energy the better load carrying capacity of the bond. Any change in the fracture parameters, τ_{max}, s_o and s_f with a constant G_F will not affect the load carrying capacity and the maximum strain in the FRP. The load carrying capacity is increased with the increase on the FRP axial stiffness.

A nonlinear finite element model is used to study the behavior of concrete beams strengthened using externally attached FRP sheets. The analysis led to the following conclusions: (a) the mode II crack propagation is the predominant component when debonding is initiated close to the midspan of FRP sheets strengthened beams; (b) if the FRP-concrete interfacial crack forms at midspan, it propagates towards the support. A stable interfacial crack growth is associated with increasing load up to a critical crack length after which the load response shows softening; (c) initiation of debonding and ultimate failure should be based on the critical strain in the FRP as well as the strain gradients; and (d) the comparison between the strain-based approach recommended by ACI and the finite element analysis performed in the two beams that have different interfacial fracture toughness revealed that the strain-based failure criterion obtained from the conventional sectional analysis method is not a safe criterion. More advanced criteria based on strain-gradients should be developed to control the debonding of FRP sheets from concrete beams.

7.2 Contributions

The main contributions of this dissertation to the state of the art on the application of the FRP for externally strengthening concrete flexural beams are summarized below:

(a) The cohesive material law that can be used in any numerical simulation involving shear stress transfer across the concrete-FRP interface was experimentally determined. An understanding of the effect of freeze-thaw cycles on the fracture parameters of the material law was also developed. The nonlinear material law was used to explain the scaling in the direct shear load response of FRP sheets bonded to concrete.

(b) An understanding of the instability at ultimate failure in shear debonding response was developed. The reason for instability was shown to be the result of snapback mechanism. The observed unstable failure at complete debonding in FRP-strengthened concrete beams was explained.

(c) The conventional sectional strain-based analysis (recommended by ACI committee 440) was shown to be unsafe. A new criterion for initiation of debonding based on the strain gradient in the FRP was proposed.

7.3 Future research work

The results of the freeze-thaw tests performed in this study show a statistical significant reduction in the bond properties however, additional experimental testing is still needed in order to develop a degradation model that simulates the effect of environmental conditions due to freeze-thawing as well as other effects.

This study focused on the behavior of the bond under the effect of increasing loads. The behavior of the bond under cyclic loading has not been addressed in the

literature. Therefore, experimental investigations to study the fatigue behavior of FRP bonded to concrete should be performed to establish appropriate fatigue crack propagation models.

The considerable scatter in the response of specimens tested in this study and by other researchers suggests that future design recommendations must take into considerations the uncertainties associated with determining the random material properties and other sources of uncertainties using structural reliability methods.

The Finite Element analysis performed in this study emphasized the behavior of the bond and did not consider other possible modes of failures. Hence, future numerical simulation studies should be expanded to include more advanced models for the concrete substrate and to take into consideration the friction that may take place between the FRP and the concrete as debonding progresses.

Improve the nonlinear finite element analysis presented in Chapter 6 to be able capture the snapback mechanism at ultimate failure observed in the strengthened beams by adapting methods similar to the arc-length method used in Chapter 5 of this report. This would allow for a more complete representation of the full behavior of the system from the initial stages of loading until the complete collapse of the structure.

APPENDIX I

NOTATION

c	=	acceptance interval for the significance testing;
d	=	global slip;
s	=	interfacial relative slip;
s_o	=	interfacial relative slip corresponding to maximum shear stress;
s_f	=	horizontal intercept of the linear softening curve;
t	=	thickness of the fibers contained in the FRP composite;
E	=	elastic modulus of the FRP composite;
y	=	coordinate from the unloaded end of the FRP;
G_F	=	interfacial fracture energy;
H_o	=	null hypothesis for the significance testing;
H_1	=	alternate hypothesis for the significance testing;
L_{STZ}	=	length of the stress transfer zone;
L	=	length of the fully debonded zone;
L_i	=	length of the initial unbonded FRP composite sheet;
P_{crit}	=	mean value of the load in the direct shear test response when the stress transfer zone is fully established.
τ	=	interfacial shear stress;
τ_{max}	=	maximum interfacial shear stress;
ε	=	axial strain in the direction of the load;
σ	=	axial stress in the FRP;
ε_{yy}^{max}	=	axial strain in the fully debonded FRP.

APPENDIX II

MATLAB Code for Arc Length Method

```
% Determination of P-Delta curve
% Interface is modeled using nonlinear springs that exhibit softening behavior
E=230*10^3; %FRP composite elastic modulus in MPa
b=46; %FRP width in mm
L=150; %Bonded length
t=0.16764; %FRP composite thickness in mm
A=b*t; %FRP cross sectional area mm^2
n=L+1; %Number of D.O.F
l=L/(n-1); %Length of FRP element in mm
e=E*A/l; %Axial stiffness of FRP element
s0=0.038; %the relative slip corresponding to the maximum shear stress in mm
tau0=5.97; %the maximum shear stress
k=tau0/s0;
K=zeros(n,n);
K(1,1)=k/2+e;
K(n,n)=K(1,1);
for i=2:n-1
   K(i,i)=k+2*e;
end
j=2;
for i=1:n-1
   K(i,j)=-e;
   K(j,i)=-e;
   j=j+1;
end
fexter=zeros(n,1);
fjr=zeros(n,1);
finter=zeros(n,1);
u=zeros(n,1);
norm=10000;
ij=1;
sf=0.18; % Horizontal intercept
incf=3; %Load incremental endpoint =8KN
incstep=1;
inc=incstep;
d=0;
F(1)=0;
delta(1)=0;
ij=2;
while inc<=incf
   fexter(n)=inc;
   udof=inv(K)*fexter;
   u=u+udof;
   finter=(fint(u,b,l,n,e))'/1000;
   fjr=fexter-finter;
   norm=0;
   for i=1:n
      norm=norm+(fjr(i))^2;
   end
   norm=sqrt(norm)
```

```
    while norm>(0.1*incstep)
        ur=inv(K)*fjr;
        u=u+ur;
        finter=(fint(u,b,l,n,e))'/1000;
        fjr=fexter-finter;
        norm=0;
        for i=1:n
            norm=norm+(fjr(i))^2;
        end
        norm=sqrt(norm)
    end
    F(ij)=inc;
    delta(ij)=u(n);
    ij=ij+1;
    norm=10000;
    inc=inc+incstep;
end
%%%%% Arc Length Method%%%%%%%
ds=0.005; %Arc length
fo=zeros(n,1);
fo(n)=1;
test=0;
test1=0;
j=1;
while (u(n)<3 & test<=1)
    gamaN=fexter(n);
    K=stiff(u,n,e,b,l);
    alfa=trace(K);
    alfa=1000*n/alfa;
    DdI=inv(K)*fo;
    if det(K)>0
        p=+1;
    else
        p=-1;
    end
    Dgama=p*sqrt(ds*ds/(alfa^2+abs(DdI'*DdI)));
    Dd=Dgama*DdI;
    u=u+Dd;
    fexter(n)=gamaN+Dgama;
    finter=(fint(u,b,l,n,e))'/1000;
    ri=fexter-finter;
    norm=0;
    for i=1:n
        norm=norm+(ri(i))^2;
    end
    norm=sqrt(norm)
    while norm>0.001*incstep
        K=stiff(u,n,e,b,l);
        alfa=trace(K);
        alfa=1000*n/alfa;
        pi=(alfa^2)*(Dgama^2)+Dd'*Dd-ds^2;
        Rd=[ri;-pi];
        KK=[K -fo;
            2*Dd' 2*alfa*alfa*Dgama];
        ddg=inv(KK)*Rd;
        for i=1:n
```

```
            dd(i)=ddg(i);
        end
        dgama=ddg(n+1);
        u=u+dd';
        Dd=Dd+dd';
        Dgama=Dgama+dgama;
        finter=(fint(u,b,l,n,e))'/1000;
        fexter(n)=fexter(n)+dgama;
        ri=fexter-finter;
        norm=0;
        for i=1:n
            norm=norm+(ri(i))^2;
        end
        norm=sqrt(norm);
    end
    F(ij)=fexter(n);
    delta(ij)=u(n);
    if (u(n)>0.08 & test1<1)
        for i=1:length(u)
            ustorage(i,j)=u(i);
        end
        j=j+1;
        test1=4;
    end
    test1=0;
    ij=ij+1
    u(n)
    F(ij-1)
    if (F(ij-1)<0.5 & u(n)>0.1)
      test=4;
   end
end
fid=fopen('C:\ustorage.txt', 'w');
for i=1:length(ustorage(:,1))
    for j=1:length(ustorage(1,:))
        fprintf(fid,'%f',ustorage(i,j));
        fprintf(fid,'         ');
    end
    fprintf(fid,'\n');
end
fclose(fid);
plot(delta,F), title('Load versus global slip response')
xlabel('Global slip in mm')
ylabel('Applied load in KN')
for i=1:length(F)
    force(i,1)=delta(i);
    force(i,2)=F(i);
end
fid=fopen('C:\ force.txt', 'w');
for i=1:length(force(:,1))
    for j=1:length(force(1,:))
        fprintf(fid,'%f',force(i,j));
        fprintf(fid,'         ');
    end
    fprintf(fid,'\n');
end
```

```
fclose(fid);
function [stiff]=stiff(disp,ndof,efrp,w,leng)
s0=0.038;
tau0=5.97
sf=0.18
for i=2:ndof-1
   slip=disp(i);
   if slip<s0
      multiplier=+(tau0/s0)*w*leng;
   elseif (slip<=sf & slip>s0)
      multiplier=-(tau0/(sf-s0))*w*leng;
   else
      multiplier=0;
   end
   stiff(i,i)=multiplier+2*efrp;
end
slip=disp(1);
if slip<s0
   multiplier=+(tau0/s0)*w*leng;
elseif (slip<=sf & slip>s0)
   multiplier=-(tau0/(sf-s0))*w*leng;
else
   multiplier=0;
end
stiff(1,1)=multiplier/2+efrp;
slip=disp(ndof);
if slip<s0
   multiplier=+(tau0/s0)*w*leng;
elseif (slip<=sf & slip>s0)
   multiplier=-(tau0/(sf-s0))*w*leng;
else
   multiplier=0;
end
stiff(ndof,ndof)=multiplier/2+efrp;
j=2;
for i=1:ndof-1
   stiff(i,j)=-efrp;
   stiff(j,i)=-efrp;
   j=j+1;
end
```

```
function [fint]=fint(disp,w,leng,ndof,efrp)
%m=2*ndof;
s0=0.038;
tau0=5.97;
sf=0.18;
for i=2:ndof-1
   s=disp(i);
   if s<=s0
      fint(i)=(tau0/s0)*s*w*leng+2*efrp*disp(i)-efrp*(disp(i-1)+disp(i+1));
   elseif (s<=sf & s>s0)
      fint(i)=(tau0+(tau0/(s0-sf))*(s-s0))*w*leng+2*efrp*disp(i)-efrp*(disp(i-1)+disp(i+1));
   else
      fint(i)=0+2*efrp*disp(i)-efrp*(disp(i-1)+disp(i+1));
   end
end
s=disp(1);
if s<=s0
   fint(1)=(tau0/s0)*s*w*leng/2+efrp*(disp(1)-disp(2));
elseif (s<=sf & s>s0)
   fint(1)=(tau0+(tau0/(s0-sf))*(s-s0))*w*leng/2+efrp*(disp(1)-disp(2));
else
   fint(1)=0+efrp*(disp(1)-disp(2));
end
s=disp(ndof);
if s<=s0
   fint(ndof)=(tau0/s0)*s*w*leng/2+efrp*(disp(ndof)-disp(ndof-1));
elseif (s<=sf & s>s0)
   fint(ndof)=(tau0+(tau0/(s0-sf))*(s-s0))*w*leng/2+efrp*(disp(ndof)-disp(ndof-1));
else
   fint(ndof)=0+efrp*(disp(ndof)-disp(ndof-1));
end
```

REFERENCES

Ali-Ahmad, M., Subramaniam, K., and Ghosn, M. (2005). "Experimental Investigation and Fracture Analysis of Debonding between Concrete and FRP." *ASCE, Journal of Engineering Mechanics*, accepted for publication.

Ali-Ahmad, M., Subramaniam, K., Ghosn, M. (2005). "Freeze-Thaw Degradation of FRP-Concrete Interface: Impact on Fracture Parameters", *ASCE, Journal of Materials in Civil Engineering*, submitted for review.

Ali-Ahmad, M., Subramaniam, K., Ghosn, M. (2005). "Analysis of Instability in FRP-Concrete Shear Debonding for Beam Strengthening Applications", *ASCE, Journal of Engineering Mechanics*, submitted for review.

Ali-Ahmad, M., Subramaniam, K., and Ghosn, M. (2004). "Fracture Analysis of the Debonding between FRP and Concrete using Digital Image Correlation." *Proceedings of FRAMCOS-5 International Conference on Fracture of Concrete and Concrete Structures/Vail*, Colorado, USA, 787-793.

Ghosn, M., Subramaniam, K., Wang, J., Ali-Ahmad, M. (2003). "Lifetime Reliability of FRP Reinforced Concrete Bridge Beams", *RILEM, Paris*, May 5-6th.

Ali-Ahmad, M., Subramaniam, K., Ghosn, M. (2004). "Experimental Investigation of Progressive Debonding of FRP Sheets from Concrete Using Digital Image Correlation", *Proceedings of ICFRC International Conference on Fibre Composites, High Performance Concretes and Smart Materials*, Chennai, India, 8-10 January, pp 397-407.

Ali-Ahmad, M., Subramaniam, K., Ghosn, M. (2004). "Application of FRP Technology for Repair of Transportation Infrastructure", *Proceedings of XIII Pan-American Conference of Transportation (PANAM).* September 26-29, Albany, NY

Ali-Ahmad, M., Subramaniam, K., Ghosn, M. (2005). "Fracture Analysis of the Debonding Failure in FRP Strengthened Concrete Beams", *ICACS International Conference on Advances in Concrete Composites and Structures Fibre Composites*, Chennai, India, 6-8 January.

Ali-Ahmad, M., Subramaniam, K., Ghosn, M. (2005). "Environmental Degradation of Bond between FRP and Concrete: Implication on the Fracture Process and Parameters", *ConMat'05 Third International Conference on Construction Materials*, Vancouver, Canada, August 22-24.

ASTM C 39 (2000). "Standard Test Method for Compressive Strength of Cylindrical Concrete Specimens." *Annual Book of ASTM Standards, Concrete and Aggregates*, ASTM, 18-22.

ASTM C 666 (2000). "Standard Test Method for Resistance of Concrete to Rapid Freezing and Thawing." *Annual Book of ASTM Standards, Concrete and Aggregates,* ASTM, 324-329.

Argyris, J. H. (1965). "Continua and Discontinua," *First Conference on Matrix Methods in Structural Mechanics*, *Wrigth-Oatterson Air Force Base*, OH, October, pp. 11-189

Arduini, M., Di Tommaso, A., Nanni, A. (1997). "Brittle Failure in FRP Plate and Sheet-Bonded Beams," *ACI Structural Journal*, 94(4), pp. 363-370.

Arduini, M., Nanni, A. (1997). "Parametric Study of Beams with Externally Bonded FRP Reinforcement, *ACI Structural Journal*, 94(5), pp. 493-501.

Bazant, Z.P., and Planas, J. (1998). "Fracture and Size Effect in Concrete and Other Quasi-brittle Materials." *Publisher: CRC Press*, New York.

Bizindavyi, L., and Neale, K.W. (1999). "Transfer Lengths and Bond Strengths for Composites Bonded to Concrete." *Journal of Composites for Construction*, 3(4), 153-160.

Bisby, L.A, and Green, M. (2002). "Resistance to Freezing and Thawing of Fiber-Reinforced Polymer-Concrete Bond." *ACI Structural Journal*, 99(2), 215-223.

Bruck, H.A., McNeill, S.R., Sutton, M.A, and Peters, W.H. (1989). "Digital Image Correlation Using the Newton-Raphson Method of Partial Differential Correction." *Experimental Mechanics*, 29(3), 261-267.

Buyukozturk, O., and Hearing, B. (1998). "Failure Behavior of Precracked Concrete Beams Retrofitted with FRP," *Journal of Composites for Construction*, 2(3), pp. 138-144.

Bazant, Z.P., and Cedolin, L. (1991). "Stability of Structures," *Publisher*: *Oxford University Press, Inc.*, New York.

Crisfield, M.A. (1983). "An arc-length method including line searches and accelerations," *International Journal for numerical Methods in Engineering*, 19, pp.1269-1289

Choi, S., and Shah, S. (1997). "Measurement of deformations of concrete subjected to compression using image correlation." *Experimental Mechanics*. 37(3), 307-313.

De Lorenzis, L., Miller, B., and Nanni, A. (2001). "Bond of Fiber-Reinforced Polymer Laminates to Concrete." *ACI Materials Journal*, 98(3), 256-264.

Daniel, I. M., and Ishai, O. (1994) "Engineering Mechanics of Composite Materials." *Oxford University Press*, New York.

El-Mihilmy, M.T. and Tedesco, J.W. (2000). "Analysis of Reinforced Concrete Beams Strengthened with FRP Laminates." *Journal of Structural Engineering*, 126(6), 684-691.

Forde, B.W.R. and Steiemer, S.F. (1987). "Improved arc length orthogonality methods for nonlinear methods for nonlinear finite element analysis," *Computers and Structures*, 27(5), pp. 625-630.

Jansen, D. C. and Shah, S. P. (1997). "Effect of Length on Compressive Strain Softening of Concrete." *Journal of Engineering Mechanics, ASCE,* 123(1), 25-35.

Khalifa, A., Gold, W.J., Nanni, A., and Abdel Aziz, M.I. (1998). "Contribution of Externally Bonded FRP to Shear Capacity of Flexural Members," *ASCE-Journal of Composites for Construction*, 2(4), pp. 195-203.

Grace, N.F., Singh, S.B. (2005). "Durability Evaluation of Carbon Fiber-Reinforced Polymer Strengthened Concrete Beams: Experimental Study and Design." *ACI Structural Journal*, 102(1), 40-53.

Hag-Elsafi, O., Kunin, J., Alampalli, S., and Conway, T. (2001). "Strengthening of Route 378 Bridge Over Wynantskill Creek in New York Using FRP Laminates." *Special Report, Transportation Research and Development Bureau*, NYSDOT, 1-33.

Ingraffea, A. and Wawrzynek, P. (1994). "FRANC2D: A Case Study in Transfer of Software Technology." *Research Transformed into Practice: Implementations of NSF Research, J. Colville, A. Made, Editors, ASCE Press, New York*, 233-344.

Karbhari, V.M., Saible, F., and Hegemier, G.A. (1996). "On use of Fiber Reinforced Composites for Infrastructure Renewal- A systems Approach." *Proceedings of the Fourth Materials Engineering Conference: Materials for the New Millennium*, 1091-1100.

Leung, C.K.Y. and Tung, W.K. (2001). "A Three-Parameter Model For Debonding of FRP From Concrete Substrate." *FRP composites in Civil Engineering*, 1, 373-379.

Leung, C.K.Y. (2001). "Delamination Failure in Concrete Beams Retrofitted with a Bonded Plate," *ASCE-Journal of Materials in Civil Engineering*, 13(2), pp. 106-113.

Leung, C.K.Y., Klenke, M., Tung, W.K., and Luk, H.C.Y. (2000). "Investigation of Nonlinear Interfacial Behavior for Concrete Beams Retrofitted with Composite Plate," *Proceedings of International Symposium of Brittle Matrix composite 6, Warsaw*, pp. 286-295.

Leung, C.K.Y. (2004). "Fracture Mechanics of Debonding Failure in FRP-Strengthened Concrete Beams," *FraMCoS-5 conference*, pp. 12-16.

Lopez Acevedo, M. D. M. (2000). "Study of the Flexural behavior of Reinforced Concrete Beams strengthened by externally bonded Fiber Reinforced Polymeric (FRP) Laminates." *Doctoral dissertation*. The University of Michigan. 2000.

Lawler, J., Keane, D., and Shah, S. (1999). "Measuring Three-dimensional Damage of Mortar in Compression with X-rays Microtomography and Digital Image Correlation." *ACI Spring Convention*.

Meier, U. and Kaiser, H. P. (1991). "Strengthening of Structures with CFRP Laminates." *Proceeding of the Conference on Advanced Composites Materials in Civil Engineering*, ASCE, 224-232.

Mukhopadhyaya, P., Swamy, R.N., and Lynsdale, C. J. (1998). "Influence of Aggressive Exposure on the Behavior of Adhesive Bonded Concrete-GFRP Joints." *Construction and Building Materials*, 12, 427-446.

Meier, U., Deuring, M., Meier, H., and Schwegler, G. (1992). "Strengthening of Structures with CFRP Laminates: Research and Applications in Switzerland," *Advanced Composite Materials in Bridge and Structures*, *Canadian Society for Civil Engineering*.

Malek, A., Saadatmanesh, H., and Ehsani, M. (1998). "Prediction of Failure Load of R/C Beams Strengthened with FRP Plate Due to Stress Concentration at the Plate End," *ACI Structural Journal*, 95(1), pp.142-152.

Norris, T., Saadatmanesh, H., and Ehsani, M. (1997). "Shear and Flexural Strengthening of R/C Beams with Carbon Fiber Sheets," *ASCE Journal of Structural Engineering*, 123(7), pp. 903-911.

Pian, T.H.H., and Tong, P. (1970). "Variational Formulation of Finite Displacement Analysis," *IUTAM Symposium on High speed Computing of Elastic Structures*, Liege, Belgium, pp. 43-63

Quantrill, R.J., Holloway, L.C., and Thorne, A.M. (1996). "Experimental and analytical investigation of FRP strengthened beam response." Part I, II. *Magazine of Concrete Research*, 48(177), 331-351.

REPLARK SYSTEM (2000). Technical Manual. Manufactured by Mitsubishi Chemical Corporation, Japan.

Ritchie, P.A., Thomas, D.A., Lu, L.W. and Connely, G.M (1991), "External Reinforcement of Concrete Beams Using Fiberglass Reinforced Plastics", *ACI Structural Journal*, 88(4), pp. 490-500.

Riks, E. (1979). "An incremental approach to the solution of snapping and buckling problems," *International Journal of Solids and Structures*, 15, pp. 529-551

Riks, E. (1972). "The application of Newtown's method to the problem of elastic stability," *Journal of Applied Mechanics*, pp. 1060-1065

Subramaniam, K.V., Popovics, J.S, and Shah, S.P. (1998). "Testing concrete in torsion: Instability Analysis and Experiments." *Journal of Engineering Mechanics*, ASCE, 124(11), 1258-1268.

Saadatmanesh, H. and Malek, A.M. (1998). "Design Guidelines for Flexural Strengthening of RC Beams and FRP Plates." *Journal of composite for construction*, ASCE, 2(4), 158-164.

Sutton, M.A., Wolters, W.J., Peters, W.H., and Ranson, W.F. (1983). "Determination of Displacements Using an Improved Digital Correlation Method." *Computer Vision*, 133-139.

Sutton, M.A., Babai, M., and Jang, J. (1988). "Effects of Subpixel Image Restoration on Digital Correlation Error Estimates." *Optical Engineering*, 27(10), 870-877.

Sutton, M.A, Bruck, H.A. (1989). "Digital Image Correlation Using the Newton-Raphson Method of Partial Differential Correction." *Experimental Mechanics*, 29(3), 261-267.

Sutton, M.A., Chao, Y.J., and Lyons, J.S. (1993). "ComputerVision Methods for Surface Deformation Measurements in Fracture Mechanics, Novel Experimental Techniques in Fracture Mechanics." *ASME-AMD* Vol. 176, 203–217.

Savoia, M., Ferracuti, B. and Mazzotti, C. (2003). "Non-linear bond-slip law for FRP-concrete interface." *FRPRCS-6 Conference Proceedings*, Singapore, 1-10.

Saadatmanesh, H., and Ehsani, M.R. (1991). "RC Beams Strengthened with GFRP Plates. I: Experimental Study," *Journal of Structural Engineering*, 117(11), pp.3417-3433.

Spadea, G., Bencardino, F., and Swamy, R.N. (1998). "Structural Behavior of Composite RC Beams with Externally Bonded CFRP," *ASCE Journal of Composites for Construction*, 2(3), pp. 132-137.

Taljsten, B. (1996). "Strengthening of Concrete Prisms using the Plate-Bonding Technique." *International Journal of Fracture*, Vol. 82, 253-266.

Taljsten, B. (1997a). "Strengthening of Beams By Plate Bonding," *ASCE-Journal of Materials in Civil Engineering*, 9(4), pp. 206-212.

Taljsten, B. (1997b). "Defining Anchor Lengths of Steel and CFRP Plates Bonded to Concrete," *International Journal of Adhesion and Adhesives*, 17(4), pp. 319-327.

Triantafillou, T.C, and Pelvris, N. (1992). "Strengthening of RC Beams with Epoxy-Bonded Fiber-Composite Materials," *Material and Structures*, Paris, 25(149), 201-211.

Triantafillou, T.C. (1998). "Shear Strengthening of Reinforced Concrete Beams using Epoxy-bonded FRP Composites," *ACI Structural Journal*, 95(2), pp. 107-115.

Teng, J.G., Lu, X.Z., Ye, L.P. and Jiang, J.J (2004). " Recent Research On Intermediate Crack Debonding In FRP-Strengthened RC Beams." *Proceedings of 4th International Conference on Advanced Composite Materials in Bridges and Structures*, (ACMBS IV), Calgary, Alberta , Canada July 2004, 1-13.

Ueda, T., Sato, Y., and Asano, Y. (1999). "Experimental Study on Bond Strength of Continuous Carbon Fiber Sheets," *Proceedings of the FRPRCS-4*, pp. 407-416.

Wu, Z. and Niu, H. (2000). "Shear transfer Along FRP-Concrete Interface in Flexural Members." *J. Materials, Conc. Struct., Pavements*, JSCE, 49(662), 231-245.

Wu, Z. and Niu, H. (2000). "Shear transfer Along FRP-Concrete Interface in Flexural Members," *J. Materials, Conc. Struct., Pavements, JSCE*, 49(662), pp. 231-245.

Wu, Z., Matsuzaki, T., and Tanabe, K. (1997). "Interface Crack Propagation in FRP-Strengthened Concrete Structures." *Non-Metallic (FRP) Reinforcement for Concrete Structures*, *Japan Concrete Institute*, 1, 319-326.

Wu, Z. and Yin, J. (2003). " Fracturing Behaviors of FRP-Strengthened Concrete Structures." *Engineering Fracture Mechanics*, 70, 1339-1355.

Wempner, G.A. (1971). "Discrete Approximations Related to Nonlinear Theories of Solids," *International Journal of Solids and Structures*, 7, pp. 1581-1599

William K.J., Warnke, E.P. (1974). "Constitutive Model for the Triaxial Behavior of Concrete." *Proceedings of Int. Assoc. for Bridge and Structural Engineering*, 19, pp. 1-30.

Yuan, H., Wu, Z., and Yoshizawa, H. (2001). "Theoretical Solutions on Interfacial Stress of Externally Bonded Steel/Composite Laminates." *Structural Eng./Earthquake Eng*., JSCE, 18(1), 27-39.

Yin J. and Wu Z.S. (2003). " Structural Performances of Short Steel-Fiber Reinforced Concrete Beams with Externally Bonded FRP Sheets." *Construction and Building Materials*, Vol. (17), pp. 463-470.

Zienkiewicz, O.C, (1971). "Incremental Displacement in Non-linear Analysis," *International Journal for Numerical Methods in Engineering*, 3, pp. 587-588